Advanced materials on the basis of nanostructured catalysed magnesium hydride for hydrogen storage

By

Jonathan Teik Ean, GOH

A thesis submitted in fulfilment of the requirements for the degree of

Doctor Philosophiae **(PhD)**

Department of Chemistry

University of the Western Cape

Supervisor: Dr Lototskyy M. V.

Co-supervisors: Prof. Yartys V. A., Dr Khotseng L.

November 2018

Student number 3280368

Keywords

Hydrogen storage

Magnesium hydride

Nanocomposites

High-Energy Reactive Ball Milling

Catalysis

Carbon additive

Hydrogen storage capacity

Absorption/desorption kinetics

Cyclic stability

Morphological changes

Abstract

Magnesium hydride has long been regarded as a promising candidate for lightweight hydrogen storage applications, owing to reasonably high theoretical capacity (7.6 wt. %). It is burdened by slow absorption/desorption kinetics which has been the target for improvement of many research groups over the years. Nanostructured MgH_2 prepared by high energy reactive ball milling (HRBM) of Mg under hydrogen atmosphere with the addition of V or Ti results in modified MgH_2 that demonstrates superior hydrogenation/dehydrogenation kinetics without a crippling compromise in storage capacity. Mg – FeV nanocomposites prepared via ball milling of Mg and FeV raw materials demonstrated up to 96.4% of the theoretical storage capacity and comparable kinetics to Mg - V prepared via the same method using pure refined V (which is far costlier than FeV). In both cases, the hydrogenation/dehydrogenation kinetics was much improved than pure Mg alone, as evidenced by faster hydrogenation times. In terms of cyclic stability, Mg – 10FeV demonstrated improvement over pure Mg with final absorption and desorption capacities of 4.93 ± 0.02 wt. % and 4.82 ± 0.02 wt. % respectively over 30 cycles. When compared against Mg – V, Mg – FeV showed slightly inferior improvements, attributed to incomplete hydrogenation of V in the presence of Fe. However, they share similar crystalline BCC, BCT – V_2H and FCC - VH phases with the size of less than 10 nm and demonstrated the same behaviour at high temperatures; at temperatures approaching 400 °C, particle sintering became an issue for both nanocomposites resulting in a drop in absorption capacity even in the first cycle. The further inclusion of carbonaceous species showed several effects, one of which was an improvement in hydrogen uptake speed as well as kinetics for the addition of 5 wt. % activated carbon. For the sample with 5 wt. % graphite, the appearance of an initial incubation period of up to 60 minutes was noted, presumably corresponding to the duration of time when the carbon was sheared and crushed before hydrogenation commences.

For the (continuation) study of Mg - $FeTiO_3$ composites, SEM analysis performed on samples showed vastly different morphologies between samples with and without carbon (particularly graphite)

content. It is suggested that the scattered graphite across the Mg/MgH_2 matrix provides some protection against MgO encapsulation that then leads to loss in reversible hydrogen storage capacity, as suggested in the preceding study. The graphite protection may also slow down the process of Mg sintering during high temperature cycling of absorption/desorption.

In the case of Mg – Ti binary alloys prepared using HRBM, high storage capacities and hydrogenation/dehydrogenation kinetics were observed; hydrogen storage capacity decreased when cycling at high temperatures (starting at T = 350 °C) which hampered its functionality and heat source/sink attributes, although the kinetics of hydrogen sorption were not significantly affected. This deterioration was associated with morphological changes occurring to the material nanostructure during cycling under high temperatures, resulting in Mg particle sintering as well as aggregation of TiH_2 particles. Consequently, the porosity and available surface areas of the nanocomposite was drastically reduced while the catalytic effect of Ti to the system greatly neutralised. The incorporation of 5 wt. % graphite to the MgH_2 - TiH_2 nanocomposite during HRBM effectively counteracts these phenomena, leading to good hydrogen sorption performance past 100 cycles of hydrogen absorption/desorption. The role of graphite in this system appears to be in terms of preserving the Mg fine structure after HRBM to prevent excessive grain growth maintaining segregation of TiH_2 particles in the cycled material. As such, the unchanged structure largely corresponds to unchanged reversible storage capacities and absorption/desorption kinetics.

Declaration

I declare that Advanced materials on the basis of nanostructured catalysed magnesium hydride for hydrogen storage is my own work, that it has not been submitted for any degree or examination in any other university, and that all the sources I have used or quoted have been indicated and acknowledged by complete references.

Full name: Jonathan Teik Ean GOH

Date: 5 November 2018

Signed: 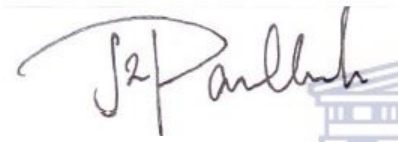

Acknowledgements

GOD. For without the constant presence and steady guidance from above, nothing that preceded this work or anything that follows, would be possible.

My parents and brother: For you love and encouragement from near and far. I know that I can count on your support in every way.

My family: You never stopped believing in me. Thank you.

To Michael, you are the one that made this work and thesis possible. Thank you for not giving up on me throughout all our challenges and obstacles. I am deeply grateful for your guidance and mentorship.

Professor Yartys and Roman (IFE): Along with Michael I consider you to be the foremost experts in the field of metal hydride hydrogen storage. It was an honour to have met and collaborated with you. Your expanse of knowledge humbles me and your commitment to your work drives me further.

To Lindiwe, thank you for being a reassuring presence to me at UWC. People came and went but you were always around.

Yevgeny, Wafeeq, Lydia, Piotr, Olivia, Serge: Your guidance, help and friendship have been invaluable to me in my time at HySA and beyond. Thank you!

Franscious (UWC EMU Unit), thank you for training me and explaining the concepts of microscopy so patiently. Your collaboration has formed an integral part of this work.

Professor Bruno Pollet: If it were not for you I wouldn't have even started this PhD journey. Thank you for seeing the potential in me and for opening this pathway to me.

To Lucy, thank you for staying by me through all of this. I look forward to whatever comes next knowing you are with me.

This work was supported by ERAfrica FP7 International Collaboration Program, project RE-037 "HENERGY". I also acknowledge the Department of Science and Technology (DST), Republic of South Africa, to be co-investor of the above-mentioned project, as well as the funder of the HySA Program (project KP3-S02)

Contents

List of Tables & Figures

1.0 Introduction

Energy is a vital prerequisite for life. It allows our bodies to perform our basic internal and external functions. Every form of life has a method of extracting, storing and utilising energy most effectively depending on their environment and purpose.

Energy is also a vital prerequisite for modern living. The industrial revolution of the 18th and 19th century is noted for being a period of transition from manual mechanical power to machine power. This resulted in an exponential increase in production capabilities and an improvement in the general standard of living.

Energy propels civilisation and technological advancement. The way in which we harvest, store and use our energy resources makes all the difference in terms of our wellbeing, growth and development as a species. As such, energy is an inseparable concept from mankind, and our relationship with energy is critical.

1.1 Background: The Global Energy Landscape

The history of mankind on Earth can be viewed retrospectively as several sequential and concurrent phases of energy resource development. From the time of nomads to settlers, from the Stone Age to the Bronze Age, from hunter-gatherers to cultivators of the land, from simple handheld tools to complex machines, from small scale production to mass production in the industrial revolution; each era brought with it distinct changes in the way we used energy to improve society.

The industrial revolution in particular was primarily accelerated by the commercialisation of oil and the invention of the steam engine powered by coal as a replacement for water power [1]. When first introduced, fossil fuels possessed an energy density the likes of which had never been seen before and mankind unleashed its potential to drive progress. The replacement of water wheels with coal-fired steam engines also allowed for factories to be situated away from rivers and flowing water

resources, allowing for greater expansion and reach. This revolutionised every aspect of human life, from production lines to transportation to agriculture and brought us to where we are today.

1.2 Climate change & Alternative Energy

Now, we approach the end of oil as an energy resource. However, even as the debate persists about whether peak oil production has passed, two facts emerge indisputable. Firstly, fossil fuel resources are finite and second: unrestrained burning of fossil fuels is deteriorating the condition of our planet. As early as 1896, Swedish scientist Svante Arrhenius had already established a link between elevated levels of carbon dioxide in the atmosphere and increased global temperatures [2]. However, he predicted a longer timescale for warming and even suggested that warming was necessary to maintain a habitable temperature on the planet. This sentiment was the subject of much discussion, investigation and disagreement.

Today, anthropomorphic climate change is no longer a subject of debate as scientists have shown conclusively (Figure 1.1) the relationship between atmospheric carbon dioxide levels and global temperatures [3], [4] not to mention the negative downstream cascade effects [5]. Phenomena such as increasingly devastating storms, hurricanes, typhoons, floods, heatwaves and even blizzards have been attributed to the rising temperature of the planet. Furthermore, melting polar ice caps and ice shelves breaking off from the poles threaten to elevate sea levels drastically within the next few years; cities such as New York and Shanghai, and even countries such as Japan, Bangladesh and the Netherlands are under threat of being submerged should the situation persist with the current trajectory.

The impact of climate change is exacerbated by our rapidly expanding population and urbanisation world-wide. With the energy sector being one of the largest contributors of carbon emissions we face the challenge of energy demand in an exponential incline at a time when we need to reconsider and even revamp the way we use energy.

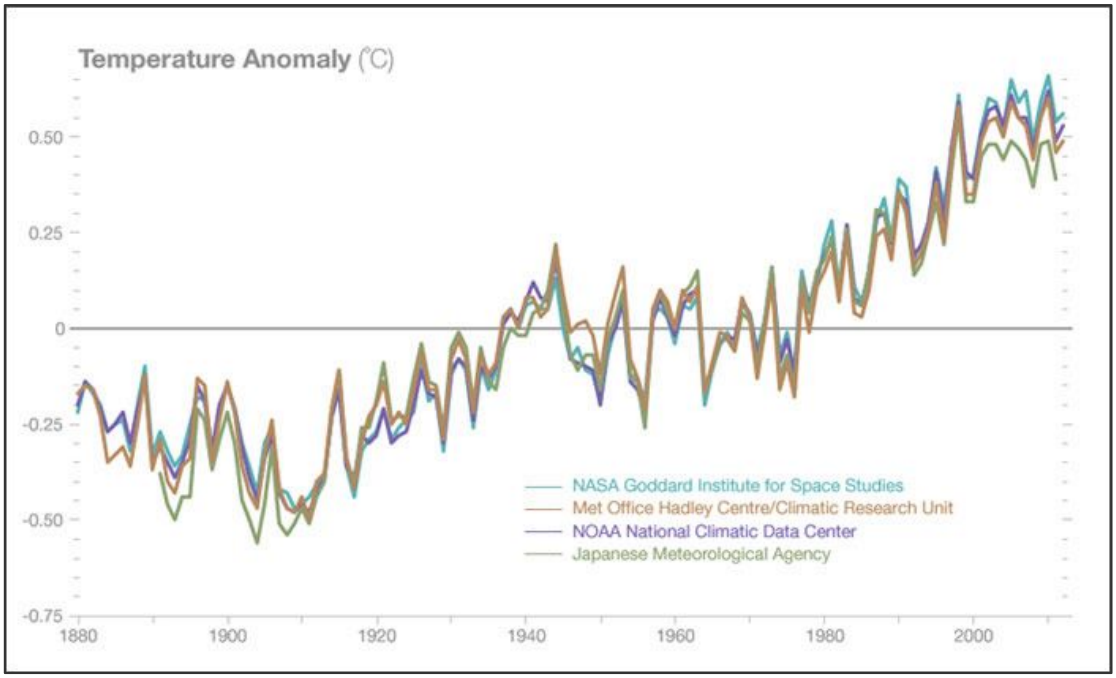

Figure 1.1: Temperature data consensus (Source: NASA)

Nuclear energy was previously considered by many to be the key for replacing coal and gas-fired plants in providing base load power. France for example, has long established nuclear energy as its solution for energy stability and security. As such, it has 58 nuclear power plants that contribute 75% of its electricity; the low cost of electricity generation from nuclear power also makes France the world's largest net exporter of electricity with profits over 3 billion euros per year [6]. However, nuclear energy has always had a less sterling aspect to it and this is concerned primarily with the highly radioactive fuel and waste that it consumes and generates. Whether it is nuclear fuel or nuclear waste, there have been countless debates regarding the actual environmental impact of nuclear energy because of the corresponding radioactive material. The half-life of nuclear waste (which is a numerical figure that reflects the duration required for material to completely lose its radioactivity) is typically in the order of hundreds, if not thousands of years. This presents huge infrastructural and logistical challenges as radioactivity at certain levels is lethal to all forms of life. More recently, the Fukushima Daiichi nuclear disaster in 2011 occurred when a tsunami caused severe damage that resulted in a chain reaction of events and explosions. Clean-up and containment

operations are still in process today, and it has been estimated that complete decontamination and clean up may take up to 40 years [7]. This incident had major repercussions and caused huge reactions globally in terms of perception towards nuclear power and was the tipping point for many. Several countries including Germany, Italy and France accelerated their plans to decrease their dependence on nuclear energy; Germany has decided to phase out nuclear energy altogether by 2022 and focus on renewable energy instead [8]. Based on recent reports and milestones achieved in renewable energy, they are very much on course (if not ahead of schedule) to be fully reliant on renewable energy resources.

Renewable energy technologies have been highlighted as the alternative way to fulfil our energy demands albeit in a cleaner and more sustainable manner. Renewable energy includes energy from sources such as solar, wind, tidal, wave, geothermal and biomass energy; all are carbon neutral when it comes to energy production (though not necessarily at implementation) and are potentially inexhaustible. The main issue with renewable energy is intermittency and that current energy storage devices do not operate at efficiencies high enough to justify wide scale implementation; as such electricity produced from renewables during periods of non-peak demand cannot be stored efficiently. Justifiably, renewable energy was often viewed as a supplementary energy source to fulfil peak demand power. However, this obstacle has not hindered the development of renewable energy technologies, indicated by major milestones such as record energy levels produced from wind power [9]. Other examples include excellent developments and projections for solar energy, which is expected to be cheaper than coal within 10 years [10], as shown in Figure 1.2 below. Even previously coal-centric countries such as China have made significant inroads in establishing renewable energy technologies within their provinces and cities [11]. In 2017, China has been reported to be the biggest investor in solar, wind and hydro power on the planet, recently switching on the biggest floating solar farm on the planet (40 MW) [12].

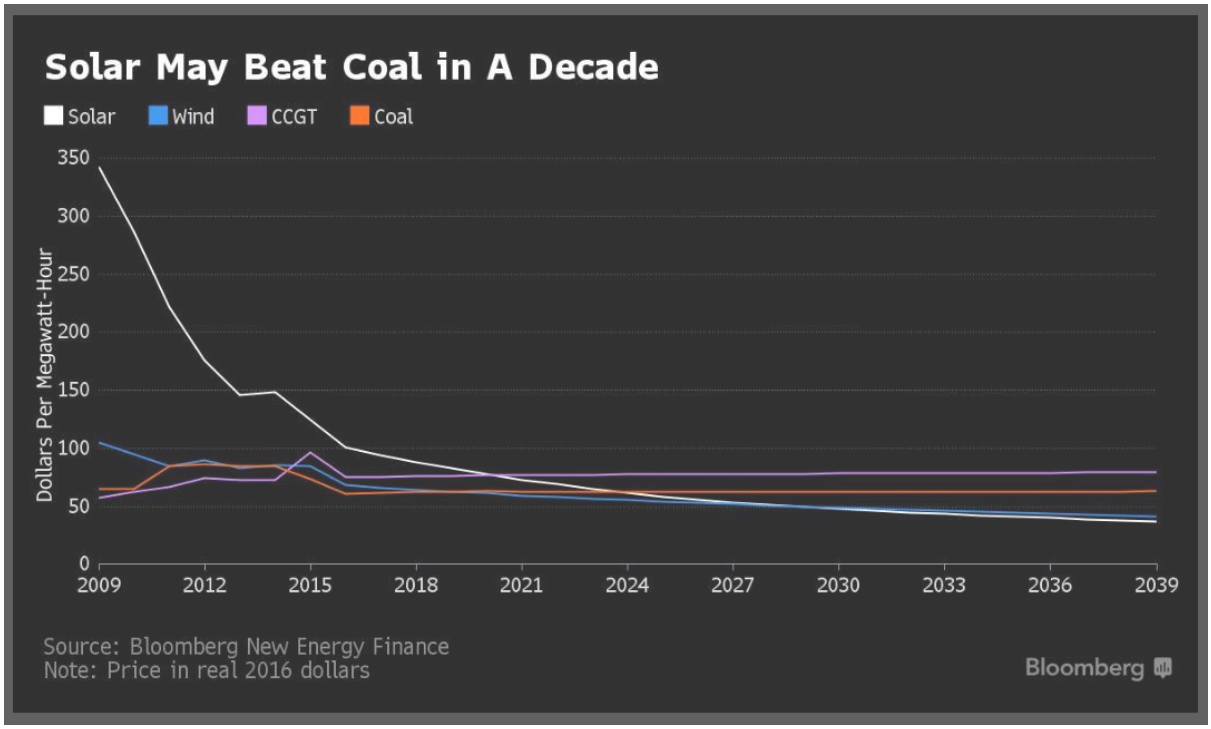

Figure 1.2: Projected costs for selected energy resources (Source: Bloomberg New Energy Finance)

Alongside renewable energy technologies, fuel cell technology is also undergoing rapid development for various applications, the most prominent being vehicular as well as combined heat and power functions. Fuel cells are essentially silent electrochemical devices that convert fuel (typically hydrogen or methanol) into electricity and by-products (water and residual heat) via a combined oxidation-reduction reaction. No carbon dioxide is produced from the reaction, which is an attractive plus point for this technology. Alongside battery electric vehicles (BEV), fuel cell powered vehicles are widely accepted as the two main vehicular power systems of the future. The development of these two fields in recent times has been exciting, to say the least, and promising enough that most major automakers have already committed to phasing out the internal combustion engine in the near future [13]. Fuel cell vehicles would offer several advantages over battery electric vehicles, most notably greater range and faster charging times since fuel cell vehicles can be refuelled relatively quickly with hydrogen as opposed to hours of plugged-in charging [14].

Bearing in mind that the real barrier to renewable energy implementation is energy storage, hydrogen has also emerged as an excellent candidate for energy storage due to its high energy density and abundance. Hydrogen is the most abundant element in the universe and exists in the form of compounds and complexes on Earth. Considering factors such as sustainability, energy security and environmental impact, it is only logical to consider hydrogen as the primary energy vector and storage medium.

1.3 The Argument for Hydrogen

Scientists and governments have long been debating the importance of transitioning to the hydrogen economy. Despite newly identified unconventional fossil fuel reserves most notably shale oil and tar sands, it remains undisputed that the combustion of fossil fuels (regardless of efficiency) produces greenhouse gases (carbon dioxide, methane etc.). Greenhouse gases in turn trap heat within the Earth's atmosphere, culminating in climate change and pollution. Hydrogen is a potential solution to this problem as it has the highest energy density among common fuels [15], but only if produced in a clean and sustainable method. Currently, hydrogen is produced for industrial purposes mainly via methane steam reforming. This is not the ideal method as it is highly energy intensive and by-products include carbon dioxide, although it can be immediately contained on site. A more sustainable method of producing hydrogen is via electrolysis, but this process is still being developed for greater efficiency and reliability at a large scale [16].

1.3.1 The Hydrogen Future

In his review of progress and problems related to hydrogen storage, Zhou noted that the historical evolution of human fuels from coal to petroleum to natural gas followed the trend of increasing hydrogen content and the final step must surely be towards pure hydrogen [17].

Being the most abundant element in the universe, hydrogen presents a more sustainable and 'cleaner' alternative than any other known fuel. Hydrogen on earth, however, exists primarily in the form of compounds. Because of this, there is a significant processing cost associated with obtaining

pure hydrogen and this elevates the cost of hydrogen above that of petrol even though it has three times the lower heating value (120.21 MJ/kg for hydrogen, 43.448 MJ/kg for petrol) [17], [18].

The Hydrogen Economy was proposed in 1970 as a conceptual energy system of the future. It consists of a 4 pronged approach - hydrogen production, storage, transportation and usage - facilitating the use of hydrogen as an energy vector. However, due to the significant physical and chemical differences between hydrogen and fossil fuels, considerable planning, adjustments and even infrastructural rebuilds will be necessary before the Hydrogen Economy may be realised. Needless to say, the pathway towards mainstream and commercialised hydrogen as an energy vector is still significantly distant, although progress has been greatly accelerated recently.

To maintain the scope of this thesis, discussions will now be focused solely towards hydrogen storage.

1.3.2 Hydrogen Storage

Hydrogen Storage has been earmarked as a far superior method of conserving energy than most other storage methods. While batteries eventually lose their charging capacity after numerous charge cycles and require long charging times, hydrogen storage provides a more stable long term means to store energy besides shorter recharge times. Robust hydrogen storage is also a vital precursor to the commercialisation of fuel cell technology because these devices are so heavily reliant on a pure supply of hydrogen.

1.3.2.1 Methods for Hydrogen Storage

There are three current technologies that are commercially available for hydrogen storage: compressed, liquefied and solid-state hydrogen storage. A simple chart showing the types of hydrogen storage methods is given in Figure 1.3. All have their advantages and drawbacks, which will be discussed below. Complications arise with regards to the handling of hydrogen as it possesses a high energetic mass density but an extremely low volumetric density i.e. hydrogen molecules, although small, are difficult to compress due to their small size and high energetic content. This

results in a high energy demand for compressing hydrogen or freezing it to reduce the intermolecular distance for more effective storage.

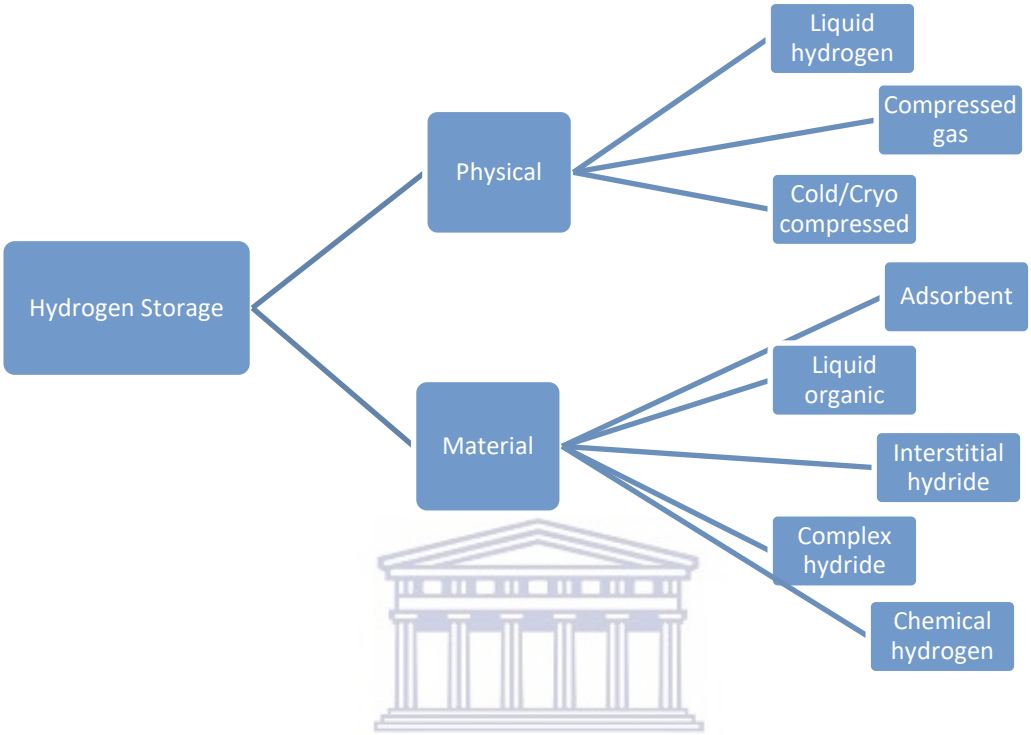

Figure 1.3: Various methods of hydrogen storage (Adapted from [19])

Compressed Hydrogen Storage

As mentioned previously, hydrogen has high energy density in terms of mass but not volume. This results in major energetic requirements when compressing hydrogen, besides safety concerns when dealing with compressed hydrogen. As such, a large proportion of the energy stored is actually offset towards mechanical compression of the gas itself.

Since the first commercial fuel cell vehicle was produced (Honda FCX Clarity), compressed hydrogen tanks has been the default choice method of storage hydrogen on board. These tanks typically contain up to 5 kg of hydrogen (or 70 MPa) and are made possible by the development of new high strength plastic materials to withstand high internal pressures while being robust enough to be

fitted into vehicles. Although the current state of technology allows for ranges in excess of 500 km on a full tank of hydrogen [20], the fact remains that compressing hydrogen to 70 MPa is a highly energy intensive process. Also noteworthy is that 5 kg of hydrogen occupies a significant volume in the vehicle; space that could otherwise be allocated towards cabin or cargo space.

Traditional concerns with regards to compressed hydrogen storage have always revolved around the safety of the pressurised cylinder itself coupled with the combustible nature of hydrogen. These fears have now been addressed and allayed through the development of highly stable and safe carbon fibre tanks and correcting misconceptions about the nature of hydrogen combustion.

Liquefied Hydrogen Storage

Several options are available for liquefied hydrogen storage; however most methods render the system highly sensitive to temperature to maintain hydrogen in liquefied form. Liquefying hydrogen requires a cryogenic facility and this is typically very costly and sensitive in nature. As such, this method is highly energy intensive and is unlikely to justify the incurred cost. Furthermore, this method is not robust and cannot be implemented universally. As such, this can be viewed as a specialised method for very specific applications and conditions i.e. hydrogen storage in isolated cold climate areas.

Solid-State Hydrogen Storage

Solid-state storage in salts (e.g. CaH_2) or metal hydrides (e.g. MgH_2) have been investigated since the early 1900s. In terms of safety, this method stands out from the previous two as hydrogen is absorbed into the lattice structure of the material. As such there is far less sensitivity to pressure and temperatures. However, metal hydride storage is the heaviest of the three methods discussed, therefore requiring more careful planning and consideration before implementation. The weight of metal hydride storage methods is not necessarily a disadvantage as applications such as utility vehicles i.e. forklifts or cranes generally require counter-balance weight. In this respect, the metal hydride hydrogen storage module may fulfil two roles within the vehicle [21].

Metal hydrides have previously exhibited excellent capabilities in terms of hydrogen storage per unit volume. Generally, a fixed volume of metal hydride material can absorb more hydrogen than an empty tank of the same volume. That being said, its use in fuel cell vehicles would also provide a viable alternative to compressed hydrogen storage tanks which tend to require excessively high pressures (>300 bar) for commercial operation.

1.3.2.2 Hydrogen Storage Challenges

The US DOE's Office of Energy Efficiency & Renewable Energy has highlighted several challenges relating to hydrogen storage technologies. While the requirements of transportable hydrogen storage are generally less restrictive than off-board bulk storage, they are still similar and often translatable. For example, off-board bulk storage might not require minimal weight but considerations of volume and 'footprint' limitations are still valid.

Key challenges for on-board hydrogen storage include:

- *Weight and Volume* – current systems are too heavy and voluminous, limiting vehicle range as compared to petrol fuelled vehicles
- *Efficiency* – energy efficiency must be considered when (re)charging and discharging hydrogen from the systems
- *Durability* – materials and components are needed to allow a lifetime of 1500 cycles
- *Refuelling time* – must be made comparable to current petrol refuelling times (i.e. less than 3 minutes)
- *Cost* – high material associated cost make it non-competitive with current fuel tanks; lower cost materials and components are needed as well as low –cost, high-volume manufacturing methods
- *Codes and Standards* – applicable codes have not been established, hindering public acceptance and commercialisation

- *Life-Cycle and Efficiency Analyses* – lack of relevant data with regards to the full life-cycle cost and efficiency for hydrogen storage systems. [22]

Other than the abovementioned challenges identified by the US DOE, a set of incremental targets have also been mapped out for hydrogen storage technologies. They are briefly summarised in Table 1.1.

Storage parameters	Units	2020	Ultimate Target
Volumetric capacity	kWh/L (kg H_2/L system)	1.3 (0.040)	2.3 (0.070)
Gravimetric capacity	kWh/kg (kg H_2/kg system)	1.8 (0.055)	2.5 (0.075)
Cycle life	Cycles	1500	1500
Minimum delivery pressure	Bar	5	3
Maximum delivery pressure	Bar	12	12
Min/max delivery temperature	K	233/358	233/358
Refilling time	Kg/min	1.5	2.0

Table 1.1: Hydrogen storage targets set by the US DOE [23]

1.4 Metal Hydride Hydrogen Storage

The discovery of metal hydrides (MH) as means for 'portable' hydrogen was made in the early 20th century. An early patent filed by Elektrochemische Werke Bitterfeld in 1905 thus claimed that 1 kg of molten calcium absorbed hydrogen so rapidly that it was converted into CaH_2 in only five minutes with an 84 % yield [24].

MH storage can be divided into 3 temperature classes: high, medium and low temperature. Low temperature systems exhibit good reaction kinetics and operate just above room temperature, but has a low storage capacity (1 - 2 wt. %). Most AB_2 and AB_5 materials (A = Zr, Ti; B = Ni, Mn, Cr, V) fall into this category. Medium temperature MH elements include palladium (Pd) and demonstrate intermediate storage capacities and kinetics. High temperature hydrides are those that operate at temperatures above 300 °C. A general overview of the operating temperatures and pressures of

various metal hydrides is shown in Figure 1.4. The area of relevance to this study is the three profiles for Mg based composites between 250 °C and 500 °C. This is the general operating temperature for Mg and hydrogen. Lower operating temperatures would be ideal for smaller applications as well as in a vehicular setting whereas temperatures higher up the scale are best suited for pairing with devices such as solid oxide fuel cells, which typically perform best at temperatures closer to 1000 °C.

Of interest also is that the combination of Mg and other known hydrogen absorbing metals such as V or Ti tends to produce intermediate hydrogen sorption temperatures; this knowledge is transferable and useful to estimate sorption temperatures of different metal combinations. The combination of Mg-Ti is explored in a later chapter of this work, yielding very interesting and promising results.

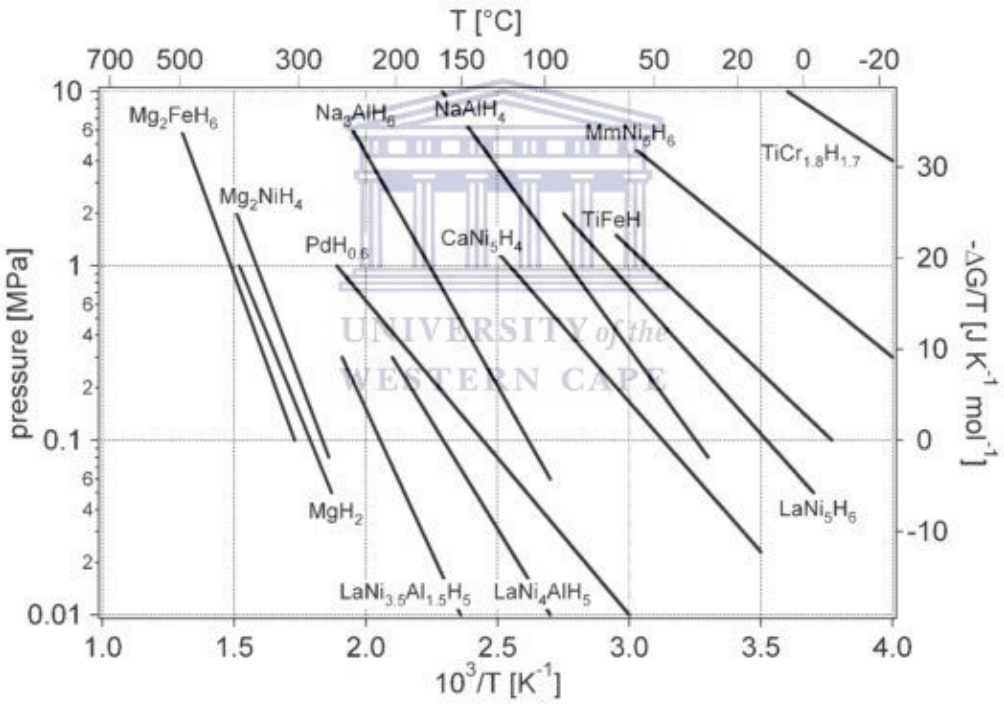

Figure 1.4: Van't Hoff plots of various metal hydrides [25]

MgH_2 has been highlighted as the most promising material for on-board hydrogen storage, owing to its high reversible storage capacity (7.6 wt. %) and low cost. It is burdened by slow kinetics but

although pure Mg only reacts with hydrogen at temperatures ≥300 °C, several methods have been identified in an attempt to improve the thermodynamic and kinetic properties of Mg.

In this work, we attempt to create binary Mg alloys with other metals and compounds using a low energetic method and examine the outcome. The aim is indeed to enhance reaction kinetics, improve cyclic stability as well as thermal stability, without sacrificing too much of the reversible storage capacity.

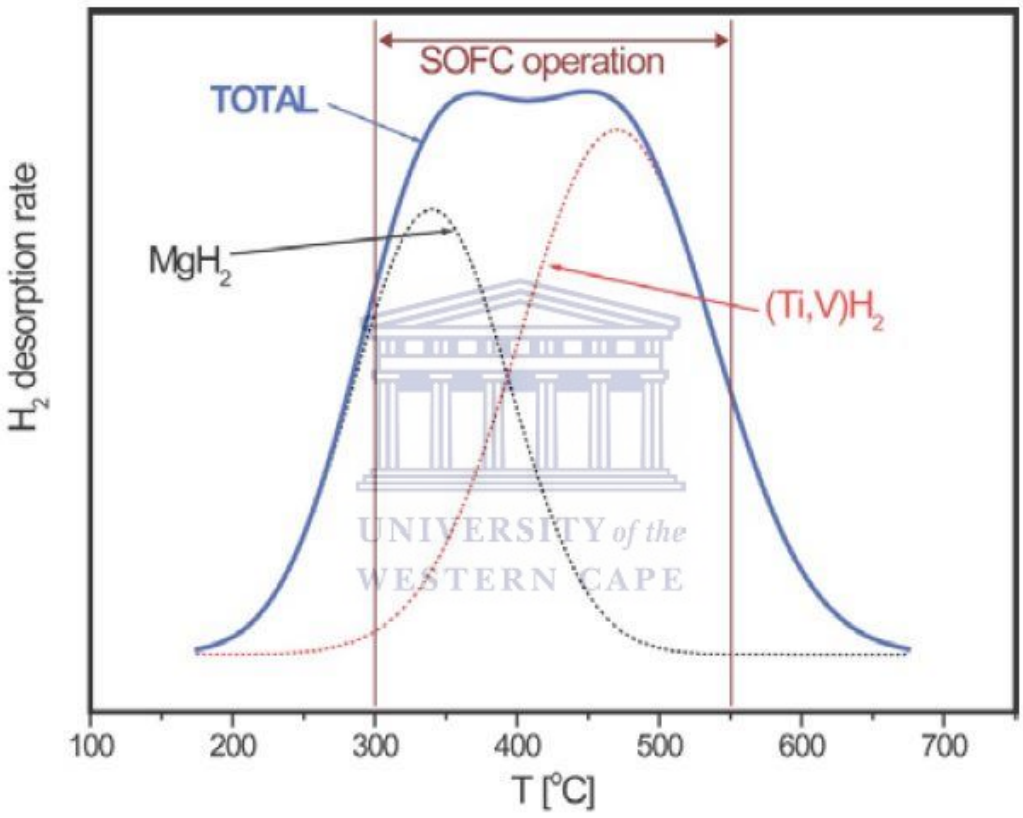

Figure 1.5: Intermediate operating temperature of MgH2 and (Ti,V)H2 corresponding with SOFC operating temperature; this behaviour is useful in engineering different combinations of metal hydrides to suit specific applications

1.5 Rationale of the Study

This study was initiated to explore the potential of various alternative materials in forming Mg binary alloys with good hydrogen interaction and thermodynamic properties. In the preceding work done by J. M. Sibanyoni, he outlined the specific objectives as follows:

- To improve hydrogenation performance of Mg via methods such as ball milling,
- To develop lightweight hydrogen storage materials with mild operating parameters i.e. fast hydrogenation at low temperatures and pressures, and
- To outline and identify promising uses and applications for the developed materials [26]

The abovementioned objectives remain valid for this study. The research undertaken in this study and the previous related study serves to provide a deeper understanding of intrinsic kinetics and mechanisms of hydrogen absorption/desorption on Mg based nanocomposites. The use of 'unwanted' or 'waste' materials as co-alloying material for Mg provides an economically viable alternative to pure additives which are rare and expensive. Generally, ferrovanadium has a market value more than 10 times lesser than pure refined vanadium. As such, ferrovanadium is a low cost alternative and further provides trace amounts of Fe (known catalyst for hydrogen absorption in Mg) that potentially improve hydrogen sorption performance of Mg.

In the process of investigating the effects of ferrovanadium as an additive to Mg for the purpose of hydrogen storage, it is also hoped that the results obtained in this study could also contribute to the overall understanding of Mg based hydrogen storage composites and provide insights into dealing with corresponding materials.

Furthermore, the co-alloying between Mg and Ti hydride materials provide additional insight towards diversifying the application of metal hydride materials as well as tailoring and improving their critical characteristics such as hydrogen sorption performance and cycle life.

2.0 Background & Literature Review

This chapter provides some general background information on Magnesium (Mg) as an element, followed by its relevance to hydrogen storage. An in-depth review of trends and developments with regards to hydrogen storage is presented, as well as preparation/processing methods and techniques uncovered through ongoing research of Mg and its composites. Selected results of Mg composites performance as a hydrogen storage material are also highlighted.

2.1 Brief overview of Mg

Mg is classified as an alkaline earth metal and is found in the second group of the periodic table of elements. It has the atomic number 12 and has the atomic weight 24.305 g/mol. It also has an oxidation number of +2 (being in the second group), and this relates to high chemical reactivity. As a result, Mg is never found as a free element in nature despite being the seventh most abundant element on earth and the eighth most abundant element in the universe [27]. In fact, elemental Mg was first isolated by Sir Humphry Davy in 1808, almost 200 years after its discovery in the form of Epsom salt [28].

Since its discovery, Mg has found widespread application from lightweight and strong alloys to pyrotechnics. Magnesium oxide (MgO), which is the second most abundant compound in the earth's crust, is also highly useful in the field of medicine and metallurgy. The Tables 2.1 and 2.2 indicate that Mg forms numerous compounds and is typically reactive when heated.

2.1.1 Physical & Chemical Properties of Mg

The following tables list the common physical and chemical properties of Mg [29].

Phase	Solid
Colour	Silvery-white metal
Crystalline structure	Hexagonal (a=0.320927 nm, c=0.521033 nm @ 25 °C)
Ductility	Can be beaten into extremely thin sheets

Malleability	Can be bent and shaped
Hardness	2.0 on Mohr's scale
Melting point	651 °C
Boiling point	1100 °C

Table 2.1: Physical properties of Mg

Compounds formed	Oxide, hydroxide, chloride, carbonate, sulfate
Flammability	Burns in air with a bright white light
Reactivity	With heating, reacts with halogens to yield halides
Alloys	Light but very strong
Oxidation	Combines with oxygen at 25 °C to form thin MgO skin

Table 2.2: Chemical properties of Mg

Briefly summarised, Mg is a relatively ductile metal that is softer than Fe, Pd and carbon, but not graphite [30]. It is highly reactive with heating, but reactivity tends to be dampened by oxide layers that form on the surface upon contact with atmosphere.

2.1.2 Surface interactions between Mg and hydrogen

Hydrogen adsorption does not occur on pure Mg surfaces; the activation energy associated with adsorption is highly linked to the geometry of the adsorption site [31]. Jian et al. showed using first-principle calculations that hydrogen adsorption on clean Mg surfaces is typically weak physisorption and that a high energy barrier (1.3774 eV) is required for the dissociation of hydrogen into H atoms [32]. In a 2004 study led by Arboleda [33], it was shown that the sticking probabilities of hydrogen to metal surfaces were the highest for La, Ti and Mg in descending order. More recently in a study aiming to replicate interstellar dust particles, the interaction between hydrogen and Mg_2SiO_4 forsterite (010) was investigated. Researchers noted that that the hydrogen atom attached via chemisorption to the forsterite (010), correspondingly resulting in an alteration of the Mg ion which directly binds the second hydrogen atom, also via chemisorption [34].

These findings imply that Mg is a good medium for hydrogen storage as hydrogen binds weakly to it and is thus easily removed (reversible storage), while the use of Mg and transition metal compounds provide an energetically favourable pathway for the dissociation hydrogen molecules and subsequent binding of hydrogen atoms.

2.2 Phases of MgH_2

MgH_2 is understood to exist in three basic phases, denoted as α, β and γ. The α-Mg phase is the raw state of low-pressure MgH_2, where fresh nucleation is seen to occur. The β-MgH_2 and γ-MgH_2 phases are separate states defined by the stability of hydrogen atoms embedded in the Mg lattice structure; the stability of hydrogen atoms embedded in the Mg lattice is largely a function of the hydrogen pressure imposed on the material at a given temperature. Although these phases are generally agreed upon, there are other transitional phases that have also been studied. For example, Durandurdu discovered through simulations that the rutile structure of α-MgH_2 transforms into a $CaCl_2$ structure when hydrogen pressure is increased [35].

The phases of MgH_2 may have differing structural and chemical properties, but the energy requirement to remove one hydrogen atom from the lattice is the same i.e. 4.0 eV [36]. However, transitions from one phase to another have been studied with inconclusive results. As pointed out by Moser et al. density functional theory (DFT) studies have not been able to reconcile the specific conditions at which one phase of MgH_2 transforms to another [37]. Table 2.3 below shows a simple summary of discrepancies in the outcomes of DFT calculations for phase transformations of MgH_2.

Investigators	Pressure for α to β transformation	Pressure for γ to β transformation	Comments
Cui et al. [38]	1.2 GPa	9.7 GPa	T = 0 K
Vajeeston et al. [39]	0.39 GPa	3.9 GPa	T = 0 K
Vajeeston et al. [40]	5.5 GPa	9 GPa	Room temperature
Bastide et al. [41]	2-8 GPa	-	α and β phase both present in this range
Bortz et al. [42]	> 2 GPa	-	No full transformation even at T = 1000 K

Kohlmann et al. [43]	> 9.3 GPa	-	No α to β transformation even at 9.3 GPa
Moser et al. [44]	4.3 GPa	-	T = 450 K

Table 2.3: Summary of DFT calculation results on conditions of MgH2 phase transformation

Despite the results of studies of phase transitions being quite conflicting, a general consensus can be made about the stability of each phase as well as their physical properties.

2.2.1 The α-MgH_2 phase

The α-MgH_2 phase is one that typically occurs at the start of hydrogenation. It has been shown to have a TiO_2 rutile crystal structure at low temperatures and pressures [41]. The unit cell parameters were measured experimentally to be *a*=4.501 Å, *b*=4.501 Å and *c*=3.010 Å at ambient conditions [42], [45]. The α-MgH_2 tetragonal unit cell structure is shown in Figure 2.1 below.

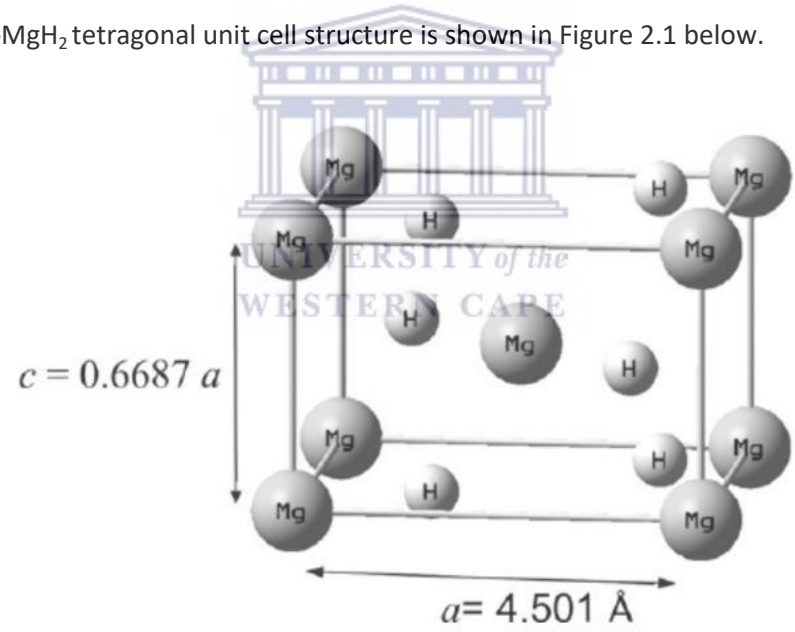

Figure 2.1: Tetragonal unit cell of α-MgH2 (rutile structure) [46]

2.2.2 The β-MgH_2 phase

The β-MgH_2 phase is typically characterised as a cubic modified CaF_2 crystal (Figure 2.3). The lattice parameters measured using synchrotron XRD produced values of *a*=4.5180 Å and *c*=3.0211 Å, while

the powder diffraction file JCPDS 12-0697 provides corresponding values of *a*=4.5170 Å and *c*=3.0205 Å [47]. The density of the β-MgH_2 phase was reported by Semenenko et al. to be 1.42x10^3 kg/m^3 [48].

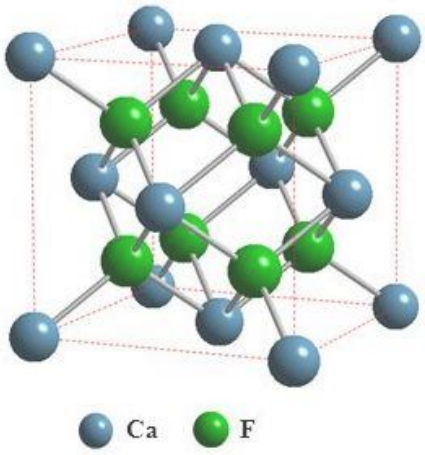

Figure 2.3: Unit cell of a cubic modified CaF2 crystal, analogous to the β-MgH2 phase [49]

It is also the most stable of the three known MgH_2 phases, typified by slow hydrogen diffusion kinetics. The diffusion coefficient of hydrogen in this phase has been shown to less than 2.5 x 10^{-13} m^2/s at ca. 350 °C [50]. Other studies have recorded even lower values at correspondingly lower temperatures [51]. Furthermore, slow hydrogen diffusion results in many sections of the Mg bulk left unreacted unless a substantially long duration is permitted.

2.2.3 The γ- MgH_2 phase

γ-MgH_2 exists as a metastable orthorhombic phase, transforming from the tetragonal structure of β-MgH_2 under high compression. While some groups have used high hydrogen pressures and temperatures to transform the α- MgH_2 phase into the γ-MgH_2 [41], [42]; several studies have shown that γ-MgH_2 forms during ball milling under low pressure hydrogen atmosphere [52], [53], also known as reactive ball milling.

Figure 2.4 shows the orthorhombic α-PbO_2 unit cell structure of γ-MgH_2; lattice parameters were measured by Bastide et al. using XRD analysis to be *a*=4.53 Å, *b*=5.44 Å and *c*=4.93 Å [41]. They also noted that β-MgH_2 transformed into γ-MgH_2 when pressure was released. The density of the γ-MgH_2 phase has been reported to be 1.43 x 10^3 kg/m^3 [48].

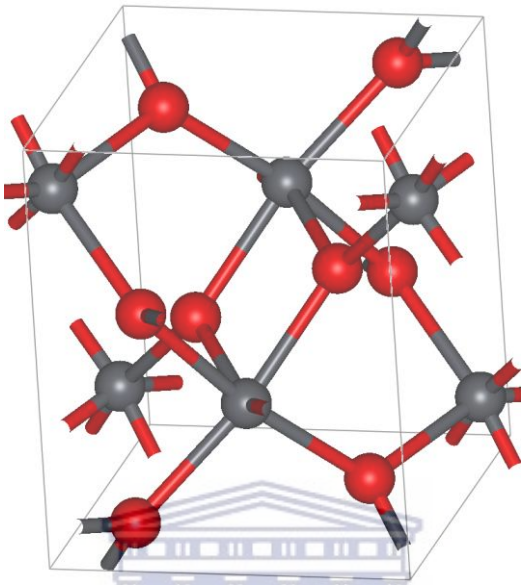

Figure 2.4: Unit cell of an orthorhombic α-PbO2, representative of the γ-MgH2 crystal structure [54]

2.2.4 Phase transitions

The transformation from Mg to α-MgH_2 is typically represented in the form of a Pressure-Concentration-Temperature (PCT) isotherm. An ideal hydrogen absorption/desorption isotherm would show a flat plateau as hydrogen concentration increases, during which phase conversion occurs. This is not the case in practical terms as a sloped plateau is generally observed experimentally, as shown in Figure 2.2 (A) and (B). The plateau slopes are even more obvious for intermetallic systems, thus suggesting that its presence and severity may be due to the degree of inhomogeneity of the sample.

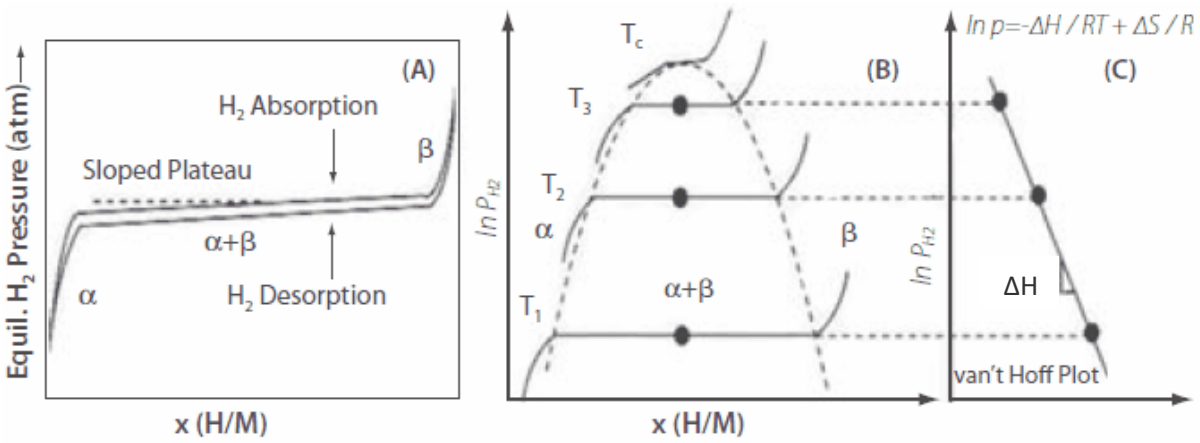

Figure 2.2: (A) Hydrogen absorption and desorption isotherm, showing a sloped plateau (as is practical) and hysteresis; (B) PCT isotherm illustrating the three-way relationship between plateau pressure, temperature and concentration affecting the transformation from α-solid solution of hydrogen in a parent metal to β-hydride, and (C) van't Hoff plot with slope corresponding to the enthalpy of hydride formation [55]

2.3 Formation and decomposition of MgH_2

The formation and decomposition mechanisms of MgH_2 have been the subject of much study without unanimous conclusions [56]. Generally, the decomposition of MgH_2 is a simpler process than formation. The formation of MgH_2 and Mg composite hydrides is typically exothermic whereas decomposition is usually endothermic and requires heat input to initiate hydrogen desorption.

2.3.1 Formation of MgH_2

Schimmel et al. [57] describes the hydrogenation of magnesium as follows:

1) Hydrogen gas flows into and through the bulk
2) Hydrogen adsorbs to surfaces and dissociates
3) Hydrogen atoms migrate from the surface into Mg/MgH2
4) Hydride phase nucleates and grows
5) Hydride phase diffuses into the bulk

There is a general consensus that the MgH_2 is formed via nucleation and growth [58], [59]. Upon contact with magnesium, hydride regions form independently near the magnesium bulk surface.

These regions typically occur in regions of the highest hydrogen concentration and lowest activation energy for nucleation [60]. As more MgH_2 is formed the nuclei extends further into the metal as well as along the surface. Hydride propagation in both directions proceeds at similar speeds and is not limited or controlled by grain boundaries. In fact, the absorption reaction is limited by the critical penetration depth of hydrogen and as such, MgH_2 formation stops at about 30 - 50 µm [61]. Figure 2.5 is a simple representation of nucleation and growth in MgH_2.

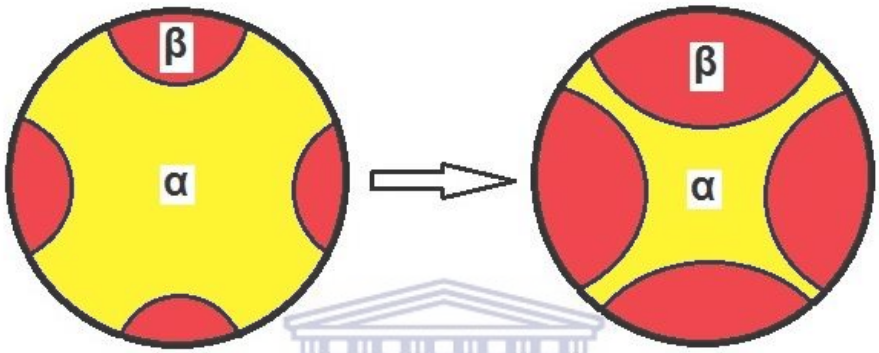

Figure 2.5: Schematic of MgH2 formation with low nucleation rate

It was noted by Vigeholm et al. that the formation of surface nuclei is the rate determining process of hydride formation [62]. Nucleation rates may differ based on pressure, surface passivation, low driving force etc. Low nucleation rates are typically represented by fewer nuclei formed on the surface, represented by the red hemispheres in Figure 2.5. Faster nucleation rates would be represented by more nuclei forming at the surface and forming a 'skin' that blocks further entry of hydrogen into the particle [61], [63]. In their effort to characterise the diffusion of hydrogen through Mg, Spatz et al. deposited Mg thin films onto previously hydride thick Pd-foil [64]. With the assumption that hydrogen only diffuses through the non-hydrided parts of the film, they successfully quantified the diffusion coefficient of hydrogen in Mg as $D = 1.1 \times 10^{-20}\ m^2/s$, at T = 305 K.

Previous studies have shown that ball milling causes a higher rate of nucleation by increasing grain defects while reducing particle size [62].

2.3.2 Decomposition of MgH_2

Desorption is not simply the reverse process of nucleation, even though MgH_2 decomposes and hydrogen is evolved. Mooij and Dam suggested that desorption of hydrogen could involve the appearance of voids, which is more favourable energetically than multilayer deformation [65]. Given enough time under the correct conditions, desorption will occur until all hydrogen previously present in the sample is released [62]. Decomposition kinetics of MgH_2 have been shown to be increased by the presence of of carbon materials in the composite [66]. Over two separate studies, Gasan and colleagues [67], [68] made a few important connections and conclusions:

1) Hydrogen desorption temperatures are dependent on particle size and specific surface area of MgH_2 powders
2) The addition of 5 wt. % V, Nb, Ti and G to MgH_2 resulted in up to a 50 °C decrease in desorption temperature as compared to commercial MgH_2
3) The was no clear correlation between crystallite size and hydrogen desorption temperatures

However, in the work reported by Checchetto and Bazzanella, they noted that transition metal doped Mg samples showed an improvement in hydrogen desorption properties that were attributed to the extended interfaces between MgH_2 and the transition metal nanoclusters acting as heterogenous nucleation sites with reduced activation energy and fast hydrogen atom delivery [69], [70].

2.4 Mg based hydrogen storage systems

Mg also reacts with hydrogen to form MgH_2. This compound has a hydrogen storage capacity of 7.6 wt. % that is highly enviable in the development of hydrogen storage materials. The challenge associated with MgH_2 is poor absorption and desorption kinetics, even at temperatures in excess of

300 °C. This is primarily caused by high thermal stability of MgH_2 due to high formation enthalpy (75 kJ/mol H_2).

2.4.1 Methods and techniques to improve the hydrogenation of Mg

The hydrogenation of Mg is typically hindered by several factors. Physical factors such as the formation of a passivated oxide layer on the surface prevents the permeation of hydrogen molecules [71]. Physical factors tend to also influence chemical factors such as hydrogen dissociation. Hydrogen dissociation on pure Mg surfaces is known to be poor and is a rate-limiting step for hydrogen absorption and subsequently impedes the diffusion of atomic hydrogen into the metal [31].

Several methods have been attempted to optimise and improve the hydrogen storage capacity and kinetics of Mg nanocomposites with varying degrees of success. It is generally understood that irregular and imperfect surfaces of Mg more readily absorb hydrogen, alluding to the fabrication process. Some effective methods include synthesis techniques such as ball milling [71]–[75], melt-spinning [76], [77], ultrahigh-energy-high-pressure milling [78], [79] and thin-film formation [80], [81]. Non-synthesis methods involve the addition of materials with known catalytic effects toward hydrogen storage, such as transition metals [53], [82], carbon materials [83]–[85], halides and intermetallic compounds [86], [87]. It has been noted that catalysts are added to improve hydrogenation and dehydrogenation kinetics but not alter reaction thermodynamics [88]. As such, the Mg-based nanocomposites were still non-operational at temperatures below 300 °C.

Note: High-energy reactive ball milling in hydrogen (HRBM) was used to produce all samples in this study and will be addressed in the following section of this chapter.

2.4.2 MgH_2 – transition metal systems

In a study report by Hanada et al., it was shown that small additions of Fe, Co, Ni and Cu nanoparticles (separately) to MgH_2 resulted in improved hydrogen desorption properties over MgH_2 [82]. In fact, another group observed that transition metals were able to improve hydrogen

desorption performance even at tiny concentrations (0.06 at. %), indicating that these metals were dispersed at an atomic level. Furthermore, they also found that cyclic stability was stable when transition metal nanoclusters were maintained in the range of 10-20 nm radius [70]. As such, there is a strong case for the use of transition metals as additives to improve the hydrogen storage performance of MgH_2.

2.4.2.1 Mg-V

Modelling studies performed by Yang et al. showed that vanadium coated Mg nanoblades could improve hydrogen desorption and absorption kinetics, with the rate limiting step being the rate of hydrogen generation by the vanadium catalyst [89]. A diagram of the modelled Mg nanoblade is shown in Figure 2.6. He et al. conducted experimental work with Mg nanoblades using a glancing angle (co)deposition technique to coat the Mg surface with V catalysts, concluding that the angle of deposition affects the hydrogen storage performance besides the porosity of Mg [90]. Mg-V composites could also be produced via ball milling and it was noted by Schimmel et al. that V breaks up into smaller particles than Nb during ball milling, providing more active sites for catalysis on the surface of Mg particles [57].

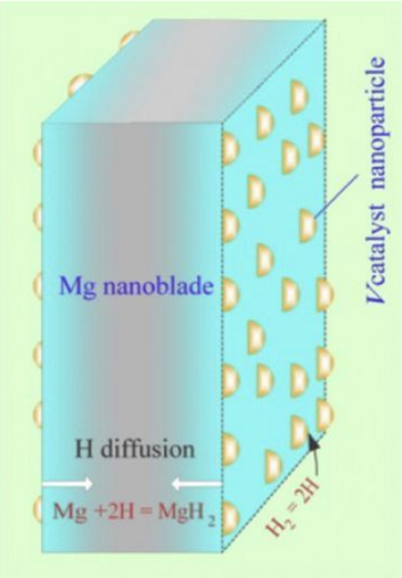

Figure 2.6: Schematic of Mg nanoblade with V catalysts undergoing hydrogenation [89]

The hydrogenation of Mg-V nanocomposites occur separately [57] and at different rates. Lototskyy et al. showed that vanadium monohydride (VH) formed more quickly than α–MgH_2 during hydrogenation [91], as seen in Figure 2.7. Consequently, desorption of hydrogen from VH also occurred at higher temperatures than from MgH_2.

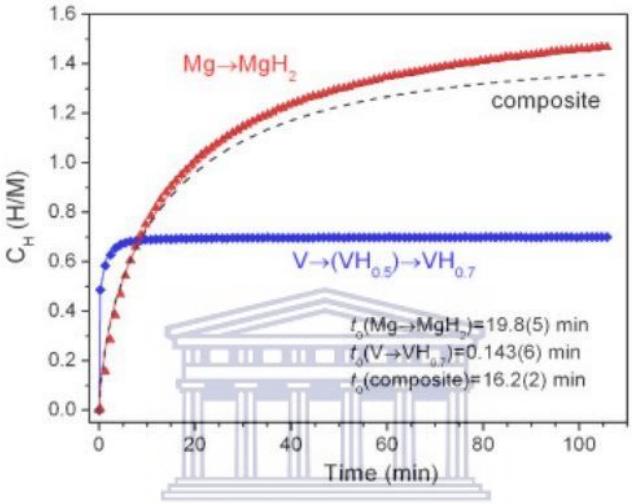

Figure 2.7: Hydrogenation profiles of Mg and V elements in the Mg-V composite [91]

Liang et al. [53] documented that the Mg–V nanocomposite released ca. 5 wt. % hydrogen under 200 s when heated to 300 °C; highlighting improvements in hydrogen storage properties when alloyed with transition metals. They further indicated that Mg-V demonstrated fast hydrogen kinetics with the hydrogen desorption activation energy of 62 kJ/mol H_2, less than half the energy required for MgH_2 [92]. In another study led by Liang, it was shown that ball milled MgH_2 – 5 at. % V released hydrogen at 473 K and reabsorbed hydrogen rapidly at room temperature [92].

2.4.2.2 Mg-Ti

Mg-Ti hydride binary alloys do not occur naturally due to the low boiling point of Mg (1091 °C) and high melting point of Ti (1668 °C). This was confirmed by Lu et al. in two separate works who showed via XRD analysis that metastable ternary Mg-Ti-H phases do not occur and what is observed is actually well dispersed mixtures of MgH_2 and TiH_2 [78], [79]. In terms of hydrogen desorption, MgH_2 peaks at about 300 °C while TiH_2 peaks at 450 °C yet the combination of the two produced via ultra-high-energy high pressure mechanical milling resulted in nano-sized Mg-Ti-H compounds with desorption temperatures below 250 °C [79]. A similar result (desorption temperatures below 250 °C) was also reported with $MgH_2/0.1TiH_2$ composites synthesised via ball milling under initial hydrogen pressures of 30 MPa [93]. In fact, early studies suggest that the formation of Mg-Ti composites using ball milling techniques require long durations or high pressures. Another example is the work by Asano et al. who produced Mg-Ti FCC hydrides from Mg-Ti BCC alloys at 8 MPa hydrogen pressure at 303 K for 270 hours and at 423 K for 122 hours [94].

Ti has been used to enhance the strength, hardness and Young's modulus of Mg composites. Rashad et al. noted that Mg-Ti composites did not form brittle inter-metallic compounds as shown in the Ti-Mg binary phase diagram [95]. Enhanced electrochemical activity was previously reported for thin film alloys of Mg – Ti (where Mg_yTi_{1-y}; $0.5 \leq y \leq 0.95$), better than that of pure Mg film and the $Mg_{0.8}Ti_{0.2}$ alloy even showed significant improvements in storage capacity and kinetics [80]. In a different study focused on binary Mg-Ti and ternary Mg-Ti-Ni materials, Lu et al. reported that the Ti shell displaced the MgO shell that typically coats Mg surfaces and effectively increased hydrogen absorption capacity of the composite [96]. The addition of Ti to Mg systems was also shown to prevent nanoparticle coalescence when the composite was produced using the inert gas condensation (IGC) method [97]. Calizzi et al. who similarly used the IGC method proved that higher Ti content reduces the crystallite size of β–MgH_2, besides minimising grain growth during cycling [98]. Finally, isothermal thermogravimetric analysis (TGA) has also been used to characterise hydrogen desorption of ball milled Mg-Ti-H composites. It was noted by Sohn and Emami [99] that

samples containing 1/7 and 1/10 molar ratio of TiH_2 to MgH_2 showed activation energies of 107-118 kJ/mol and significantly faster kinetics as compared to similarly prepared MgH_2 (226 kJ/mol).

The addition of Ti was also shown to improve the performance of other binary Mg nanocomposites. In the case of Mg/Pd multilayer thin films, Jung et al. indicated that the insertion of Ti interlayers between the Mg and Pd layers improved hydrogen storage capacity [100]. This is achieved by preventing Mg and Pd atoms from cross diffusion and forming intermetallic layers as seen in Figure 2.8, which is the typical problem associated with Mg/Pd systems [101]. Cyclic stability tests over 80 cycles also showed that the MgH_2-0.1TiH_2 nanocomposite suffered little loss of hydrogen storage capacity [78].

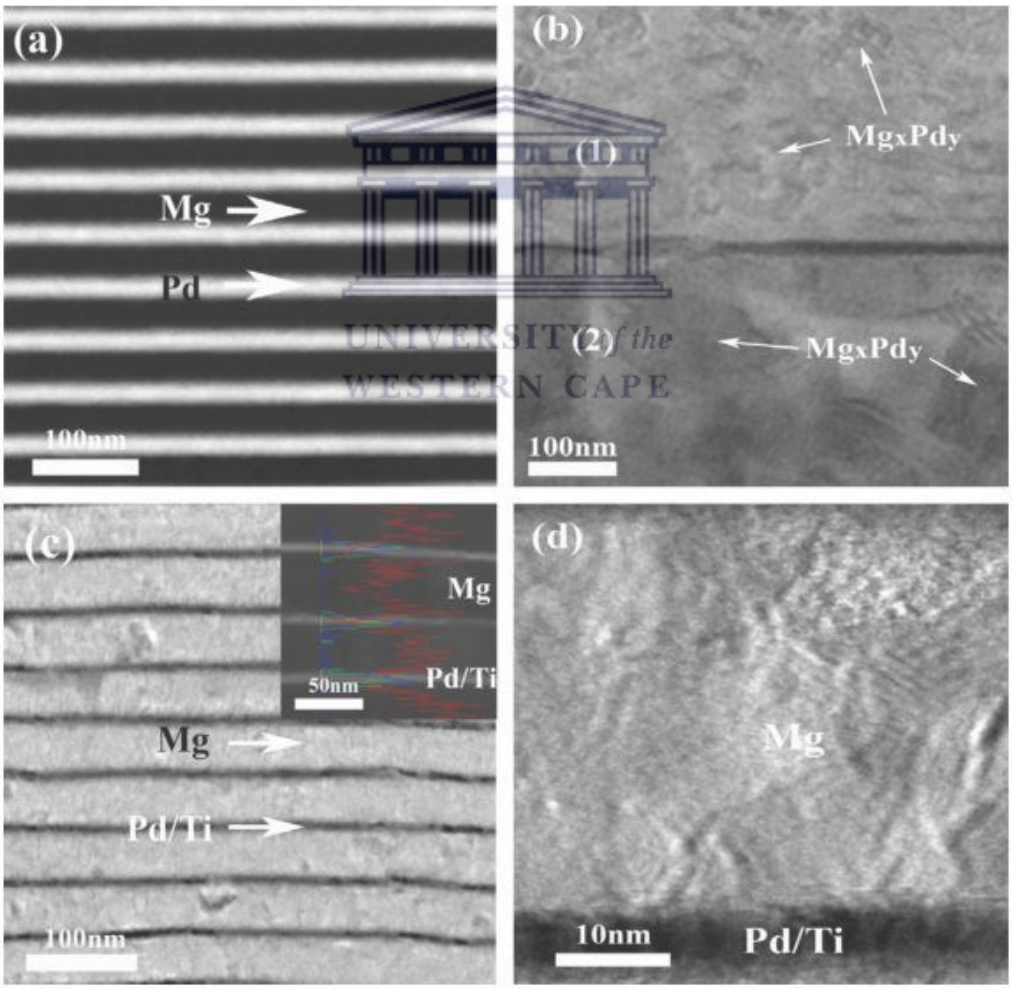

Figure 2.8: Cross-section TEM images (a) as-prepared Mg-Pd multilayers, (b) Mg-Pd multilayers after hydrogenation at 200 °C, (c) as-prepared Mg-Pd-Ti

multilayers with EDS inset, and (d) Mg-Pd-Ti multilayers after hydrogenation at 200 °C [100]

2.4.2.3 Mg-Ni

It was reported that Mg – 2 mol. % Ni prepared via soft milling for 15 minutes at 200 rpm desorbed more than 6 wt. % hydrogen in the range of 150 – 250 °C [82]. Jurczyk et al. synthesised Mg_2Ni hydride composites via ball milling followed by annealing; the composite slowly formed a ternary hydride at room temperature, it did not release hydrogen unless heated to 250 °C [102]. It was Liang et al. who suggested in [53] that the Mg – Ni interface acted as an active nucleation site for hydride formation. Ni has the ability to bind hydrogen molecules via chemisorption and dissociate it, transferring the hydrogen atoms to Mg. As such, it was recommended by Fujimoto et al. that the Mg and Ni possessed clean surfaces to maximise the interface. Their chosen fabrication method to achieve this state is through gas evaporation [103].

Density functional theory (DFT) methods have been used to model and understand the interaction of Ni and Mg. On such study by Kuklin et al. concluded that Ni atoms have a tendency to substitute Mg atoms in the subsurface layers. Furthermore, they indicated that the clusters of Ni atoms have a greater effect on the hydrogenation effect of Mg-Ni than the individual Ni atoms themselves [104].

In terms of cyclic stability, Hofmann et al. showed that the Ni doped Mg sample reached 5 – 6 wt. % capacity within 45 minutes and were stable over ca. 200 cycles [105]. In contrast the undoped Mg sample reached 2 – 3 wt. % in 45 minutes and 4 – 5 wt. % after 135 minutes. In a different study it was observed that Ni doped Mg performed differently from Mg-Ni composites that had been melted and crushed together. While the former is highly sensitive to high temperatures (practical temperatures above 420 °C were avoided), it showed a 36% drop in capacity over 4300 cycles at temperatures between 270 – 390 °C, attributed to particle sintering [106]. Mg2Ni produced via milling had a theoretical hydrogen storage capacity of 3.6 wt. % but had greater tolerance for high temperatures and decent cyclic stability. Figure 2.9 shows the cyclic stability of Mg_2Ni under 230 - 330 °C and 0.4-2.8 bar [107].

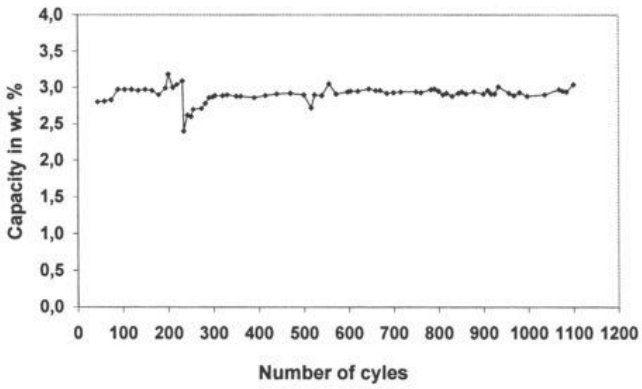

Figure 2.9: Cyclic stability of Mg2Ni prepare by melting and crushing [107]

2.4.2.4 Mg-Co

Mg-Co nanocomposites have been prepared by ball milled, showing ca. 3 wt. % hydrogen absorption capacity and capable of absorbing hydrogen below 273 K [108]. Zolliker et al. commented that certain results published in literature indicated some hysteresis i.e. heat of dissociation 86 kJ/mol H_2 and heat of formation 60 kJ/mol H_2 [109]. Data published by Yvon et al. showed that Mg-Co showed low theoretical capacities when compared to MgH_2 but a high degree of thermodynamic stability such that the material was a suitable heat storage system [110]. Figure 2.10 illustrates the higher working temperatures of Mg-Co systems as compared to other systems.

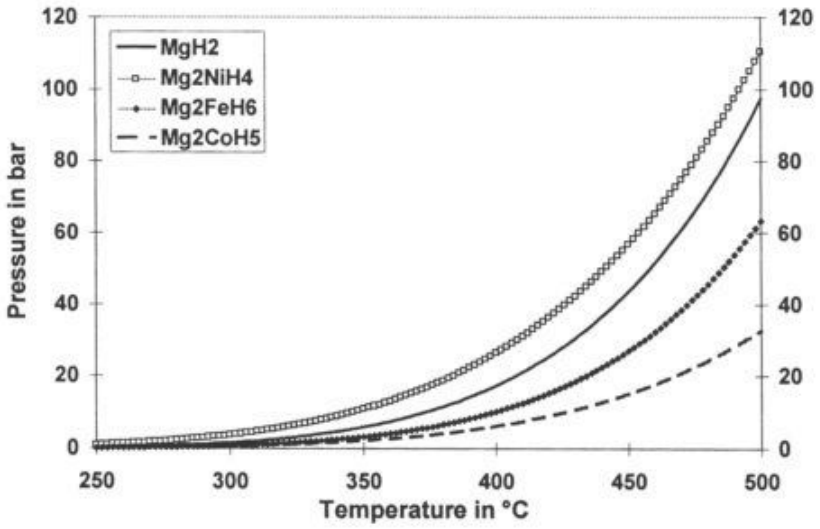

Figure2.10: Dissociation pressure-temperature diagram for different MgH2 systems [107]

Cyclic stability of Mg-Co (in the ratio of 2:1) was carried out by Reiser et al. and the material performed well for over 1000 cycles [107]. They presumed that during the cycling conditions $Mg_6Co_2H_{11}$ was partly formed which imparted greater stability to the system.

Interestingly, some controversy was noted over the existence and stability of Mg-Co and Mg_2Co compounds. Gennari and Castro attempted to investigate by using different synthesis methods to produce Mg-Co alloys; they concluded that kinetic factors may suppress the formation of MgCo in favour of Mg_2Co [111].

2.4.3 Addition of transition metal oxides

Oxides of transition metals have been studied for their catalytic contributions towards MgH_2 storage systems. A study conducted by Bormann et al. included oxides of Sc, Ti, V, Cr, Mn, Fe, Cu, Al and Si, prepared with MgH_2 using ball milling. This study concluded that the catalytic effect towards the hydrogen sorption kinetics of Mg was similar and that Fe_3O_4 had the biggest impact followed by V_2O_5. Interestingly, it was noted that it was in fact V_2O_5 instead of pure V that had the largest effect on desorption with hydrogen completely desorbed in 5 minutes at 300 °C [112]. In his review, Webb attributed the discrepancy between some of the previously mentioned works in Section 2.4.2.1 to the presence of small oxide impurities in V that positively affected results [113].

Separately, Barkhordarian et al. [114] studied Nb_2O_5 and demonstrated fast hydrogen sorption kinetics with nanocrystalline Mg doped with 0.2 mol.% Nb2O5. Up to 7 wt. % H capacity was effectively absorbed within 1 minute at 300 °C and conversely complete desorption took only 130 s. At lower temperatures, the absorption/desorption times were logically slower but still within 10 minutes.

In a study of cyclic stability, it was shown that milling MgH_2 with 10 wt. % Cr_2O_3 produced β–MgH_2 at about 30 nm. However, it was later illustrated via XRD, SEM and XPS that segregation of Cr_2O_3 to the interfaces between sintered Mg particles and reduction of Cr_2O_3 to Cr both contributed towards deteriorating hydrogen storage capacity over 150 cycles of desorption/absorption [115].

Most interestingly, transition metal oxides appear to have a synergistic effect when added with carbon to MgH_2 systems [116, 117]. This has been linked to the role of carbon in transferring H atoms from the surface of the catalyst and bulk Mg [118]. More information pertaining to the role of carbon will be discussed in the next section.

2.4.4 Addition of carbon species to Mg based nanocomposites

Several studies have explored the potential of carbon based materials as milling additives for intermetallic hydrogen storage nanocomposites or even on its own. These carbon materials include activated carbon, graphite, single-walled carbon nanotubes, multi-walled carbon nanotubes etc. One study by Imamura et al. successfully produced graphite-magnesium nanocomposites via ball milling that showed hydrogen absorption on dangling carbon surfaces in the form of C – H bonds [119]. In another study, the addition of carbon materials to Mg prior to ball milling resulted in faster hydrogenation kinetics as compared to pure Mg powders [120]. Figure 2.11 shows the hydrogenation profiles of Mg and various carbon materials.

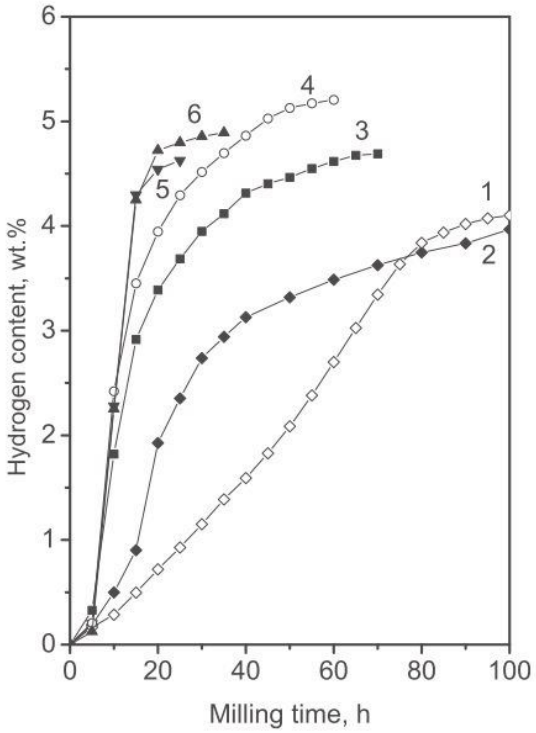

Figure 2.11: Ball milling hydrogenation of (1) Pure Mg, (2) Mg – Graphite (low specific surface area), (3) Mg – Carbon nanotubes, (4) Mg - Ultrafine diamonds, (5) Mg – Graphite (high specific surface area i.e. 176.4 m^2/g), and (6) Mg - Amorphous carbon [120]

Carbon has been used extensively as a milling additive. According to Zhou et al. [121], carbon has several roles in ball milling:

1) Dispersing agent that prevents cold welding of Mg when carbon additive was more than 30 wt. %
2) Lubricant to produce regular shaped MgH_2 (especially in the case of graphite sheets)
3) Milling media that aids milling and reduces milling time (due to sharp particles with protrusions on carbon structure)

In a more recent study, it was shown that the addition of carbon species milled with Mg resulted in improved hydrogenation kinetics [116]. However, it was also concluded that carbon did not act as a catalyst for hydrogenation of Mg but had an intermediary role for hydrogen transport. This finding is

in agreement with an earlier study where investigators, using DSC methods showed that were not catalytically active in Mg-C composites as there was no corresponding improvement in hydrogenation behaviour with increasing surface area [122]. To clarify, increasing surface due to improved porosity would increase the number of active catalytic site which would result in an improvement in hydrogenation behaviour. In 2014, Zhou et al. studied the effect of carbon from anthracite coal on the decomposition kinetics of magnesium hydride, concluding that the formation of nucleation sites on MgH_2-carbon boundaries was easier than in the MgH_2 bulk [66]. It was also shown that the addition of graphene nanoplatelets (GNP) improved the strength and ductility of Mg – 10 wt. % Ti due to higher specific surface area and adhesion of GNPs [95]. Carbon additives may also prevent or control the agglomeration of Mg particles during cycling under heat [121].

In terms of using carbon as a storage vector, Cao et al. performed modelling studies and informed that single-walled carbon nanotubes (SWNT) could store up to 7.4 wt. % or 62.2 kg/m^3 hydrogen [123]. This avenue of research was again highlighted by Dillon et al. who showed that hydrogen could condense to high density within narrow SWNTs [124]. In 2014, Zhou and his team reported that FTIR analysis confirmed that carbon could store hydrogen by forming C-H which dissociates more easily than in MgH_2 [66]. As such, carbon may contribute slightly to the storage capacity of the material.

2.4.5 Addition of transition metals/alloys to MgH_2

The development of effective and suitable MgH_2 nanocomposites has provided much insight into the roles of different metals in influencing the composite. For example, Mg_2NiH_4 possesses good hydriding and dehydriding rates while Fe is known to provide active sites for chemisorption and dissociation of hydrogen molecules [125]. Ti is much harder than Mg and is expected to aid in particle refinement, besides forming TiH_2 which also aids in particle refinement. On their own, transition metals tend to have the highest storage volumetric storage capacity of ca. 1500 cm^3 H_2 /cm^3 hydride [126].

Bazanella et al. showed in 2011 that the addition of Fe and Zr further enhanced the desorption kinetics of MgH_2 as compared to each additive individually [70]. In an earlier study, the Mg–(10 wt. % Ni)–(5 wt. % Fe)–(5 wt. % Ti) composite prepared using ball milling exhibited good hydriding and dehydriding kinetics [127]. Mg-Ni-Fe composites were also produced via melt spinning and ball milling, showing superior desorption kinetics over both its components [76] and the Mg-Ni-Fe-Ti composites previously mentioned as well [127]. A study of $TiFeO_3$ has also shown that it is an excellent dispersing agent that helped prevent the agglomeration of Mg particles besides aiding in the refinement of particles during ball milling [26].

In the scope of this study, ferrovanadium (FeV) was selected as a cheap and easily available vanadium source. The use of FeV was previously documented by Yan et al. and they confirmed that it was a reliable alternative source for vanadium that improved hydrogen storage properties of alloys [128] besides lowering costs [129]. In Dou's study of using FeV to reduce the cost of Ti-V BCC alloys, he discovered that increasing FeV content resulted in decreasing lattice parameter and cell volume of the BCC phase that directly affected the hydrogen desorption capacity of the material [130]. This finding was confirmed by Santos and Huot who suggested that the reduction in cell volume of the BCC phase was caused by atomic radius of Fe being smaller than V [131]. They further indicated that although substituting V for FeV lowers the total hydrogen storage capacity, the modification of plateau pressures for desorption actually improves the reversible hydrogen storage capacity.

Titanium vanadium (TiV) alloys were also used in this study. A quick survey of literature revealed that TI-V systems differed from other intermetallic systems. The crystallinity of ball milled TiV did not depend on the starting material but rather the hydrogen pressure under which the mixture was milled. It was observed by Huot et al. [132] that at low (0.2 MPa) and high (1 MPa) pressures, BCC and FCC TiV were formed respectively. At intermediate hydrogen pressures, amorphous TiV was obtained.

2.5 High-Energy Reactive Ball Milling

Mechanical alloying is a powder processing technique that creates alloys without the direct application of heat to the elemental metal powders. This cold-alloying method was developed by J. S. Benjamin in an effort to produce a nickel base super-alloy for gas turbine applications in the 1960's [133]. Three processes occur to metal powders during mechanical alloying: cold-welding, fracturing and re-welding of powder particles. These three processes are effected by highly energetic compressive impact forces caused by collision of milling balls in a mill [133]. Mechanical alloying has been proven effective for synthesising equilibrium and non-equilibrium alloy phases starting from a mixture of elemental powders or pre-alloyed powders [134].

Ball milling differs from mechanical alloying conceptually in that actual alloying may not occur during ball milling, thus a reduction in particle size is the primary gain as opposed to producing alloys. This is a welcome effect for Mg based nanocomposites, as nanostructuring (caused by ball milling) has been shown to improve hydrogen storage properties in numerous studies [6–9].

2.5.1 Types of ball mills

There are several variants of ball mills, suited for different parameters and batch sizes. Among the more popular types of milling equipment are the attritor, horizontal ball mill, shaker mill, planetary ball mill and large diameter ball mill. Attritor and large diameter ball mill types are typically used for large batch sizes (1-1000 kg). Shaker mills and planetary ball mills are more suited for research purposes due to their ability to work with small amounts of powder.

The shaker mill is a highly energetic mill that effects movement in three perpendicular directions in excess of 1000 rpm. An example of this type of mill is the Spex 8000M Mixer/Mill®, capable of working with samples between 0.2 and 10 g with rotation speeds up to 1425 rpm [138].

Planetary ball mills (such as the one used in this study) are subjectively lower energy mills when compared to the shaker mills. The working mechanism of a planetary ball mill consists of one to four

milling bowls/vials seated on a rotating disc. During operation, the disc and the milling vials rotate in the opposite direction, resulting in alternately synchronised centrifugal forces [72]. In terms of movement, this translates to the milling balls sliding along the walls of vial before falling across and colliding with the opposite side of the vial. Suryanarayana, in his review of mechanical alloying and milling [134] terms these forces as friction forces (balls sliding along the vial wall) and impact forces (balls flying across the vial and striking the opposite side of the vial), as shown in Figure 2.12.

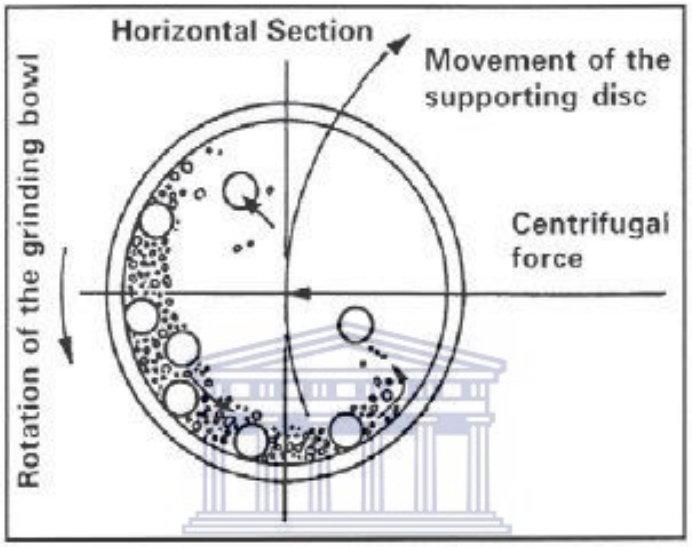

Figure 2.12: Schematic showing the movement of the milling vial (grinding bowl) and the rotating disc during milling operations [134]

2.5.2 Ball milling parameters

Several parameters are known to influence ball milling and have a consequence on the final milled product. These are milling duration, milling speed, the material of which the mill and balls are made of, the ball to powder ratio (BPR), milling atmosphere, type of mill etc.

In terms of milling duration, there is typically a critical milling time after which no further improvement is noted. This critical value differs depending on the other parameters (milling speed, BPR, ball and vial material) as well as the material being milled. One example for this: in [116] ball milled Mg achieves saturation after 5 hours but in [139] the critical milling time for Mg based nanocomposites is mentioned to be 10 hours. This difference reflects the numerous combinations

and permutations that may affect the critical milling duration, such that perhaps studies should in fact reflect a minimum effective milling durations instead. Furthermore, extended durations of milling have been shown to deteriorate the hydrogen storage performance of the material [14,15]. Figure 2.13 below is the overlayed x-ray diffraction patterns for MgH_2 milled at different durations. It is clearly seen that the conversion of β-MgH_2 to γ-MgH_2 occurs after 2 hours of milling. Correspondingly, MgO has also formed after this time. The peaks are also broad, pointing towards small crystallite sizes [52]. However, it is noticeable that the intensities for some β-MgH_2 peaks increase between 10 and 20 hours of milling, indicating a reversal in phase structure.

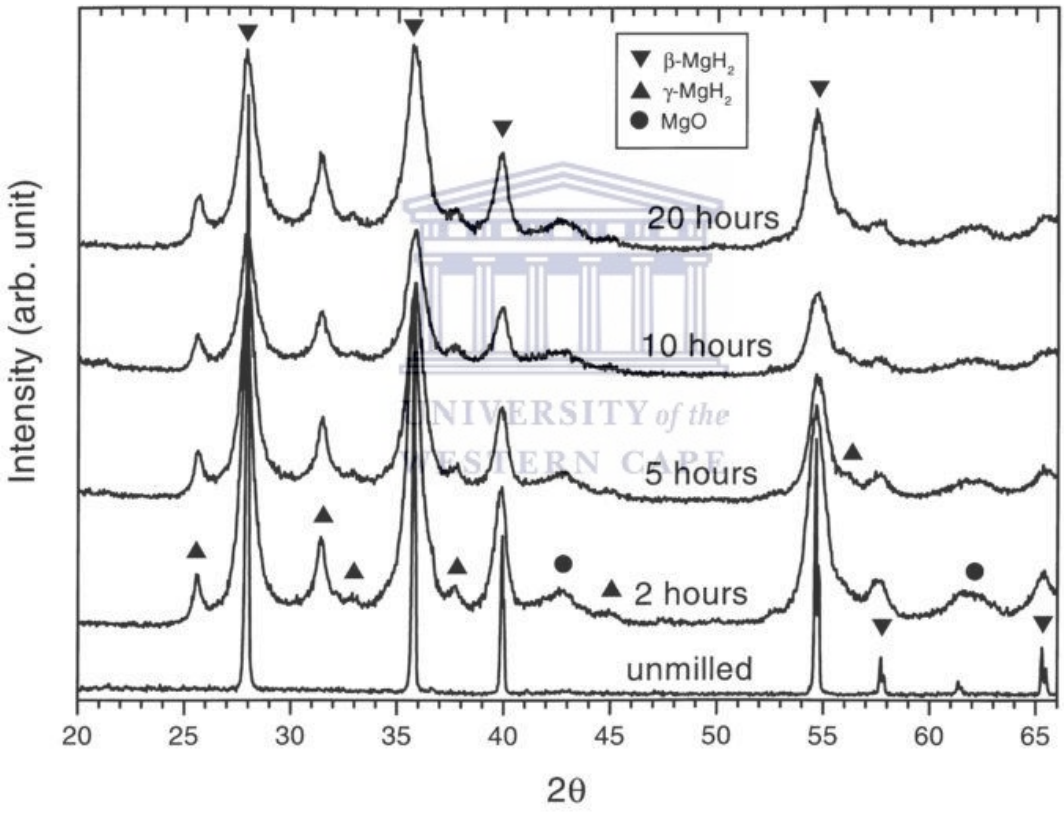

Figure 2.13: X-ray diffraction profiles of ball milled MgH2 with different milling times [52]

It is finally noted that excessive milling times tend to produce secondary effects that decrease the storage capacity and negatively impact the hydrogen absorption kinetics of the material [142]. In a

study of Mg – Nb_2O_5 – SWCNT and Mg – Nb_2O_5 – MWCNT, crystallite sizes decreased when milling up to 2 hours but steadily increased when milled to 4 hours. The investigators thus suggested that the continued shear and compressive forces throughout the milling duration resulted in particle refinement to the point where surface energy increased beyond a critical point that promoted Mg agglomeration [140].

Milling speed is directly proportional to the energy delivered into the system. However, due to the circular structure of the milling vial, excessive milling speeds will result in the milling balls just 'sticking' to the walls without impacting the material. This leads to plenty of friction forces but no impact force. As such, a critical speed exists below which both forces are present. Nath et al. also reported that increasing milling speed resulted in decreasing particle sizes for barium titanate powders, up to 18 nm after which no further size decrease was noted [141]. Furthermore, in an investigation that evaluated milling parameters and the statistical significance of each parameter towards the product, it was found that milling speed is the second most significant factor in the reduction of specific surface area [143]. Milling speeds also affect the temperature inside the vial.

The construction material of the vial and balls must be evaluated before any milling work is done. Due to the highly energetic nature of ball milling, contamination easily occurs if the wrong combination of milling media and milling equipment is used. Balls and milling vials are commonly made from stainless steel or tungsten carbide. These were both available at our facility and used for different purposes. In situations where iron contamination was detrimental to the product, tungsten carbide was the preferred option. The tungsten carbide mill was also used when the milling media was known to be harder than steel. However in certain cases, the presence of leeched iron from the milling vial assisted in the creation of nucleation sites to reduce particle size, similar to FeTi [86].

The ball to powder ratio (BPR) describes the weight ratio between the milling balls and material. Theoretically, the higher the BPR, the more energy is imparted to the material upon collision; thus affecting the ignition time, t_{ig}, described as the time at which a self-sustaining reaction begins and

propagates through the material [144]. Schaffer and McCormick discovered that the ignition time, which is the sum of all mechanical energy supplied to the vial, decreases as milling time increases, and also when the BPR increases [145].

Ball milling can be performed under hydrogen or argon atmosphere, or vacuum to minimise atmospheric contamination. It was demonstrated in [146] that milling under hydrogen atmosphere produced more reactive materials than under argon for Mg – 10 wt. % Co. This appears to be the case for most Mg based nanocomposites and even MgH_2 which is more brittle and resulted in even greater particle refinement. As such, milling serves two purposes: particle size reduction and hydrogenation. It was noted that the Mg – 10 wt. % Co sample milled in argon did not hydrogenate faster despite smaller grain size [146].

2.5.3 Conclusions about High Energy Reactive Ball Milling

Surface and interface contamination is potentially detrimental during ball milling preparation of nanomaterials. Contaminations can occur in several ways, for example atmospheric contamination of oxygen or moisture sensitive materials due to improper handling outside of the glovebox or a faulty 'O' ring leading to an imperfect seal on the milling vial. Besides this, stainless steel milling vials have also been known to leech trace amounts of iron (Fe) into the milling mix, although in the case of this study, the presence of iron in the nanocomposites was beneficial rather than a deterrent. Contaminations may be reduced and minimised by optimising milling speed and time, as well as maintaining operations within an inert glove box [72].

Ball milling is the most cost-efficient and effective method for synthesising Mg nanocomposites in ambient conditions without excessive energy requirements. Although there are several parameters that need to be considered, the simplicity of method allows for quick and accurate application. Ball milling is able to shorten the timescale of composite synthesis from days to hours, and the efficacy of the process is largely reliant on the milling energy, which in turn is determined by the ball milling parameters. It was noted by Huot et al. that the embrittlement caused by hydrogen absorption

(when milling under pressurised hydrogen atmosphere) motivates particle refinement and quick synthesis of binary metal hydrides. For ternary hydride synthesis via ball milling, other factors such as cold-welding and interface diffusion become more important [132].

2.6 Conclusion of Literature Review

Mg possesses the suitable qualities to be a premier hydrogen storage material – it is easily available in abundance, cheap, lightweight and high hydrogen storage capacity. This combination of positive attributes has driven urgent research in the area of Mg based hydrogen storage materials in recent times.

There is no disputing the potential for MgH_2 nanocomposites to be a reliable and viable medium of hydrogen storage; the only challenge being hydrogen absorption and desorption kinetics as well as cyclic stability. The US DOE has set milestone targets for specific performance parameters (Appendix 1) as well as approaches to research and development of robust and efficient forms of hydrogen storage methods. This includes a short term plan focusing on improving compressed hydrogen storage and delivery methods, while the long term plan explores other hydrogen storage methods including sorbents and metal hydrides [147]. As such, there is no lack of effort, as the literature survey shows, in exploring a wide range of materials and intermetallic compounds as well as adjusting and developing synthesis methods that lead to favourable physical and chemical properties.

It has been shown conclusively that the combination of Mg and elements such as Fe, Ti and V produce compounds with vastly improved hydrogen absorption and desorption kinetics. The task remains to find a balance between kinetics and capacity as an improvement in one comes with a trade-off from the other. Besides exploring intermetallic combinations and their effects, research has also uncovered improvements related to the arrangement and orientation of the metal micro- and nanostructure. However, it remains uncertain how these methods may be scaled up for a larger production capacity.

Another aspect for consideration is the lifespan or cyclic stability of the material. High temperatures result in metal sintering, and thus reduced storage capacity over time. To be competitive with current status quo, hydrogen storage materials require a cycle life in excess of 1500 cycles from ¼ to full tank, according to US DOE targets. This proves to be quite the challenge as even at lower heating temperatures, cyclic stress greatly affects the physical integrity of metals and hydrogen storage performance deteriorates correspondingly.

3.0 Experimental Methodology

This chapter serves to introduce the design, approach and procedures for the preparation and characterisation of magnesium-based nanocomposites studied in this work. A detailed description of materials used will be provided as well as a discussion of sample preparation, characterisation methods and data analysis. Calibration procedures will be mentioned and experimental parameters will be clearly defined. Some issues faced during the course of experimentation and the subsequent remedial steps taken are also touched upon.

3.1 Scope of work

The work reported here covers the preparation and characterisation of magnesium based nanocomposites for hydrogen storage research. The metals and alloys chosen to be alloyed with magnesium were selected on the basis of application, economy, availability and previous performance. The intended application of the hydrogen storage material narrows down the choice the material combinations. While certain alloys interact with hydrogen at room temperature, hydrogen only desorbs from magnesium hydride (MgH_2) at temperatures in excess of 300 °C and for other materials such as titanium hydride (TiH_2) even higher temperatures are required to facilitate absorption and desorption of hydrogen. In the interest of feasibility of commercialisation of these hydrogen storage materials, considerations pertaining to cost are vital for any new technology to break into the market. Local availability is also an important factor linked with supply, cost and practicality. Finally, the performance of the novel material must be competitive with existing and benchmark materials for it to be even considered a candidate for success.

In this work, a few combinations of Mg nanocomposites were prepared and adequately characterised. The earliest work was performed on Mg and ilmenite ($FeTiO_3$), a continuation from a previous study. This was followed by Mg and ferrovanadium (FeV) as a complete study; a detailed list of samples prepared is given in the following section. As an extension of the study of Mg-FeV nanocomposites, carbonaceous materials were also added and tested, to interesting results. Finally

included in this thesis is the study performed on Mg-Ti which was intended for higher temperature applications.

3.2 Materials

The main component of all the nanocomposites prepared was 99.8 % Magnesium (325 mesh, Alfa Aesar). Among the other materials used to prepare the composite was 99.7 % Vanadium turnings (2.5 cm, metal basis). South African Ferro-Vanadium (FeV; ≥ 75 % V grade) was also used. The FeV was obtained locally from Insimbi Alloy Suppliers (Pty) Ltd. and were regarded as a by-product of the mining process. As such, this fulfilled two of the criteria mentioned above, namely low cost and local availability. The material took the form of a course black powder with shiny elements and the reported fraction composition corresponded to particle sizes of 0.075 – 0.5 mm.

Under observation via Scanning Electron Microscopy (SEM), the FeV particles were noted to have a cubic or cuboidal appearance between 0.1 mm and 0.5 mm in size. Energy Dispersive X-ray Spectroscopy or EDS analysis, shown in Figure 3.1 below, indicated that the vanadium content was about 77 % which matched the supplier specification. The material also contained impurities such as Si (ca. 4 %), Al (ca. 3 %), Ca (ca. 1 %) and Mg (ca. 0.6%), besides significant amounts of oxygen in the form of surface oxides.

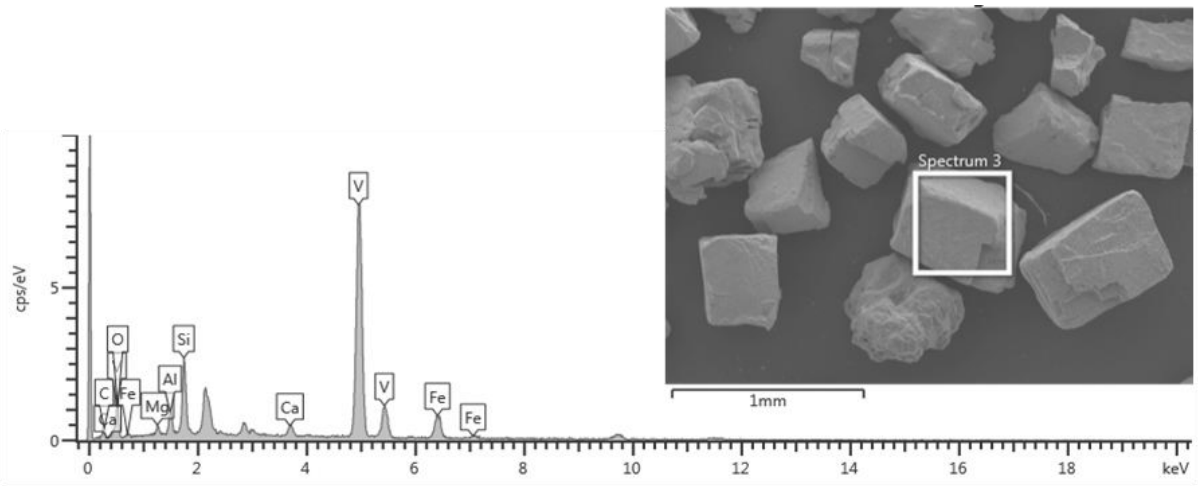

Figure 3.1: EDS spectrum and SEM image (inset) of ferro vanadium used in this study

A summary of EDS data is shown in Table 3.1 below. The data was obtained from four different sites (denoted as spectrum) of the raw FeV powder. It is also noted that the average V content is a match to the specifications (ca. 77 %). Furthermore, the impurities present do not exceed 4 wt. % which reflects a satisfactory level of control and consistency.

Spectrum	Components [wt. %]					
	V	Fe	Si	Al	Ca	Mg
1	69.7	22.5	1.4	4.4	0.8	1.2
2	73.4	12.8	7.9	2.8	1.8	1.3
3	85.4	12.6	0.3	1.8	0.0	0.0
4	77.8	12.3	6.0	2.5	1.3	0.0
Average	***76.6±6.7***	***15.1±5.0***	***3.9±3.6***	***2.9±1.1***	***1.0±0.8***	***0.6±0.7***

Table 3.1: EDS analyses on different sites on the sample (oxygen excluded)

The following nanoparticles were synthesised specifically for this study:

- Mg + 2 wt. % (FeV), or $Fe_{0.1857}V_{0.8143}$
- Mg + 5 wt. % (FeV)
- Mg + 10 wt. % (FeV)
- Mg + 20 wt. % (FeV)

In addition, one sample was chosen to be further added with carbonaceous material as follows:

- Mg + 10 wt. % (FeV) + 5 wt. % activated carbon (AC)
- Mg + 10 wt. % (FeV) + 5 wt. % multi-walled carbon nanotubes (MWCNT)
- Mg + 10 wt. % (FeV) + 5 wt. % graphite (G)

Activated carbon (YP-50F, coconut based, diameter 3-20 µm, surface area 1600-1700 m^2/g) was obtained from Kuraray Chemical Co. in Japan. The multi-walled carbon nanotubes were specified as diameter 5-20 nm, length 10 µm, aspect ratio > 500, bulk density 0.04-0.06 g/cm^3, with impurities of amorphous carbon and Fe (<10 %) present, obtained from Carbon Nano-material Technology Co.

(Korea). The graphite material was obtained from Fluka (99+ %, powder length ≤ 20 µm, bulk density 1.9 g/cm^3).

3.3 Sample preparation

A single preparation method was used for all samples in this study: high-energy reactive ball milling (HRBM). A survey of literature has revealed HRBM to be one of the simplest yet most effective methods of producing homogenous Mg nanocomposites [71], [148]–[150].

3.3.1 Setup for nanostructuring

Mechanical alloying describes the process of repeated welding and fracturing of cold metallic powders that eventually produces a homogenous alloy. This would typically be performed in a vial or ball milling jar which is subjected to vibrational or centrifugal forces. Mechanical alloying was developed by Benjamin and Volin [133] as a method to combine the advantages of precipitation hardening and oxide dispersion strengthening to improve the high-temperature strength in a nickel-base superalloy. Related but not synonymous to mechanical alloying is the process known as ball milling; mechanical alloying results in a homogenous alloy being produced whereas ball milling describes the reduction in particle size via mechanical means [134].

Mg composites were prepared using high-energy reactive ball milling (HRBM). In terms of the Mg and ferrovanadium samples, HRBM ensured consistent particle sizes in the nano-scale (< 100 nm) and created the necessary grain defects that promote the diffusion of hydrogen into the material. HRBM with harder materials such as pure titanium, vanadium and their alloys required a preparatory step to crush the material into sufficiently small particle sizes before milling with larger weight ratio of magnesium.

Numerous parameters dictate the final outcome of the milled powders. These include the type of milling apparatus used, material of the vial and milling balls, milling speed, ball-to-powder (BPR)

weight ratio, milling atmosphere and milling duration. These have been explained in detail in the previous chapter.

Several types of mills are available commercially with differing working parameters and specific characteristics. The mill used in this study was a *Pulverisette 6* planetary mono mill by Fritsch GmbH. The *Pulverisette 6* grinds material by utilising opposing rotational forces; the milling vial spins in one direction while rotating around an axis in the opposite direction thus creating centrifugal force in alternate directions – Coriolis motion. Because of this, a forced tumbling action occurs at certain rotation speeds when the milling balls 'slide' down the inner wall creating a friction effect that is immediately followed by disengagement from wall and impacting the opposite side – impact effect [134]. The material is thus crushed by the balls impacting the wall as well as collision between milling balls.

The vial and milling balls can be made from various materials and is chosen based on hardness and reactivity with the powder to be milled. The vial used in this work was made from stainless steel and obtained from Evico-magnetics GmbH. Considering that the bulk of powder being milled was Mg (Mohr's hardness 2.0; relatively soft) stainless steel was adequate for milling operations. However, harder alloys such as TiV had to be crushed prior to milling in order to avoid causing abrasion and damage to the milling vial.

The rechargeable milling vial had integrated circuitry in the lid that allowed for remote monitoring of pressure and temperature *in situ* during milling. It has been noted that iron contamination can occur when using a steel vial. However, iron also has a catalytic effect on hydrogen absorption by magnesium.

Other parameters for ball milling include milling speed and duration. In general, a mill rotating faster (ω2 in Figure 3.2) has more energy input than a slower one. However if a critical rotation speed is exceeded the milling balls will be held on the walls of the vial by centrifugal force and thus negate

any impact on the powder. As such, the milling speed needs to be set below the critical value to impart maximum impact force from the greatest height.

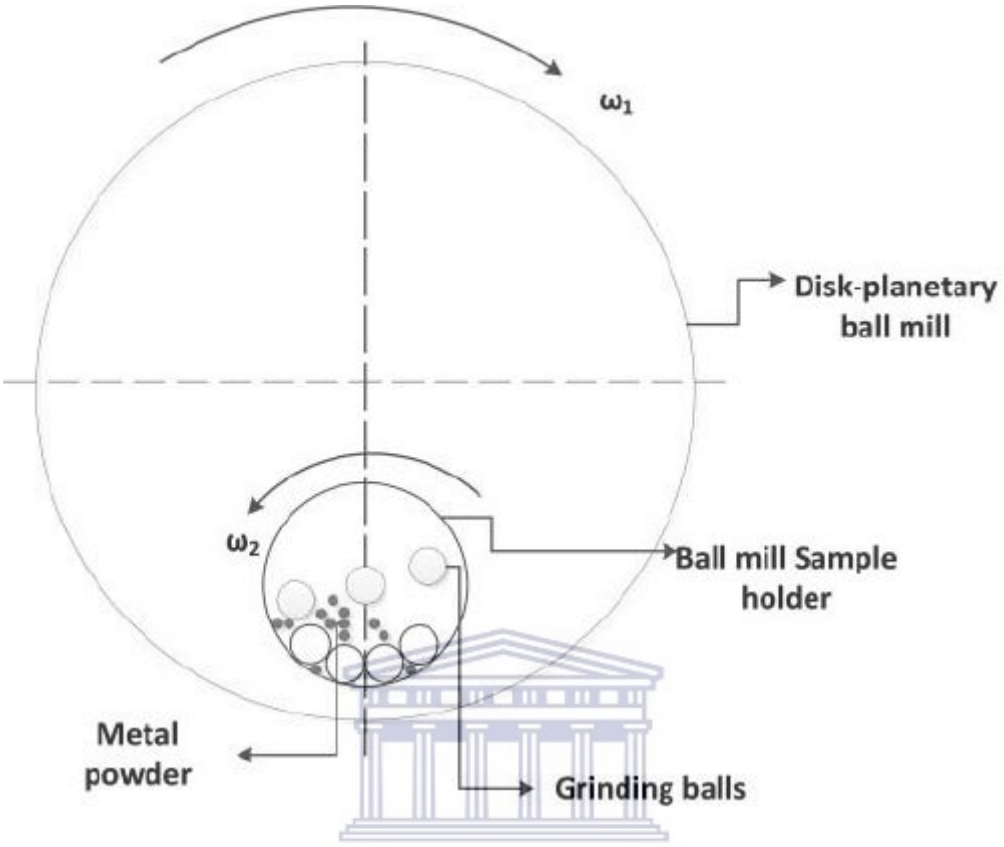

Figure 3.2: Schematic of ball movement inside the milling vial [151]

Milling speed and duration were also limited by the limiting temperature of the vial. As mentioned above, the Evico-magnetics vial had integrated circuitry built into the lid to monitor pressure and temperature. It was noted from the manual that temperatures in excess of 70°C would damage this circuitry. Furthermore, high temperatures during milling could be counter-productive to powder refinement as particle sintering may occur.

The ball to powder weight ratio (BPR) played an important role in influencing the efficiency of the nano-structuring process. It is seen as a determining factor to the size achievable by ball milling given other parameters being constant. In our study, the target BPR to achieve nano-sized material

was 40, specifically 40:1 in terms of total ball weight to material weight. To this effect, a fixed number of 82 stainless steel balls with 10 mm diameter.

In this work, 8 g of Mg was the base material with other additives between 2 – 20 wt. % with a further 5 wt. % carbonaceous material for the relevant samples. This preparation was done within the confines of an Argon glovebox to minimise contamination and oxidation of the materials. The ball to powder ratio (BPR) was between 33 and 40. Milling was performed at 500rpm for up to 5 hours in 30 minute intervals, allowing for sufficient cooling in order to record the pressure at normalised room temperature and also to preserve the circuitry of the vial (< 65 °C). Materials were also milled under 30 bar hydrogen atmosphere; hydrogen was refilled whenever the pressure dipped below 15 bar to maintain equilibrium pressure and drive the hydrogenation process. Upon completion of milling, the hydrogenated samples were carefully removed in a glovebox with argon atmosphere to avoid oxidation of Mg.

Note: In the case of pure Mg, HRBM was monitored without interruption similar to references [116], [152]. The comparison of the results with the ones taken after intermittent cooling showed a negligible difference and henceforth the abovementioned procedure was adopted.

3.4 Characterisation methods

For this work, several methods of characterisation were used to evaluate the as-prepared novel Mg composites with respect to their ability to store hydrogen. Several aspects were considered, relating to performance expectations of the material in a commercial application, such as gravimetric and volumetric hydrogen storage capacity, kinetics, cyclic stability, absorption and desorption temperatures.

3.4.1 Thermogravimetric Analysis & Differential Scanning Calorimetry

Thermogravimetric analysis (TGA) was carried out on as-milled samples using a Perkin Elmer STA 6000 analyser. For this analysis, a small amount of sample was weighed out (typically between 10

and 30 mg) into the ceramic/alumina crucible and the sample chamber continuously purged with pure argon gas at 100 ml/min to eliminate oxidants as well as flush away hydrogen that evolves from the sample. The samples were heated from 30 °C to 600 °C at several heating rates between 5 °C/min and 20 °C/min, before cooling down to 30 °C again.

TGA analysis is typically shown as a profile of sample weight against temperature. Because hydrogen is reversibly absorbed onto the Mg composite, it desorbs from the sample at a certain temperature (hydrogen desorbs from pure MgH_2 at approximately 300 °C) and can be traced as weight lost from the sample. This provides a good assessment of hydrogen interaction with the sample.

Differential scanning calorimetry (DSC) was performed simultaneously with TGA in the same apparatus and on the same sample. DSC analysis involved tracking the heat flow into the sample against the temperature of the sample itself. The results from the DSC analysis were used to calculate the activation energy of hydrogen evolution from the sample via the Kissinger method [153]. Hydride decomposition/hydrogen evolution was an endothermic process and the apparent activation energy (E_A) was calculated using the equation:

$$ln\left(\frac{\beta}{T_p^2}\right) = ln\left(\frac{ZR}{E_A}\right) - \frac{E_A}{RT_p} \quad [1]$$

Where β is the heating rate (K/min), T_p is the peak temperature (K), R is the universal gas constant (=8.3143 J/mol K), Z is the pre-exponent (1/min) and E_A is the activation energy (J/mol). From the resulting data and the equation above, a plot of $ln(\frac{\beta}{T_p^2})$ vs $\frac{1}{T_p}$ was used to reveal the value of $\frac{E_A}{R}$ (from the slope).

In this study, the Mg nanocomposite samples produced very wide peaks of up to 300 K, reflecting large hydride decomposition temperatures. It was thus difficult to accurately determine the peak temperature, T_p which consequently affected the Kissinger plots and resulting in unrealistic calculated values of E_A. To overcome this problem, a method was used whereby the decomposition

peak, *Q(T)* was assumed to be the function of several overlapping minor peaks with different parameters:

$$Q(T) = \sum_{i=1}^{n} q_i(T) \quad [2]$$

As such, the DSC spectrum could be deconvoluted and the constituent peaks were modelled by a Gaussian function, as follow:

$$q(T) = Aexp\left[-\frac{(T-T_m)^2}{2w^2}\right] \quad [3]$$

Where A is the peak amplitude and w is the peak width relating to the full width at half maximum (FWHM), which is defined below:

$$FWHM = 2w\sqrt{\ln(4)} \quad [4]$$

Deconvolution of the whole set of DSC spectra was performed assuming that 3 constituent peaks were present or n=3. The peak temperatures for each constituent peak, $T_m^{(i)}$ were fitted into the Kissinger calculations separately for i=1,2 and 3.

For the Kissinger fitting exercise, each experimental point was assigned an error range of $x = \frac{1}{T_m}$ and $y = \ln\left(\frac{\beta}{T_m^2}\right)$. T_m was assumed to be 5 K while the contribution of β in the y value and the y error was estimated as an average and standard deviation of the experimentally observed heating rates in the temperature range from 150°C to T_m. The y error provided weightage to the experimental data during the Kissinger fitting exercise and together with the deviations of experimentally obtained points from a linear fit, allowed more accurate estimation of the error in the calculated E_A value.

Further discussions will be included in chapters reviewing the actual DSC data for the samples in this study.

(TGA and DSC analyses were only performed on earlier samples as the equipment malfunctioned and was not repaired; however, the Sieverts' apparatus was later used with the furnace set at different temperature gradients allowing for Kissinger analysis to still be performed)

3.4.2 X-Ray Diffraction Analysis

X-ray diffraction (XRD) analysis was used to evaluate the composition and crystalline properties of the sample and is an indispensable tool to answer questions such as:

- How much Mg is there in this sample? (related to intensity)
- Is there MgO in the sample? (related to wavelength)
- What impurity phases are there in this sample? (database matching)

It cannot however be used to identify an unknown sample with no prior information [154]. X-rays are electromagnetic beams with atomic sized wavelengths thus allowing it to penetrate any substance. This method is non-destructive and allows for the precise identification of chemical and crystalline composition of solid, powdered samples (due to unique X-ray diffraction patterns of pure substances). The electron density of the material under investigation is the main cause of x-ray beam diffraction, and is recorded as an electron density map. The map is then cross-referenced with a database of known material diffraction patterns. As such, XRD is typically used in conjunction with other phase analysis tools such as TEM or EDS and is rarely used to identify an unknown material.

X-rays are generated by bombarding a metal target (typically Molybdenum or Copper) with high energy electrons that are emitted from a hot filament (eg. Tungsten). This incident beam ionises electrons in the K-shell of the target atom, and the subsequent drop of electrons from the outer orbitals into lower energy positions result in the X-ray beam.

Figure 3.3 below is a sample XRD spectra obtain from reference. The typical XRD spectrum shows the angle of diffraction (2θ) as the x-axis and the intensity as the y-axis. Broader peaks tend to indicate

smaller crystalline structures or significant strain in the microstructure. This is shown in the Scherrer equation [155] used to estimate crystallite sizes:

$$B(2\theta) = \frac{K\lambda}{L\cos\theta} \qquad [5]$$

Where B is the peak width, 2θ is the diffraction angle (typically between 5° to 70°), K is the Scherrer constant (0.62 to 2.08, depending on crystal type/shape), λ is the wavelength of X-ray used and L is the crystallite size. From the equation, it can be seen that the peak width is inversely proportional to the crystallite size. The crystallite size can therefore be estimated by measuring the peak width.

According to T. Ungar in [156], peak broadening is also attributed to structural defects (stacking faults etc) and concentration gradients in non-stoichiometric compounds, or in other words, inhomogeneity of the sample. Furthermore, peak broadening can also be caused by the measuring instrument, as such correct calibration and operating procedures must be practiced. It is further noted that the peak area is independent of crystallite size therefore peak broadening is typically accompanied by a decrease in peak height.

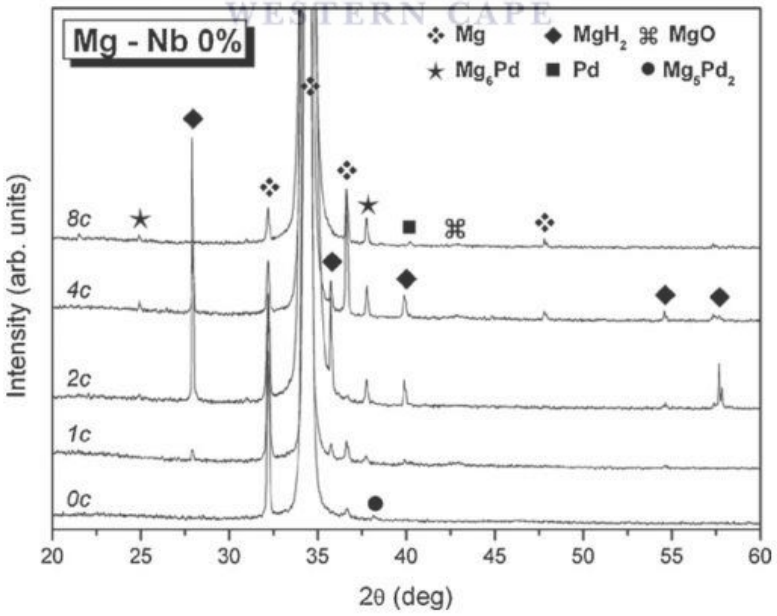

Figure 3.3: XRD spectra showing for different samples of (Oc, 1c, 2c, 4c and 8c) showing the presence and intensities of various elements and compounds (Sourced from [157])

Hydrogen binds with Mg in different progressive phases (α, γ and β); each phase having different binding strength and crystalline properties. XRD analysis at various stages of absorption and desorption shows the different crystal phases present and thus provides crucial information on the how the increase in hydrogen concentration and/or pressure affects the crystal structure of MgH_2.

In this work, the XRD studies were commissioned to iThemba Labs. All analysis was performed using a Bruker AXS D8 Advanced diffractometer with Cu-Kα radiation (λ_1=1.5406 Å, λ_2=1.5444 Å, λ_2/λ_1=0.5). The instrument was water cooled and employed a Bragg angle, 2θ of 15 – 90°. The scan rate and step size used were 1.2°/min and 0.035° respectively. To determine the instrument contribution towards peak profiles, a standard α-Al_2O_3 sample was used as a calibration background profile.

The resulting XRD spectra was analysed via GSAS software using Rietveld full-profile analysis. This yielded lattice periods of constituent phases, abundances crystal sizes and micro-strain data.

3.4.3 Scanning Electron Microscopy & Energy-Dispersive X-Ray Spectroscopy

Scanning electron microscopy (SEM) analysis was performed on samples to evaluate the Mg nanocomposites in terms of surface and internal morphology, topography, and composition. In this study, the SEM equipment used was a Zeiss Auriga Field Emission Gun (FEG) SEM with InLens (working distance 5mm) and secondary electron, SE (10mm) detectors operated at and extra high tension (EHT) voltage of 5kV for high resolution imaging. Once a suitable area in the image was located, the image was frozen and saved; freezing the image is a necessary step when using high magnification as refresh rates were visible moving across the image.

SEM typically offers a large depth of focus, allowing for a larger part of the sample to be viewed at a time. The high resolution imaging enabled the effective examination of formations in close proximity even at high magnifications with little image distortion. The electron beam produced by the equipment interacts with the sample particle and produces secondary or back-scattered electrons that are picked up and recorded by several detectors situated around the sample. The data from these interactions (electron energy, angle of scattering etc.) is then processed and a contrast-based image is produced.

For SEM analysis, samples were placed on sticky carbon discs (pre-refrigerated to maintain crispness of the carbon layer) glued on stubs. The samples were then coated with a gold/palladium layer using a carbon coating machine to enhance conductivity and adhesion to the carbon surface. Proper adhesion was necessary to prevent particle movement under vacuum pressure during analysis. The principle of operation is that gold/palladium plasma is generated in between graphite rods and settles onto the sample which is spun around on an axis. The gold/palladium coating creates a conductive layer which enables SEM analysis. Coating material is typically selected based on the composition of the sample; the coating cannot be of the same material that is already present in the sample. Gold and palladium are used in tandem because palladium prevents gold nanoparticle agglomeration.

In the case of Mg nanocomposites, HR-SEM allowed for the inspection of particle surfaces and grain boundaries that facilitate the diffusion of hydrogen from the surface into the sample. Furthermore, EDS analysis provided compositional analysis of the sample and reaffirmed the content of the sample was free of impurities or oxidation. Higher EHT settings (15-20kV) were used for EDS analysis and the secondary electron viewing method was used to locate the suitable area. Once the desired area was selected, the coating type and spectrum were identified so as not to interfere with the compositional analysis of the sample materials.

3.4.4 High-Resolution Transmission Electron Microscopy (HR-TEM) & Selective Area Diffraction (SAD)

Transmission electron microscopy (TEM) is another method of microscopy that has phase determination capability and provides crystallographic information on the sample. It has similar working principles as the light microscope, utilising an electron beam instead of visible light. Electrons have a much lower wavelength than visible light thus producing image resolutions 1000 times higher than a light microscope and capable of viewing objects in the range of Angstroms (10^{-10} m). The electron beam is produced within a vacuum column and focused using electromagnetic lenses through a thin sample (<100 nm). The interaction of the electron beam and the sample may result in no scattering, single scattering or multiple scattering. Scattering may be elastic or inelastic as well as forward or backward depending on the properties of the sample. The 'unscattered' electrons eventually hit a fluorescent screen below the sample and an image is formed, consisting of bright areas and shadows that correspond to the density of the sample. Scattered X-rays are also detected by an energy-dispersive spectroscopy (EDS) probe that allows for chemical analysis and quantitative analysis.

Transmission electron microscopy was a useful tool to investigate the composition, crystalline and structural properties of the samples after milling and after cycling. Owing that Mg nanoparticles has the tendency to sinter at high temperatures and/or after many sorption cycles, information on the phase changes revealed the current state of crystallinity and average particle sizes. Selective area diffraction (SAD) was used to evaluate the single and polycrystalline phases present in a particular area as well as to identify these crystals by cross-referencing their physical characteristics to the material database as well as the results of the XRD analysis. SAD patterns typically form a series of concentric rings, each corresponding to a set of crystal planes. If the crystallite size is small (100 – 500 nm), then the diffraction rings are broad. Crystallite sizes between 500 nm to 10 µm produce a sharp, smooth and continuous ring pattern while crystallite sizes in excess of 10 µm then to result in only a small portion being irradiated by x-ray thus resulting in a 'spotty' ring [158].

HR-TEM studies were carried out using an FEI Tecnai $G^2$20 field emission gun transmission electron microscope (FEG-TEM) operated at 200 kV. This equipment was also capable of EDS analysis using an EDAX liquid nitrogen cooled lithium doped silicon detector.

For the purpose of elemental mapping, samples on holey carbon grids (prepared for TEM) were examined using techniques called electron energy loss spectroscopy (EELS) and energy filtered transmission electron microscopy (EFTEM); both methods operate on the principle of monitoring electron energy loss after the electron beam collides with the sample. These techniques are capable of identifying and producing distribution maps of elements across the area of focus.

3.5 Pressure-concentration isotherm (PCI) experimental setup

Pressure-concentration isotherms (PCIs) are an invaluable characterisation method for metal hydrides. PCIs should accurately relate the pressure of hydrogen released during desorption (or hydrogen pressure required during absorption) to the concentration of hydrogen absorbed by the metal hydride material.

3.5.1 Methods for measuring and producing PCIs

There are two methods that can be used to produce PCIs of metal hydrides. The gravimetric method measures the changes in material weight as a means to quantify the absorption/desorption of hydrogen from the on material. Due to the intrinsic nature of hydrogen (incomparably lightweight), a highly sensitive micro-balance is required and can only be performed using complicated and expensive equipment. The second method, and the method used in this study, is the volumetric method (Sieverts' method). The Sieverts' method uses a setup that measures pressures and temperatures in a known fixed volume within a closed system. The theoretical storage capacity is obtained using mass balance of the amount of hydrogen in the system. The Sieverts' method is widely preferred due to it simpler, cheaper and user friendly equipment requirements. However, it is burdened by numerous inaccuracies which potentially arise from leaks and diffusion that skew results in a non-linear manner when subjected to varying pressures and temperatures. To minimise

this, a thorough equipment check and calibration is periodically required for the Sieverts'apparatus to ensure the most accurate measurements are obtained during experiments. Conversely, the gravimetric method does not suffer from the same problem as it typically measures absorption and desorption at different pressure points.

PCIs can be obtained using static or dynamic procedures. Static measurements imply step-wise increments of hydrogen pressure or volume whereas dynamic methods use a continuous flow of hydrogen. While the dynamic method is a more realistic reflection of practical refilling and discharge of metal hydride applications, it also tends to produce more hysteresis [159].

3.5.2 The concept of the Sieverts' method

As mentioned previously, the volumetric (Sieverts') method uses a closed system to measure the absorption/desorption of hydrogen in a sample of a known mass. The diagram below (Figure 3.4) is a simplified representation of the Sieverts' apparatus. The reactor is represented on the right side connected via a valve to the reservoir of hydrogen tank on the left.

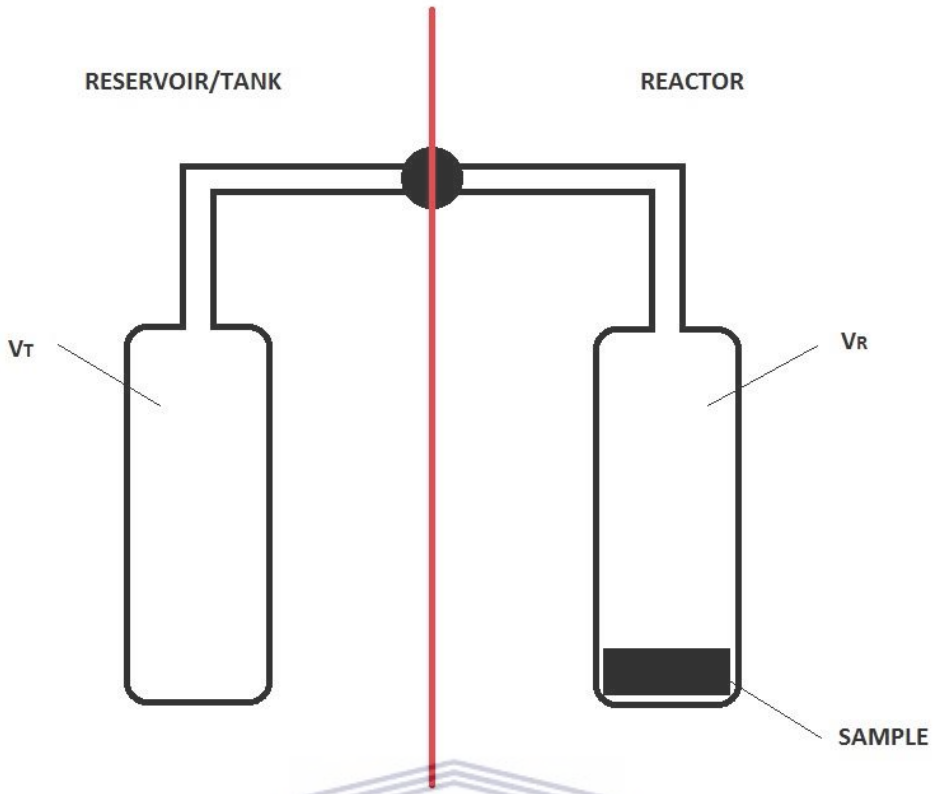

Figure3.4: Simplified representation of the Sieverts' method/apparatus

During absorption, hydrogen flows from the reservoir/tank (V_T) to the reactor (V_R). At the start of absorption it is assumed that there is zero hydrogen content in the sample as well as the reactor volume (in a vacuum state). As such, the total mass of hydrogen in the system at this point is given by the equation:

$$m = m_{T0} + m_{R0}\ ;\ m_{R0} = 0 \qquad [1]$$

T0 and R0 represent the system before the valve is opened and T1, R1 is after the valve is opened. When the valve is opened, hydrogen flows into the reactor. Note that absorption only occurs is hydrogen pressure is greater than the equilibrium pressure. Therefore the equation above becomes:

$$m = m_{T1} + m_{R1} + m_s \qquad [2]$$

Where m_s is the mass of hydrogen absorbed in the sample. At this point, the amount of hydrogen absorbed by the material can also be calculated due to nature of the closed system (fixed amount of hydrogen):

$$m_s = (m_{T0} + m_{R0}) - (m_{T1} + m_{R1}) \quad [3]$$

And because m_{R0} is known to be 0, the equation can be simplified as follows:

$$m_s = m_{T0} - (m_{T1} + m_{R1}) \quad [4]$$

The constitutive equation for hydrogen is used to calculate the amount of hydrogen in the reservoir and reactor volumes. It is given as:

$$pV = Z(p,T) \cdot m_{H_2} \cdot R_{H_2} \cdot T \quad [5]$$

Where the real gas factor Z(p,T) ≈ for p < 0.1 MPa.

3.5.3 Specific Sieverts' apparatus

The specific setup used in this study is illustrated in Figure 3.5 below.

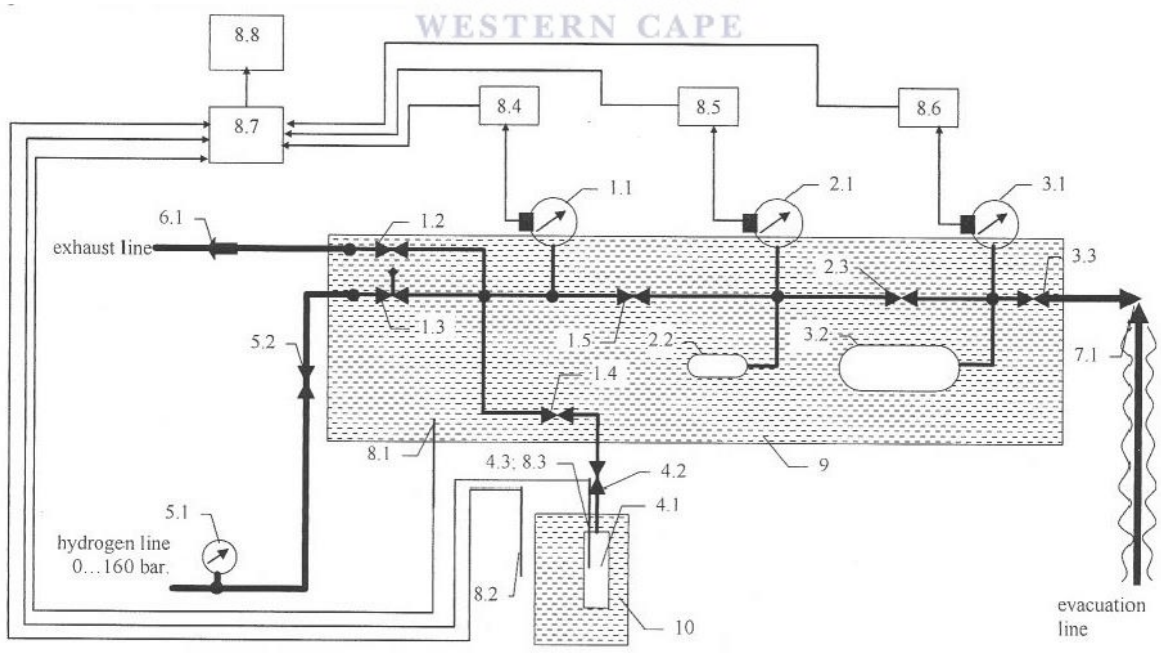

Figure 3.5: Schematic of Sieverts' apparatus used in this study [160]

Parts labelled 1.1, 2.1 and 3.1 are three separate pressure sensors associated with individual buffer volumes. Component 1.1 represents the 160 bar pressure sensor with corresponding buffer volume of approximately 5 cm^3, component 2.1 is the 16 bar sensor with 75 cm^3 volume (2.2) and component 3.1 is the 1 bar sensor with 150 cm^3 buffer volume (3.3). These are connected from the highest to lowest pressure in series coming from the reactor (4.1) and heading towards the vacuum line (7.1). Peripheral and other components will be noted and described in Appendix 2.

The reactor (4.1) is stainless steel constructed and typically heated within an external furnace with a controller box. The reactor housed the sample and its structure was of utmost importance. The walls of the reactor had the requirement of being thin enough to minimise the temperature gradient from the outside (furnace) to the inside (sample) of the reactor. The reactor needed also a sufficiently narrow capillary to ensure that sample thickness was at a minimum to ensure that the sample was heated evenly as well as maintaining effective thermal conductivity of the sample. The amount of sample loaded into the reactor was also decided with considerations towards minimising pressure drop while allowing effective diffusion of hydrogen through the contact surface into the bulk.

3.5.4 Thermal Desorption Studies (TDS) and re-hydrogenation

Using a Sieverts' apparatus, as-milled samples were repeatedly desorbed and absorbed with hydrogen to assess the performance of the material in terms of hydrogen release and uptake. The sample powder weighing approximately 200-400 mg was loaded into the reactor within the confines of an argon glove box. The entire reactor and Sieverts' apparatus was then evacuated at room temperature to $<10^{-4}$ mbar vacuum pressure. TDS measurements were carried out by heating the sample from room temperature to 450 – 470 °C under dynamic vacuum at a rate of 5 °C/min. When hydrogen desorption occurs, the vacuum pressure is affected and is thus translated into meaningful desorption data. The TDS procedure was halted once the vacuum pressure returned to its original plateau i.e. hydrogen desorption was complete.

For the re-hydrogenation of samples, the reactor (still connected to the Sieverts' apparatus after TDS) was cooled down to ca. 250 °C with an initial hydrogen pressure of 12 – 15 bar. The final pressure after absorption using the abovementioned amount of sample is typically 6 – 8 bar. Hydrogen absorption data during re-hydrogenation was processed using the Avrami-Erofeev equation to interpret kinetics:

$$C = C_{max}\left\{1 - exp\left[-\left(\frac{t}{t_0}\right)^n\right]\right\} \quad [6]$$

Where C is the actual hydrogen absorption, C_{max} is the maximum hydrogen absorption, t is time, t_0 is the characteristic hydrogenation time or reciprocal rate constant and n is an exponential factor indirectly related to the reaction mechanism.

3.5.5 Calibration of Sieverts' apparatus

Due to the numerous inaccuracies that may arise from the volumetric analysis method, the Sieverts' apparatus required calibration in order to ensure accurate measurement of hydrogen desorption and absorption during analysis. This was performed by using material with no hydrogen absorption properties i.e. iron ore. The system was then evacuated at the typical desorption working temperature, ca. 450 °C. Following this, hydrogen was introduced at incremental pressures (50, 60 and 75 bar), allowing for a plateau in between each increase.

The above procedure was then repeated, but with increasing weights of iron powder (8, 16, 24 g), including the approximate weight of sample to be used (ca. 500 mg). This allowed for accurate calibration and quantification of the buffer volumes and reactor volume along with the intermediary capillary volumes.

The vacuum sensor for the apparatus was calibrated using a known flow rate of H2 gas into the system.

3.5.6 Cyclic stability Experimental Setup

The cyclic stability of hydrogen storage materials is of great practical importance. Hydrogen storage materials must be capable of a substantial amount of absorption and desorption cycles to be commercially competitive. The ultimate commercial target for hydrogen storage systems for on-board hydrogen storage for light-duty fuel cell vehicles is 1500 cycles [23].

Although the materials prepared and investigated in this study were not yet at the commercialisation stage, limited cyclic studies were still conducted on selected samples in order to gauge the stability of the material up to 50 cycles (also due to time and usage constraints of the equipment). The equipment used for cyclic studies is the PCT-Pro-2000 automated gas sorption analyser (Hy-Energy Scientific Instruments). This setup allowed for automated pressure switching and dosing that could be programmed at the start of the test.

Cyclic studies may be performed using the isothermal (constant temperature) or isobaric (constant pressure) method. For this study, the isothermal method was chosen. The specific steps are detailed in the following section.

3.5.6.1 Cyclic stability Experimental method

Approximately 500 mg of sample was placed in the reactor (in a glovebox). Sample temperature was controlled using a furnace and external controller. Samples were cycled between absorption and desorption states at 350 °C for 30 minutes each. The final pressure for absorption was estimated to be ca. 15 bar and desorption final pressure ca. 3 bar. It was noted that the temperature of the sample, T_s increased drastically in the first 10 seconds of hydrogenation during cycling. A similar trend was observed in previous studies with HRBM of Mg-V [91]. Therefore the time dependence of the sample temperature was estimated as follows:

$$T_s^*(t) = T_s \exp\left(-\frac{t}{\tau}\right) \int_0^t \exp\left(\frac{u}{t}\right) \frac{d}{du}[T_s(u)]\, du \qquad [7]$$

Where $T_S^*(t)$ is the actual time dependence of sample temperature and τ is the thermocouple response time (measured separately as 5.6 ± 0.1 s).

The calculated values of T_S^* were then compared with temperatures of the Mg ↔ MgH_2 transformation, denoted as T_{eq}, which in turn was defined from the Van't Hoff equation with respect to temperature:

$$T_{eq} = \frac{\Delta H}{R \ln(P) + \Delta S} \qquad [8]$$

In equation [8], P is the actual hydrogen pressure while reference data for transformation enthalpy, ΔH = -74.5 kJ/mol H_2 and entropy, ΔS = -135 J/mol H_2 K.

Using the same setup, kinetic studies could also be performed by performing limited absorption/desorption cycles at different temperatures.

4.0 Investigation of hydrogen storage properties of Mg – $TiFeO_3$ nanocomposites

As continuation of a previous study [26], [152], ilmenite ($FeTiO_3$) was used as a catalytic additive to MgH2 in order to improve hydrogen sorption kinetics. Ilmenite was selected on the basis of being cheaper as compared to the individual Ti, Fe metals or their corresponding alloys.

4.1 Ball milling hydrogenation of Mg – *x* wt. % $FeTiO_3$

The addition of 2 wt. % $FeTiO_3$ was sufficient to reduce the milling time to hydrogen saturation. While pure Mg required HRBM durations of about 5 hours, the samples Mg – *x* wt. % $FeTiO_3$ (where x = 2, 5, 10, 15, 20) were completely hydrogenated within 1-2 hours. Generally, the two parameters from Equation (6) that influence kinetic improvements are the characteristic reaction time, t_0, and the Avrami exponent, *n*. Both are changed significantly by the introduction of $FeTiO_3$ and other useful additives and are responsible for the shortening of the duration required for complete transformation of Mg to MgH_2 during HRBM. The corresponding hydrogen absorption curves are shown in Figure 4.1 and the hydrogenation rates are observed to increase with increasing $FeTiO_3$ composition. At $FeTiO_3$ concentrations above 5 wt. %, up to 6.7 wt. % hydrogen was absorbed during 1 hour of ball milling.

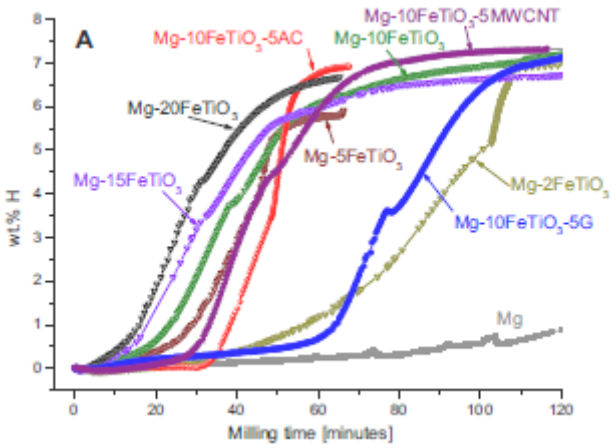

Figure 4.1: Hydrogen absorption during HRBM of Mg – x wt. % FeTiO3 (x = 2 – 20) [26]

When carbon additives (graphite, activated carbon and multi-walled carbon nanotubes) are used alongside $FeTiO_3$, milling duration becomes characteristically longer as exemplified by Mg – 10$FeTiO_3$ – 5G where the presence of an incubation period of about 1 hour is observed before hydrogenation occurs. Nevertheless, complete hydrogenation (ca. 7 wt. %) is achieved within 2 hours. The samples with other carbon additives (AC and MWCNT) absorbed about 7 wt. % hydrogen within 1 hour of HRBM.

4.2 XRD and elemental composition

The diffraction patterns obtained from the as-milled Mg – 10$FeTiO_3$ showed broad peaks characteristic of ball milling. This is due to the formation of nanocrystallites and the increase in defects during HRBM [161].

Upon hydrogenation, the Mg – $FeTiO_3$ nanocrystallites grow slightly larger as indicated by the sharp, intense diffraction peaks. The presence if α-MgH_2, Mg was observed, along with trace amounts of MgO and Fe. It was noted that the decrease in $FeTiO_3$ content results in a corresponding increase in α–MgH_2 crystalline size [26].

EDS studies performed provided elemental compositions for various spectrums taken on different areas of the sample, as shown in Figure 4.2.

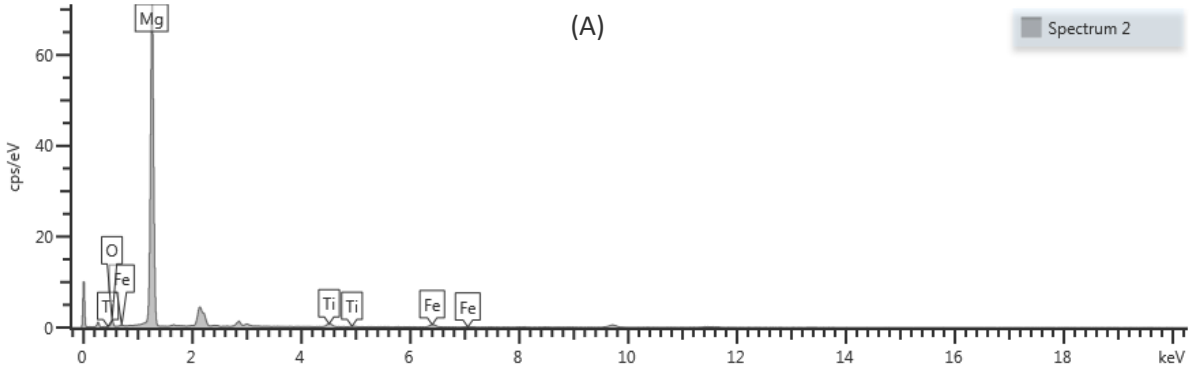

(B)

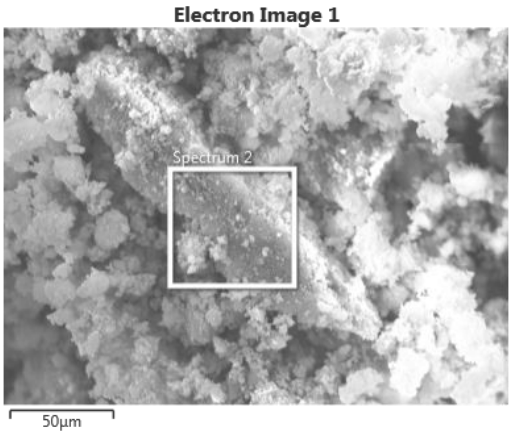

Figure 4.2: EDS spectrum (A) taken from the Mg – 10FeTiO3 sample at the area denoted (B)

From Figure 4.2 (A), it can be seen that Mg was present in the highest concentration followed by other elements including Fe, Ti and O. Several spectrums were obtained for different as-milled samples. The elemental composition data is summarised in Table 4.1.

Element	Average compositions (mass %)		
	Mg – 10FeTiO$_3$	**Mg – 10FeTiO$_3$ – 5AC**	**Mg – 10FeTiO$_3$ – 5G**
Mg	52.2	41.6	40.7
O	44.7	49.7	50.9
C	-	6.4	6.8
Ti	1.2	0.9	0.7
Fe	1.9	1.4	0.9

Table 4.1: Average compositions of elements as calculated by EDS

The three samples shown in Table 4.1 show compositions which are in good correspondence to the stoichiometric calculations as well as the XRD data. In the Mg – 10FeTiO$_3$ sample, a very small amount of carbon was detected but eliminated on the basis of being trace elements occurring naturally.

4.3 SEM studies

Additionally, SEM images were obtained for the as-milled samples of Mg – $FeTiO_3$ and those with carbon additives. The sample without carbon showed finer particles (FeTi based) strewn across the larger matrix of Mg/MgH_2. The FeTi based particles measure in the order of ≤ 100 nm in a wide range of different sizes and are quite well dispersed across the sample, as shown in Figure 4.3.

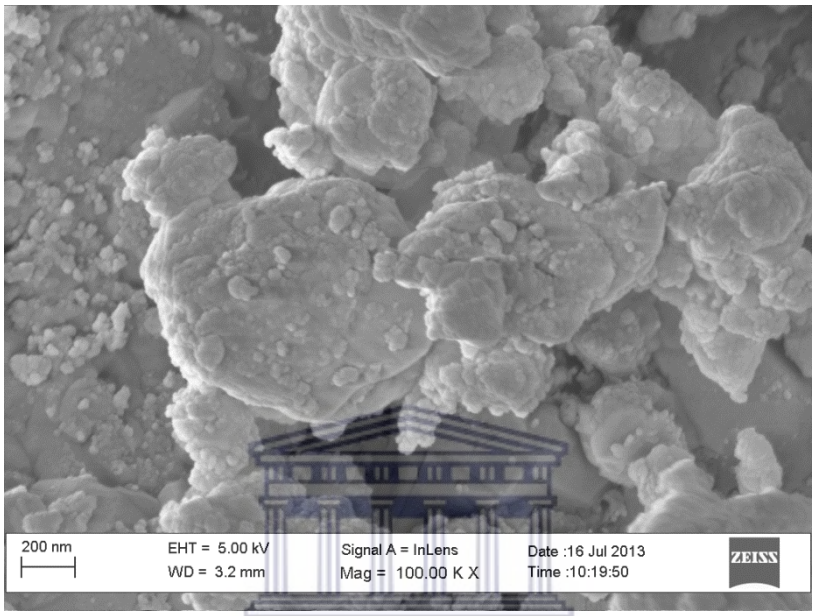

Figure 4.3: SEM image of Mg – FeTiO3

Meanwhile, the Mg – $FeTiO_3$ – 5C samples present a different morphology. Figure 4.4 shows wide angle and more magnified images taken from Mg – $FeTiO_3$ – 5AC and Mg – $10FeTiO_3$ – 5G. Generally, smaller particles of FeTi based material are observed on the surface of the Mg bulk material. These particles appear to be in the same order of size as found on the sample without carbon but higher in quantity. The Mg/MgH_2 matrix itself has a rougher texture and appears to be more irregularly shaped than in the Mg – $FeTiO_3$ sample.

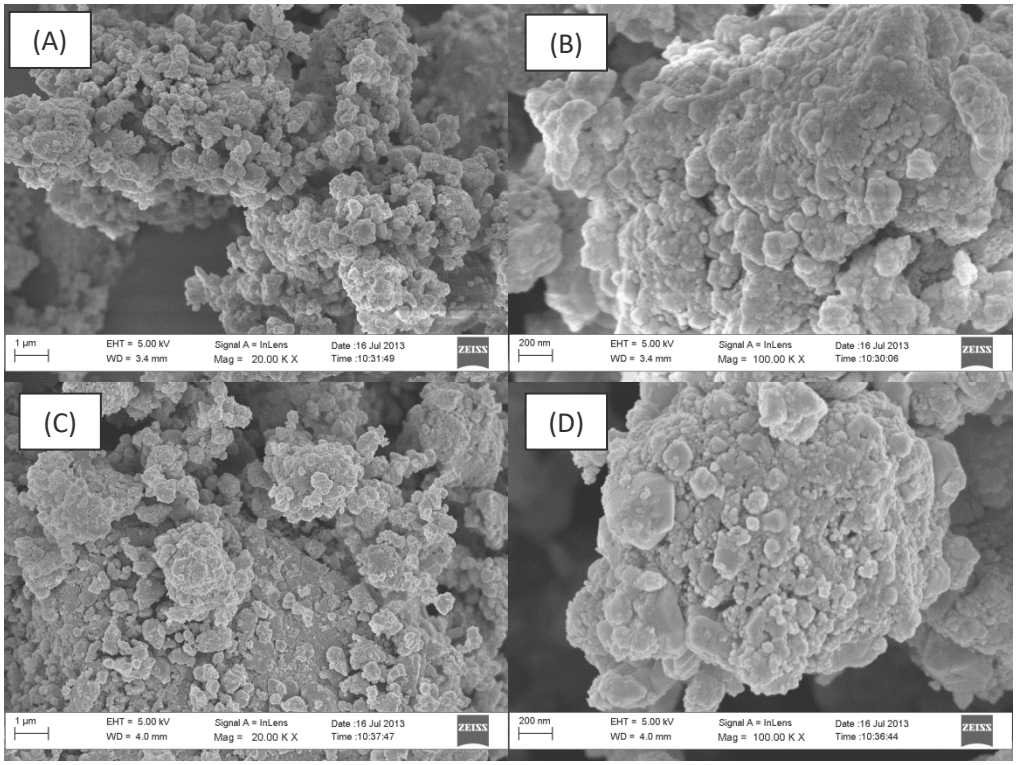

Figure 4.4: SEM images of Mg – 10FeTiO3 – 5AC (A and B), and Mg – 10FeTiO3 – 5G (C and D)

In Figure 4.4 (C and D), the sample containing 5 wt. % graphite appears to have the most refined particles at ≤ 100 nm in size. These are also very well dispersed and appear to form small clusters over smaller particles, as seen in Figure 4.4 (C). It was hypothesised previously [116] that carbon did not have a catalytic role in Mg based systems. In the previous work performed by Lototskyy et al. [152], it was shown that the addition of carbon actually slowed down hydrogen absorption/desorption but improved the cyclic stability of the material. This suggests that carbon plays an intermediary role that maintains the accessibility of grain defects for H atom diffusion into the Mg/MgH_2 bulk material.

4.4 Summary of Mg – $FeTiO_3$ study

The selection of ilmenite ($FeTiO_3$) as an additive to Mg was made on the basis of being a cheaper source of 'impure' Fe and Ti material that would have a beneficial catalytic effect on hydrogen absorption/desorption performance. It was demonstrated clearly that Mg – $FeTiO_3$ nanocomposites

do indeed have better hydrogen absorption rates during HRBM as well as improved kinetics during desorption and re-hydrogenation (for the second time). However, the cyclic stability of the material was dubious as it was noted by Sibanyoni [26] that the morphology of the material was drastically altered during high temperature cycling of absorption/desorption. This is chalked down to the formation of MgO from the reduction of $FeTiO_3$; MgO proceeds to coat the unreacted surface of Mg thus impeding hydrogen atom passage.

In this study, it was shown using EDS that the Mg – $FeTiO_3$ nanocomposite composition was a match to the stoichiometric calculations of the material. SEM studies noted the different morphologies of the material with and without carbon and provided a theory as to why Mg – 10$FeTiO_3$ – 5G has superior reversible hydrogen storage capacity over the nanocomposite without carbon. Based on the evidence from SEM analysis, the graphite material upon being sheared during HRBM (and hence causing the incubation period without hydrogen uptake), appears to provide extremely good coverage over the Mg surface that could afford some protection against MgO thus enhancing reversible hydrogen storage capacity.

5.0 Investigation of hydrogen storage properties of Mg - FeV nanocomposites

Commercially available vanadium is an example of intermetallic metals that may be used to accelerate the hydrogenation of Mg. The catalytic effect of vanadium improves hydrogen absorption and desorption kinetics even at room temperatures, when prepared by HRBM. This performance improvement has been attributed to the significant decrease in particle size during HRBM; in turn the diffusion length of hydrogen within the material is shortened [91].

Ferro vanadium, on the other hand is an alloy typically used in metallurgy. According to Westbrook Resources Ltd., the largest practical application for ferro vanadium (with V content at 35-85 %) is in the process of hardening steel to manufacture parts such as gears, axles and other frames that require significant strength [162].

The ferrovanadium (>75% V grade) used in this study was supplied by Insimbi Alloy Suppliers (Pty), Ltd.; South Africa. The measured composition was recorded as $Fe_{0.1857}V_{0.8143}$. Further specifications have already been detailed in the Chapter 3.

5.1 Ball milling hydrogenation of Mg - *x* wt. % FeV

As mentioned in the Experimental chapter, the Mg – x wt. % FeV samples were prepared via ball milling. Several compositions of FeV were used i.e. 2, 5, 10 and 20 wt. % including three samples with activated carbon, multi-walled carbon nanotubes and graphite (which will be covered in the next chapter).

Hydrogenation curves for ball milling of Mg – *x* wt. % FeV are shown in Figure 5.1. Overall, the hydrogenation data shows that Mg - FeV nanocomposites produced via HRBM have superior hydrogenation performance over pure Mg. The observed improvements gradually become more pronounced up to Mg – 10 wt. % FeV and then slightly deteriorate, as seen in the Mg – 20 wt. % FeV. Correspondingly, the increase of FeV content in the nanocomposite also results in a decrease in

hydrogen absorption capacity, due to the lower hydrogen content in hydrogenated vanadium as compared to MgH_2. A notable example would be the Mg – 68 wt. % FeV which exhibited the fastest absorption kinetics but also the lowest hydrogen storage capacity among all the prepared Mg – *x* wt. % FeV samples.

The Mg – 2 wt. % FeV sample showed the highest hydrogen storage capacity, albeit being the slowest to achieve its maximum hydrogenation rate. All other samples achieved their maximum hydrogen absorption rate and maximum hydrogen storage capacity within 90 minutes and 120 minutes respectively. This can be attributed to the crushing effect of V (Mohrs hardness 7.0) on the relatively soft Mg (Mohrs hardness 2.5) that produced smaller particles that aided in minimising hydrogen diffusion lengths.

Drawing parallels to the Avrami-Erofeev equation, the parameter directly affecting kinetic improvements is characteristic reaction time, t_0, or its inverse (AKA rate constant), $k = \frac{1}{t_0}$, as well as the Avrami exponent, n, which is indirectly associated with the reaction mechanism. Both parameters are significantly altered with the introduction of additives such as FeV and carbon (and indeed FeTiO3, Ti and graphite as shown in other chapters of this thesis). The primary effect that resulted from the addition of FeV was the obvious shortening of the time required to completely transform Mg to MgH_2 via HRBM.

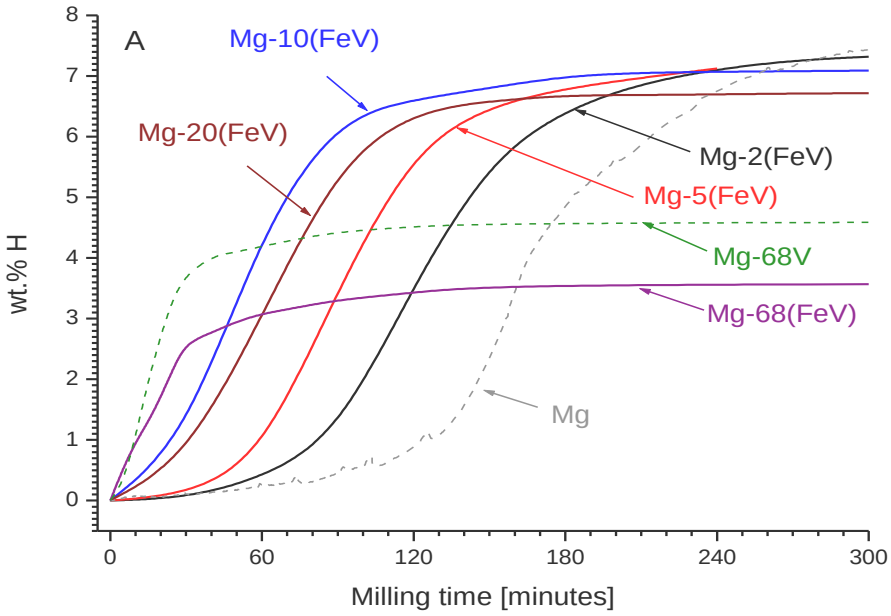

Figure 5.1: Ball milling hydrogenation profiles for Mg - FeV alloys

The highest hydrogen storage capacity was achieved by the Mg – 2 wt. % FeV, scoring 96.4% of the theoretical maximum capacity. Correspondingly, the Mg – 20 wt. % FeV showed a maximum capacity of 95.3% of the theoretical value. All samples of Mg – *x* wt. % FeV showed close to complete hydrogenation (H/M≥1.9). Table 5.1 summarises the compositions of samples studied and their HRBM hydrogenation performance and outcomes. The Mg, Mg – 68 wt. % V and Mg – 68 wt. % FeV samples are included for reference. In the latter two samples, the maximum absorbed hydrogen during HRBM was 90.5% and 70.6% of their respective theoretical values.

Samples	Ball to Powder Ratio (BPR)	Additive used		Theoretical wt. % H (1)	Max H sorption during HRBM	
		V or $V_{0.81}Fe_{0.19}$ (FeV)				
		mol.%	wt. %		wt. % H	H/M
Mg	40	–	–	7.66	7.45	1.95
Mg-2(FeV)	39.2	0.89	1.96	7.59	7.32	1.92
Mg-5(FeV)	38.1	2.21	4.76	7.48	7.12	1.90
Mg-10(FeV)	36.4	4.32	9.09	7.32	7.07	1.93
Mg-20(FeV)	33.3	8.27	16.67	7.03	6.70	1.90
Mg-68(FeV)	40	50	68.1	5.03	3.55	1.42

Mg-68V	40	50	67.9	5.07	4.59	1.83

Table 5.1: Compositional analysis of samples after HRBM

Note: [(1)] – Assuming H/M=2

5.1.1 Sample activation

Hydrogen storage materials containing Mg typically require an activation step which entails exposure to high temperatures (>300C) and high pressures of hydrogen (≥ 1MPa depending on composition) alternately for several cycles. This step was taken to ensure that the passivated MgO layer that generally forms on the Mg surface can be removed and discarded.

However, samples prepared via HRBM required non-such activation, as demonstrated in Figure 5.1 where the samples began to absorb hydrogen right from the start of the milling process. It is widely agreed upon that this is because HRBM removes contaminants and oxides from the surfaces of Mg mechanically while generating fresh surfaces [84], [146], [163]. Although some samples in this study still exhibit slower hydrogen absorption profiles, HRBM for a duration of 5 hours was more than sufficient to achieve maximum absorption capacities.

5.2 DSC

The DSC spectra for the samples in this study were characterised by steep ascending fronts followed by a mildly sloping descent, and wide peaks of hydride decomposition. While a typical 'good' DSC spectrum exhibits the opposite properties in both cases, the emergence of these features did not hinder the calculation of activation energies besides providing insight on the nature of the composites. Figure 5.2 shows DSC spectrums for various samples, obtained with a heating rate of 10 K/min. The non-conventional peaks have been de-convoluted into separate peaks relating to sample composition (dotted lines).

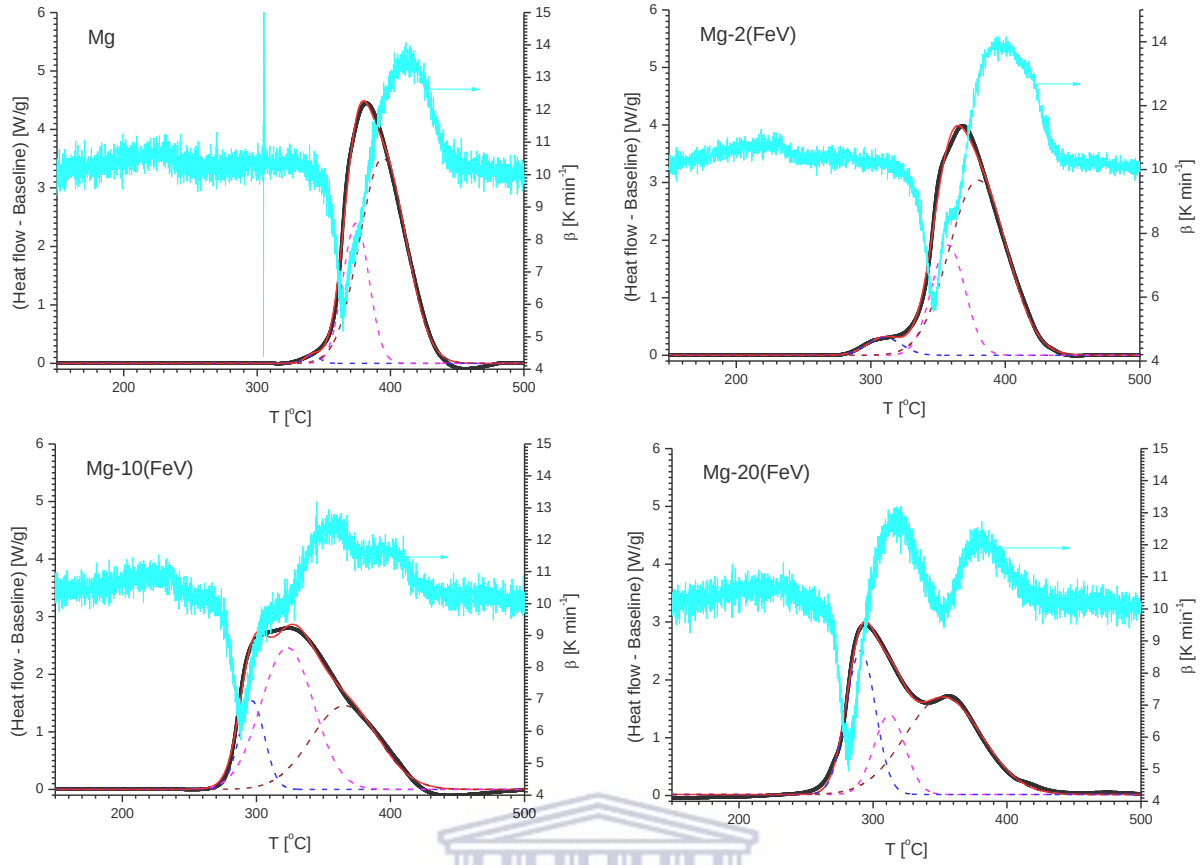

Figure 5.2: DSC spectrums for as-milled Mg – x wt. % FeV samples (x = 0, 2, 10, 20); experimental data shown as points, calculated curves are solid lines, constituent peaks are shown as dashed lines and observed values of β = dT/dt correspond to the y-axis on the right

As shown in Figure 5.2, the DSC spectra have a wide temperature range for hydride decomposition. For Mg, the peak full width (FW) is approximately 100 K and the addition of FeV results in further widening of the FW value up to 170 - 180 K. It is also noted that the presence of FeV also causes the appearance of non-resolved peaks, which in turn complicates the calculation of hydrogen decomposition energies using the Kissinger method. The method used to address this problem has been described in the *Experimental Methods* chapter under the DSC section and as seen in Figure 5.2, the deconvolution of the DSC spectra provides good correspondence to the experimental data with R^2>0.99. The deconvolution produced three peaks that correspond to the distinct decomposition of less stable V-based hydride, decomposition of γ-MgH_2 and the decomposition of α-

MgH_2 respectively. One issue that remains is that the constituent peaks (dashed lines in Figure 5.2) do not sufficiently match the shape of the peaks, although the maximum temperature values are not significantly altered. Kissinger plots for this material are included in Appendix 3.

In summary, the introduction of FeV to Mg results in a few changes as shown by DSC. They are as follows:

- Decrease of 50 – 100 K in the decomposition onset temperature; the decrease becomes greater with higher FeV content
- Decrease of 10 – 120 K in the peak decomposition temperature, corresponding to the maximum decomposition rate; the decrease becomes greater with high FeV content, particularly from 10 wt. % FeV upwards
- Significant widening of decomposition temperature range (FW) with increasing FeV content
- Greater contribution of the lower temperature de-convoluted peak to the overall decomposition range with increasing FeV content ($x \geq 10$); the higher temperature peak exhibits the opposite tendency at $x \leq 10$

5.3 TDS and re-hydrogenation

TDS and DSC spectra are essentially similar in that they reflect changes to the sample with increasing temperature (Figure 5.3). A comparison between the two shows that the TDS spectrum produces lower onset desorption temperatures and correspondingly wider decomposition temperature ranges. There was less distortion in the TDS curves as compared to the DSC ones, although the increase in FeV content resulted in a similar decrease in the gradient on the descending portion of the spectrum as well as the appearance of an additional high-temperature peak.

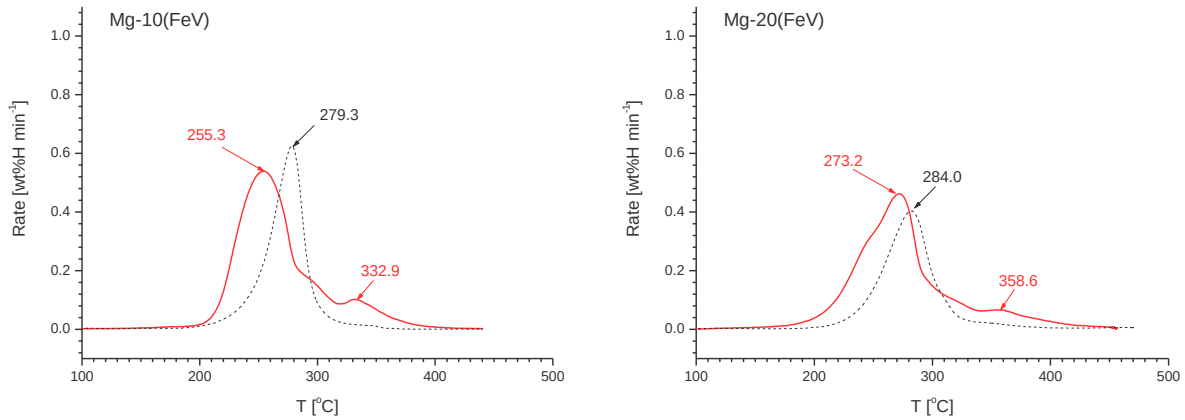

Figure 5.3: TDS curves for the as-milled (red) and re-hydrogenated (black) samples; peak temperature is labelled

The differences between the TDS and DSC curves occur as a result of the different conditions under which the tests were performed (compare Figure 5.2 and 5.3). In the case of the TDS analysis, there was zero chance for contamination during sample loading as the reactor was loaded and sealed within the Argon glovebox. On the other hand, there is a brief and unavoidable moment of exposure when samples are loaded into the TGA equipment. Furthermore, the vacuum conditions in the Sieverts facilitate the complete and effective removal of adsorbed impurities in the sample. These factors contribute towards less steep ascending fronts and the absence of additional peaks on the descending side during TDS.

From Figure 5.3, it is also noteworthy that the second TDS (black line; performed after one cycle of re-hydrogenation) exhibits clear one-stage decomposition with one peak of hydrogen desorption corresponding to the decomposition of α-MgH_2. The peak temperature for the second TDS was also higher than the as-milled samples. This can be attributed to the additional presence of γ-modified MgH_2 in the as-milled samples, which distorts the overall thermal decomposition process [164].

5.4 XRD

XRD studies were carried out without complications despite the samples being exposed to air and moisture during analysis. A summary of XRD data obtained is presented in Table 5.2.

Sample	Characteristics of the constituent phases*						
	α-MgH_2	γ-MgH_2	Mg	BCT-H	FCC-H	BCC-H	BCC
Mg	81.0(–) / 14 *a*=4.5177(4) *c*=3.0188(4)	19.0(3) / 16 *a*=4.513(2) *b*=5.457(3) *c*=4.937(3)	–	–	–	–	–
Mg-2(FeV)	72.9(–) / 10 *a*=4.5133(7) *c*=3.0284(7)	22.8(3) / 19 *a*=4.508(4) *b*=5.439(5) *c*=4.988(5)	–	1.8(1) / 11 *a*=2.965(3) *c*=3.610(4)	–	2.5(9) / 12 *a*=3.040(3)	–
Mg-10(FeV)	72.5(–) / 13 *a*=4.5169(5) *c*=3.0213(5)	22.8(3) / 19 *a*=4.545(5) *b*=5.407(6) *c*=4.956(6)	–	1.6(1) / 11 *a*=2.757(3) *c*=4.029(9)	–	13.7(1) / 5 *a*=3.012(1)	–
Mg-10(FeV) – after TDS	–	–	75.7(–) / 76 *a*=3.21090(7) *c*=5.2136(2)	–	–	–	24.3(3) / 7 *a*=2.984(1)
Mg-10(FeV) – re-hydrogenated	76.6(–) / 107 *a*=4.52126(6) *c*=3.02389(7)	–	9.3(1) / 80 *a*=3.2151(2) *c*=5.2202(7)	–	–	14.1(2) / 5 *a*=3.001(1)	–
Mg-10(FeV) – cycled 10 times at *T*=350°C	79.3(–) / 110 *a*=4.52120(6) *c*=3.02386(7)	–	8.9(1) / 93 *a*=3.2148(2) *c*=5.2203(6)	–	–	8.9(1) / 6 *a*=2.999(1)	–
Mg-20(FeV)	61.4(–) / 11 *a*=4.5228(4) *c*=3.0266(4)	20.0(3) / 5 *a*=4.489(7) *b*=5.753(9) *c*=4.976(9)	–	6.0(1) / 9 *a*=2.944(2) *c*=3.255(4)	6.2(1) / 10 *a*=3.959(2)	6.3(1) / 7 *a*=3.009(1)	–
Mg-68(FeV)	20.9(3) / 8 *a*=4.501(-) *c*=3.02(-)	11.7(4) / 5 *a*=4.521(-) *b*=5.438(-) *c*=4.934(-)	0.8(-) / 540** *a*=3.210(-) *c*=5.204(-)	16.9(-) / 16 *a*=2.8633(9) *c*=3.655(2)	18.2(2) / 13 *a*=3.9746(8)	8.8(1) / 15 *a*=3.0861(7)	22.7(2) / 7 *a*=2.978(1)
Mg-68V	8.2(2) / 9 *a*=4.478(3) *c*=3.026(4)	0.9(2) / 22 *a*=4.49(-) *b*=5.40(-) *c*=4.90(-) (-)	0.5(5) / >1000 *a*=3.197(1) *c*=5.190(1)	38.1(2) / 48 *a*=6.0277(4) *c*=6.8248(8)	52.3(-) / 48 *a*=4.2540(3)	–	–

Table 5.2: Summary of XRD data for the Mg – FeV samples (as-milled unless otherwise indicated)

Note:

*Calculated abundance [wt. %] /Crytallite size [nm]; lattice periods [Å]

**Preferred orientation plane (001)

Reference data: Refer to Appendix 4

As seen in Table 5.2 and in Figure 5.4, the as-milled samples exhibited the presence of both α- and γ – modified MgH_2 at the nanoscale, with lattice periods in good correspondence to reference data [165]. Several other phases were noted in the XRD patterns; these were identified as hydrogenated V and FeV, becoming especially prominent in the samples with 68 wt. % FeV and V.

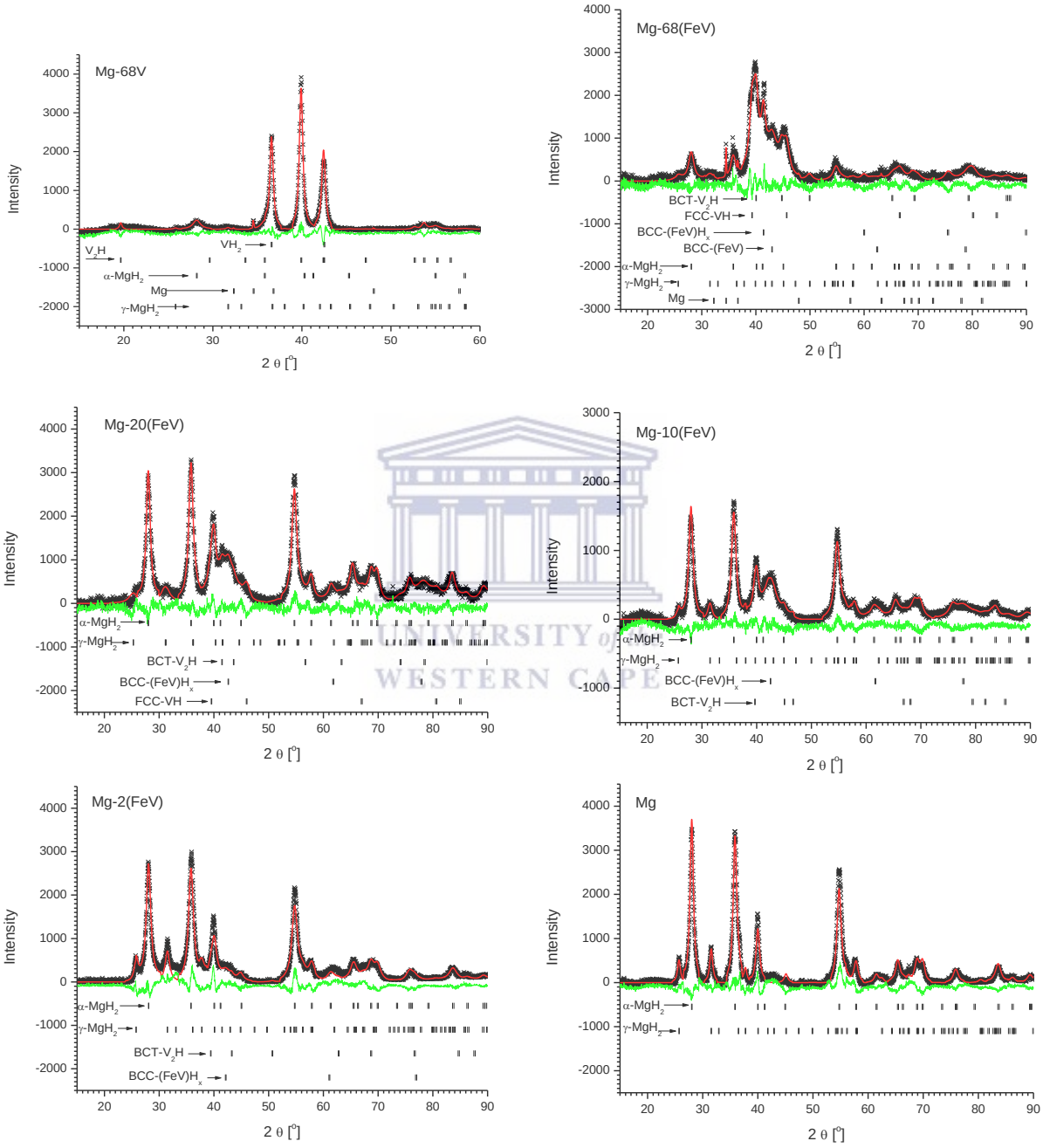

Figure 5.4: XRD spectra for the as-milled samples of Mg – 68 wt. % V, Mg – FeV and Mg

It is immediately apparent that the substitution of V with FeV causes major changes to the phase composition of the Mg nanocomposite (top two images in Figure 5.4). In the Mg – 68 wt. % V sample, well-resolved peaks corresponding to vanadium monohydride (V_2H_{1+x}) and vanadium dihydride (VH_2) were noted and these were also a good match to reference data with crystallite size ca. 45 nm [165]. On the other hand, the Mg – 68 wt. % FeV sample exhibits a much more diverse pattern. The phases found were a close match to hydride phases BCT – $(V,Fe)_2H$ and FCC – (V,Fe)H with nanocrystalline size of about 15 nm [166]. Besides that, significant amounts of non-hydrogenated BCC phase (crystallite size about 7 nm) was noted with the lattice period matching the major BCC phase in the starting FeV material. Finally, another BCC phase was matched in the XRD spectra for Mg – 68 wt. % FeV with 3.6% higher lattice period corresponding to a solid solution of hydrogen in the parent BCC. Crystalline sizes for this phase were estimated to be 15 nm.

Figure 5.4 also showed that samples with lower FeV content produced high intensities and narrower MgH_2 peaks. This corresponded well to the increase of crystallite size from 5 – 8 nm (Mg – 68 wt. % FeV) to 14 – 16 nm (as-milled pure Mg). The total calculated abundances for the FeV phases (BCC, FCC and BCT) only corresponded adequately to the content of FeV in the samples for Mg – 20 wt. % FeV. The discrepancy for samples with lower FeV content can be attributed to the low accuracy of quantitative phase analysis using XRD which is further complicated by the wide peaks of these phases covering the range of crystallite sizes from < 5 – 12 nm, as seen in Table 5. … These samples were noticeably missing the FCC – (V,Fe)H phase.

5.5 Cyclic studies

Cyclic hydrogen desorption and absorption was carried out up to 50 cycles on all as-milled samples at 350 °C and approximately 30 minutes for each phase. As shown in Figure 5.5, Mg – 10 wt. % FeV sample showed good cyclic stability for up to 30 hydrogen desorption/absorption cycles; the average final absorption and desorption capacities were 4.93 ± 0.02 wt. % H and 4.82 ± 0.02 wt. % H respectively. This shows that the Mg – FeV nanocomposites have better cyclic stability than as-milled

pure Mg where maximum hydrogen concentration dropped from 7.3 to 6.9 wt. % within the first 10 absorption/desorption cycles under the same conditions [116].

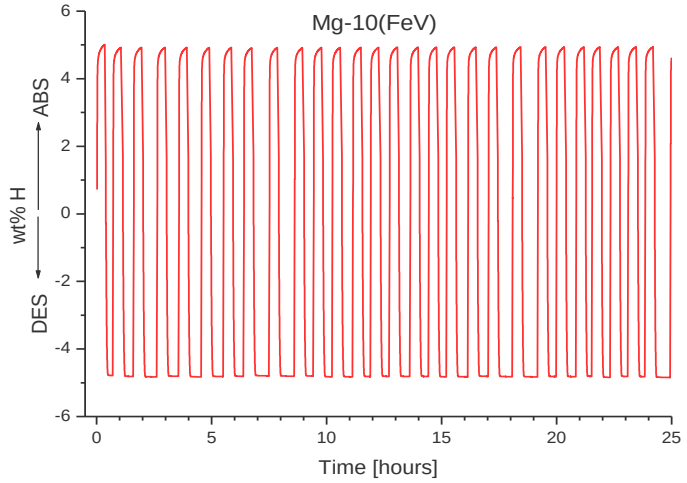

Figure 5.5: Collected data from cyclic studies for Mg – 10 FeV; absorption starting pressure (ABS, P ≥ 14 bar), desorption starting pressure (DES, P ≤ 3 bar), T = 350 °C

A significant decrease in C_{max} is also observed during re-hydrogenation when compared against HRBM for the samples Mg – 10 wt. % FeV and Mg – 20 wt. % FeV. Figure 5.6 below illustrates this, as well as the large drop in absorption capacity after the first cycle.

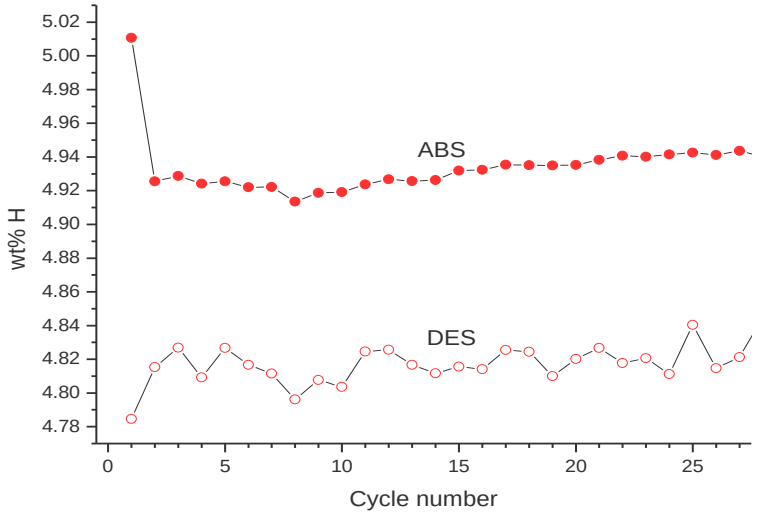

Figure 5.6: Changes in hydrogen concentration after each absorption/desorption cycle

A possible contributor to this phenomenon is the sintering of Mg/MgH_2 during re-hydrogenation. At the start of the cycling procedure, the sample temperature increases rapidly, due to the exothermic nature of the reaction. Approaching 400 °C, the sample may surpass the equilibrium temperature (T_{eq}) for the $Mg \leftrightarrow MgH_2$ transformation at the given hydrogen pressures. A similar observation was made during the re-hydrogenation of Mg – V in an earlier study [91].

5.6 SEM & TEM studies

Image quality was affected by the dielectric properties of MgH_2, particularly in the samples with low FeV content (where the effect of higher MgH_2 content was more prominent). Figure 5.7 shows some typical SEM images for selected as-milled samples.

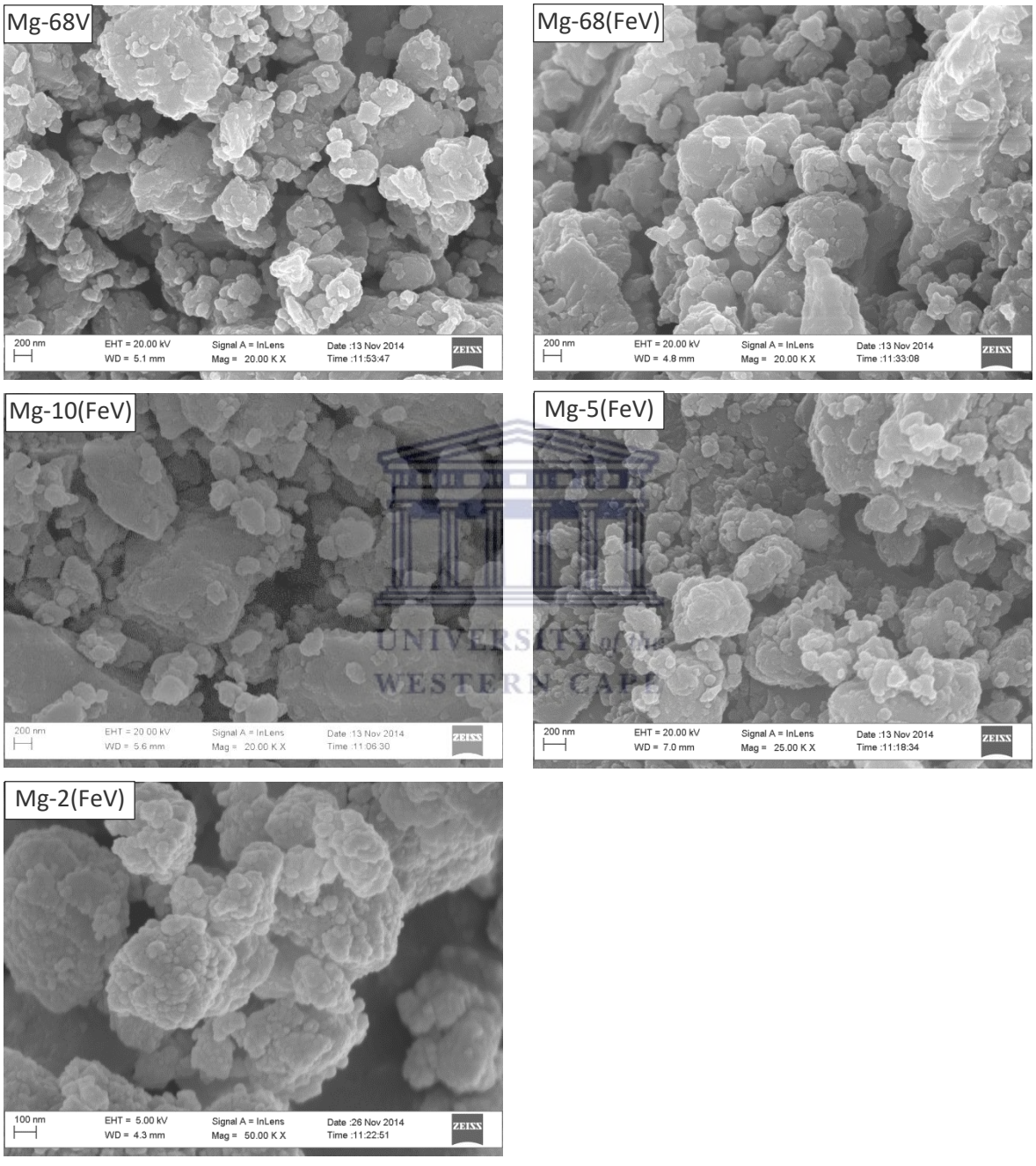

Figure 5.7: SEM images for selected as-milled samples

The samples present irregular particles ranging from ca. 100 nm to several microns in size. Some agglomeration was observed, but not as much as in previous studies [116], [152]. From Figure 5.7, it

can be generalised that higher concentrations of FeV resulted in a higher proportion of smaller particles. It was also impossible to distinguish the different constituents of the sample via visual identification. EDS data collected showed a good correspondence with the sample compositions.

Figure 5.8 below presents high resolution TEM images for the samples Mg – 68 wt. % V and Mg – 68 wt. % FeV. V-based nanoparticles (dark inclusions) are seen to be scattered on the Mg-based matrix. The SAD patterns shown on the right of Figure 5.8 provide information on the phase composition that is in agreement with the XRD results previously discussed. It is noted that the SAD pattern for the sample with FeV has more clearly defined rings as compared to the sample with pure V. This indicates that the nano-crystallite size of the sample with FeV is smaller. This finding is also in agreement with the estimation obtained via XRD.

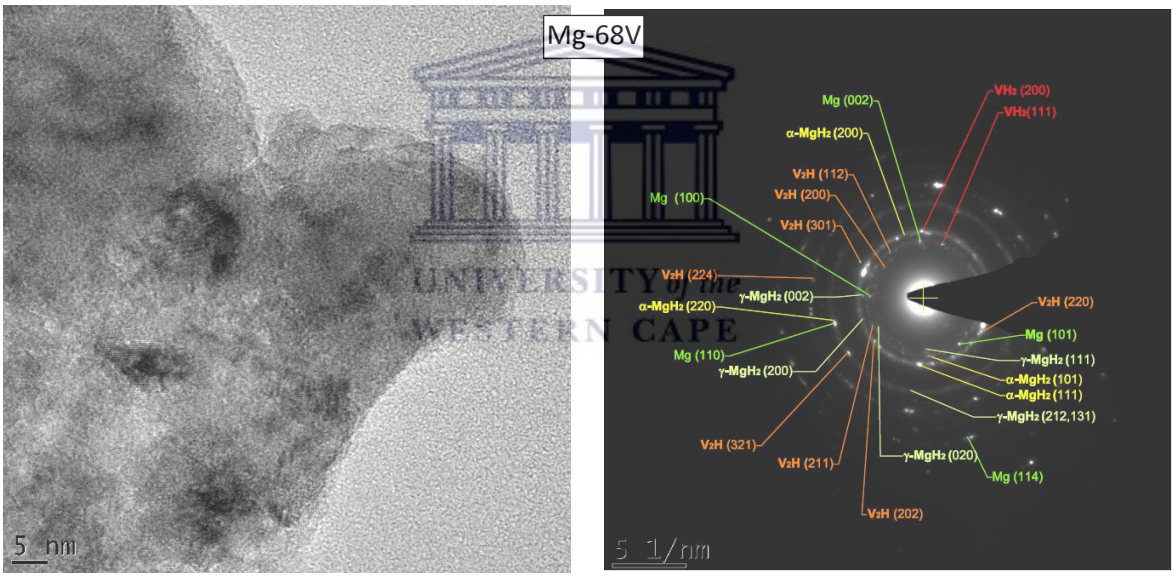

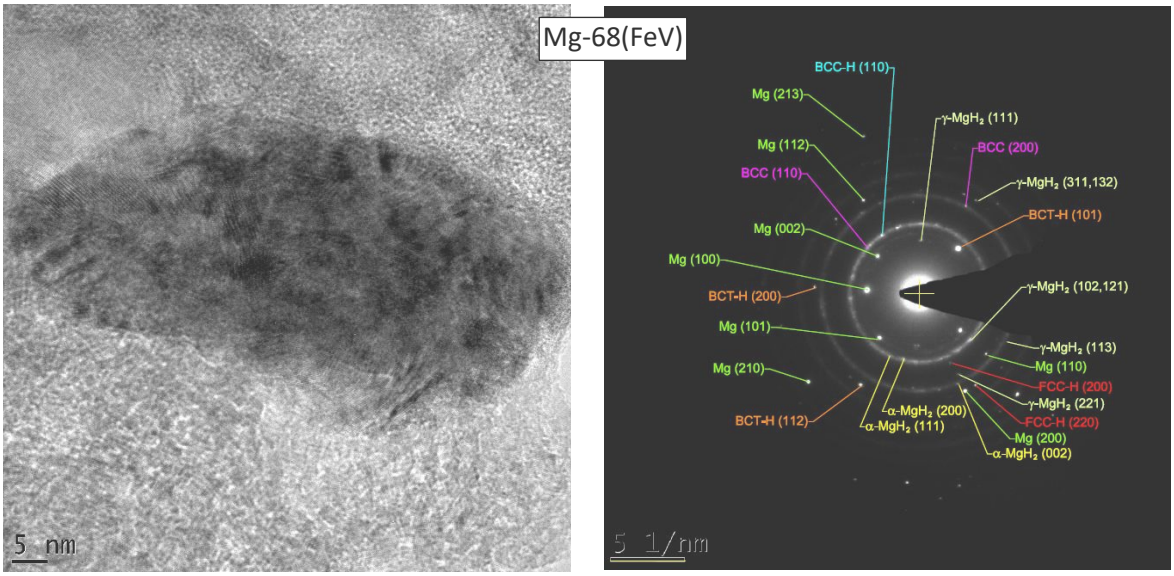

Figure 5.8: TEM images (left) and SAD patterns (right) for the as-milled samples of Mg – 68 wt. % V and Mg – 68 wt. % FeV

A comparison between the TEM images and SAD patterns for the as-milled, dehydrogenated and re-hydrogenated sample of Mg – 20 wt. % FeV indicates that de-hydrogenation causes coalescence of particles as well as the appearance of a well crystallised Mg phase. As evidenced in Figure 5.9, the BCC phase remains nano-crystalline, surmised by the rings in the SAD pattern and this corresponds well to the XRD data. Re-hydrogenation results in a similar morphology to the de-hydrogenated sample, with nano-crystalline hydrogenated BCC phase present besides well crystallised phases of α – MgH_2 and unreacted Mg.

Figure 5.9 (below): TEM images and SAD patterns for as-milled, de-hydrogenated and re-hydrogenated samples of Mg – 20 wt. % FeV

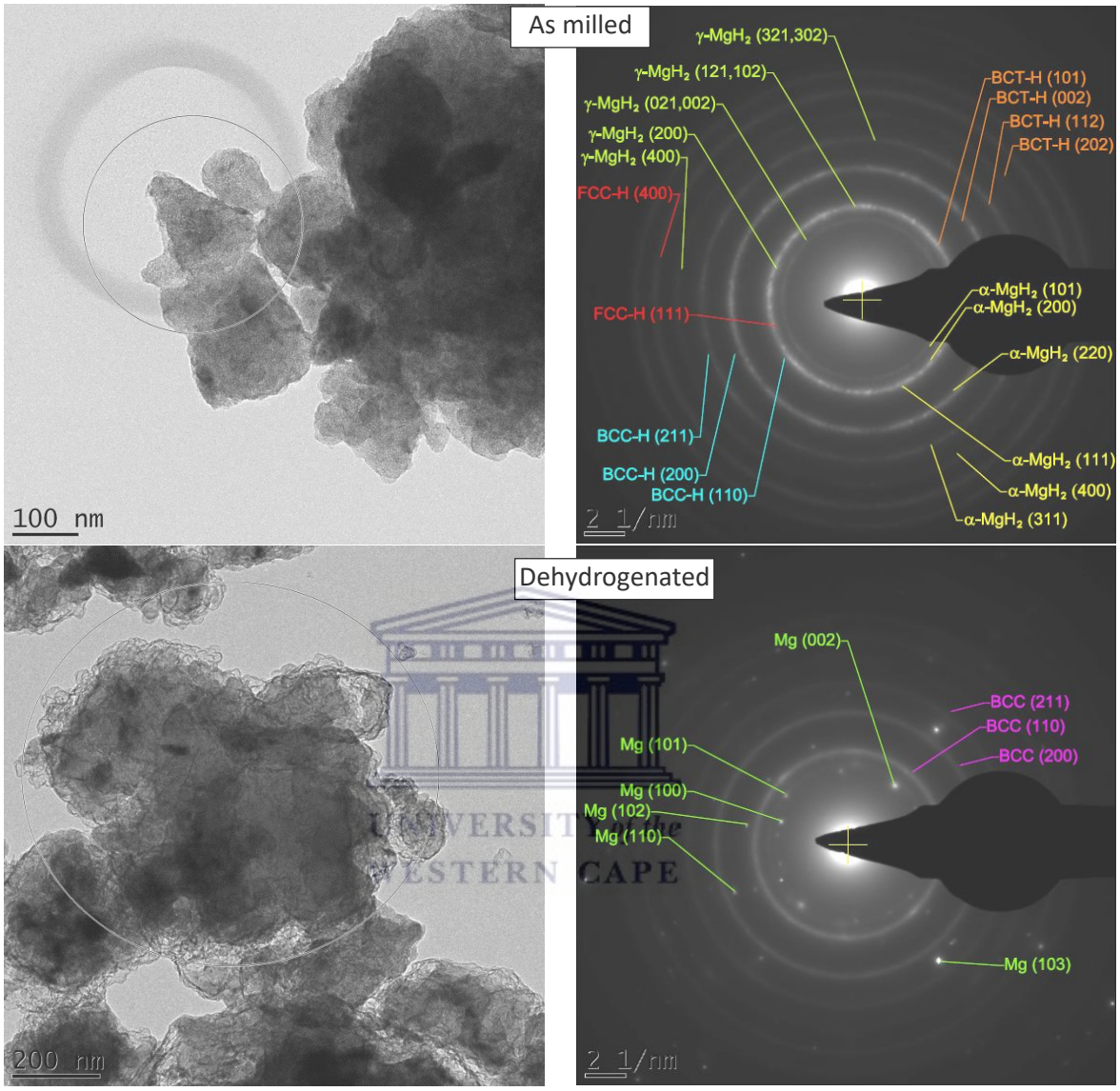

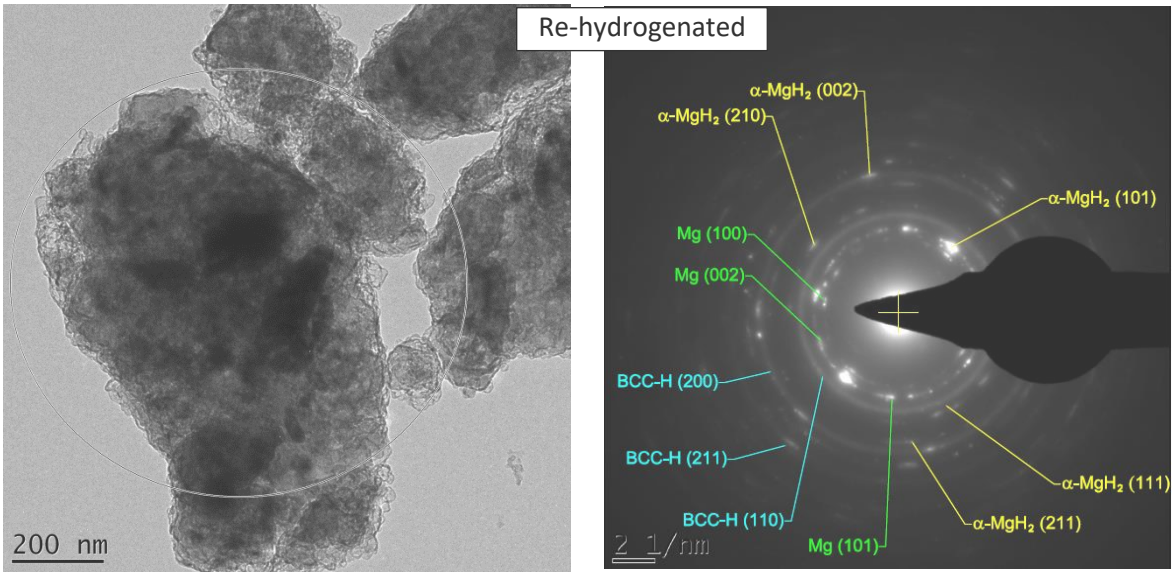

5.7 Reference experiments

For the sake of comparison and to establish a baseline, some tests detailed above were also carried out using arc melted ferro vanadium. These were prepared by arc melting V (80 wt. %) and Fe (20 wt. %). The V and Fe had purities of 99.7 % and 99.98% respectively. In terms of HRBM behaviour, the arc melted Mg – 10FeV sample exhibited a similar hydrogenation profile as pure Mg (Figure 5.10), where absorption proceeded quite slowly and required more than 3 hours to even pass 5 wt. % H storage capacity.

In both cases of commercial and arc melted FeV, hydrogen absorption capacity was 1.3 – 1.5 wt. % H, at P = 30 – 40 bar and T ≈ 20 °C. This appeared to be in good correspondence with literature [166] although the commercial variant was activated more easily. While the arc melted FeV only began absorbing H_2 in its hot state following several cycles of vacuum heating regulated at T = 450 °C followed by cooling, the commercial FeV required only 1 hour of vacuum heating before it readily absorbed H_2 at room temperature.

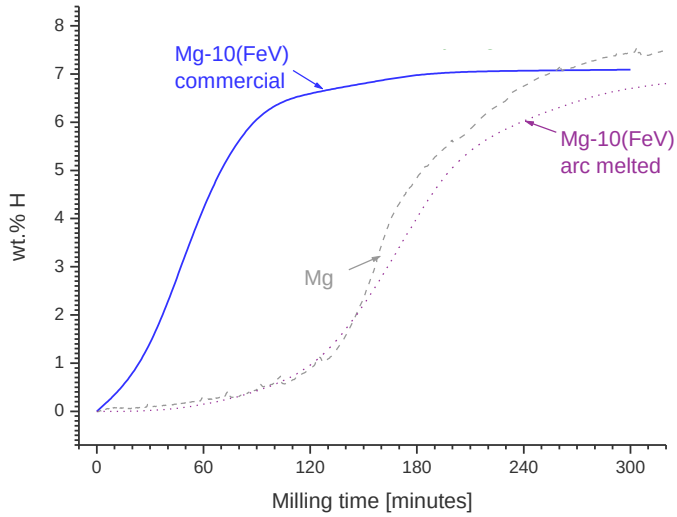

Figure 5.10: Comparison of HRBM performance between commercial FeV and arc melted FeV

5.8 Summary of Mg – FeV studies

The results presented in this chapter have conclusively shown that the addition of ferro vanadium (FeV; ca. 80 wt. % V) to Mg significantly improves hydrogen absorption/desorption performance specifically by enhancing hydrogenation during HRBM in hydrogen, as well as quickening de-hydrogenation and re-hydrogenation kinetics. The biggest improvement in hydrogen sorption performance was observed with the Mg – 10 wt. % FeV sample. This sample achieved 7 wt. % hydrogen storage capacity after only 2 hours of HRBM; subsequent calculation of activation energies yielded an improvement from 107 – 130 kJ/mol H_2 to 60 – 80 kJ/mol H_2. This represented a ten-fold improvement in hydrogenation time when compared to the hydrogenation of pure Mg under the same conditions.

The improvements noted when using FeV as an additive were less significant than when using pure V or easily hydrogenated V alloys as catalytic additives to Mg. This was attributed to incomplete hydrogenation of V when in the presence of Fe, which in itself does not bind with hydrogen as well. The Mg – FeV alloys, upon hydrogenation, contained BCC phase with < 10 nm crystallite size and a lesser occurrence of BCT – V_2H and FCC – VH with similar nano-crystallite sizes too.

Particle sintering is a common issue associated with Mg at higher temperatures. In the Mg – FeV nanocomposites, sintering during cycling resulted in an increase in particle size from 10 – 20 nm to 80 – 100 nm with no further significant enlargement. The FeV catalyst remained nanocrystalline and were well distributed across the matrix of Mg/MgH_2. This observation is likely the reason why the Mg – FeV samples were relatively stable for up to 30 cycles of absorption and desorption at 350 °C.

6.0 Investigation of hydrogen storage properties of Mg - FeV nanocomposites with additional carbon additives

The investigation of Mg - FeV nanocomposites was further extended to include carbon materials in the milling mix. Upon preparation of and characterisation of Mg – x wt. % FeV, the best overall performing sample was chosen and prepared with a selection of carbonaceous material. In this study, activated carbon (AC), multi-walled carbon nanotubes (MWCNT) and graphite (G) was used; the origins of which have been described in Chapter 3 - Experimental Methods under the Materials section.

The use of carbon in Mg – nanocomposites has roots in a previous study conducted by Lototskyy et al. [116] where it was noted that the addition of carbon improved hydrogen sorption performance, yet did not have a catalytic effect on the Mg. Further works with different Mg – nanocomposites [152] provided similar conclusions and as such the role of carbon in Mg – FeV nanocomposites was also investigated in order to better understand its role in improving hydrogen storage performance.

6.1 Ball milling hydrogenation of Mg – 10 wt. % FeV – 5C

The HRBM hydrogenation curves for Mg – 10 wt. % FeV – 5C (where C = AC, G or MWCNT) are shown in Figure 6.1 alongside the Mg – 10 wt. % FeV curve. It is first noted that none of the three samples with carbon additives achieved the same hydrogen saturation capacity as the sample without carbon. The sample with MWCNT achieved 96.4 % of its theoretical capacity while the samples with activated carbon and graphite arrived at 91 % and 88 % respectively. The Mg – 10 wt. % FeV yielded 96.6 % storage capacity. The samples containing AC and MWCNT arrived at maximum capacity within 2 hours; the sample with graphite reached ca. 6 wt. % hydrogen capacity between 4 – 5 hours of HRBM.

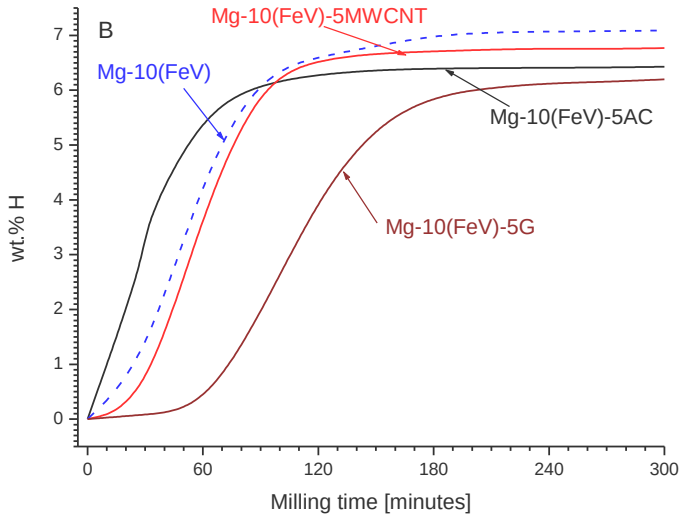

Figure 6.1: Ball milling hydrogenation curves for Mg – 10 wt. % FeV – C alloys; C = G, MWCNT or AC, hydrogenation curve for Mg – 10 wt. % FeV included as reference

The addition of AC yielded the most improvement in hydrogenation speed and exhibited faster kinetics than the sample without carbon. Within 60 minutes, this sample had achieved almost 6 wt. % hydrogen capacity. The sample containing MWCNT showed the least difference as compared to the non-carbon sample; hydrogenation kinetics were unchanged and the kinetics largely resembled the original. The addition of graphite however showed the most profound differences. Firstly, a one hour incubation period was observed at the start of HRBM followed by the slowest hydrogen uptake among the three samples with carbon additives. A similar incubation period was previously observed during the HRBM of Mg – *x* wt. % C (x = 1 – 5) in another study and it is generally understood that the sheet-like graphite material is first sheared and crushed in this duration of up to an hour before Mg is hydrogenated [116].

Table 6.1 provides a summary of the HRBM data. It is noted that because the number of milling balls were not changed throughout the study, the increase in sample weight (with the addition of carbon materials) reduced the ball-to-powder ratio slightly from 36.4 to 34.8. The data also confirms that

the sample with MWCNT showed the closest hydrogenation performance to the sample without carbon, suggesting that its contribution towards hydrogen absorption during ball milling is inconsequential or even detrimental as it only results in a reduction of hydrogen storage capacity.

Notation	BPR	Additive to Mg		wt. % H (theo-retical)[1)]	H sorption during HRBM				
		V or $V_{0.81}Fe_{0.19}$ (FeV)			MAX		Milling time [hrs] to achieve hydrogenation fraction of:		
		mol. %	wt. %		wt. % H	H/M	0.1	0.5	0.9
Mg-10(FeV)	36.4	4.32	9.09	7.32	7.07	1.93	0.3	0.9	1.6
Mg-10(FeV)-5AC	34.8			7.02	6.41	1.82	0.1	0.5	1.2
Mg-10(FeV)-5MWCNT	34.8				6.77	1.92	0.5	1.0	1.6
Mg-10(FeV)-5G	34.8				6.20	1.75	1.1	1.8	2.7

Table 6.1: Compositional analysis of samples after HRBM

Note: [(1)] – Assuming H/M=2

6.2 DSC

As mentioned in the previous chapter, the DSC spectra for the samples in this study were characterised by steep ascending fronts followed by a mildly sloping descent, and wide peaks of hydride decomposition. Samples containing carbon materials exhibited an even wider decomposition peak of up to 270 K (Mg – 10 wt. % FeV – 5AC). Figure 6.2 below presents the DSC curves for samples containing AC and MWCNT as well as the plain Mg – 10 wt. % FeV for comparison.

Unfortunately, the TGA/DSC equipment was not available for the analysis of samples containing G.

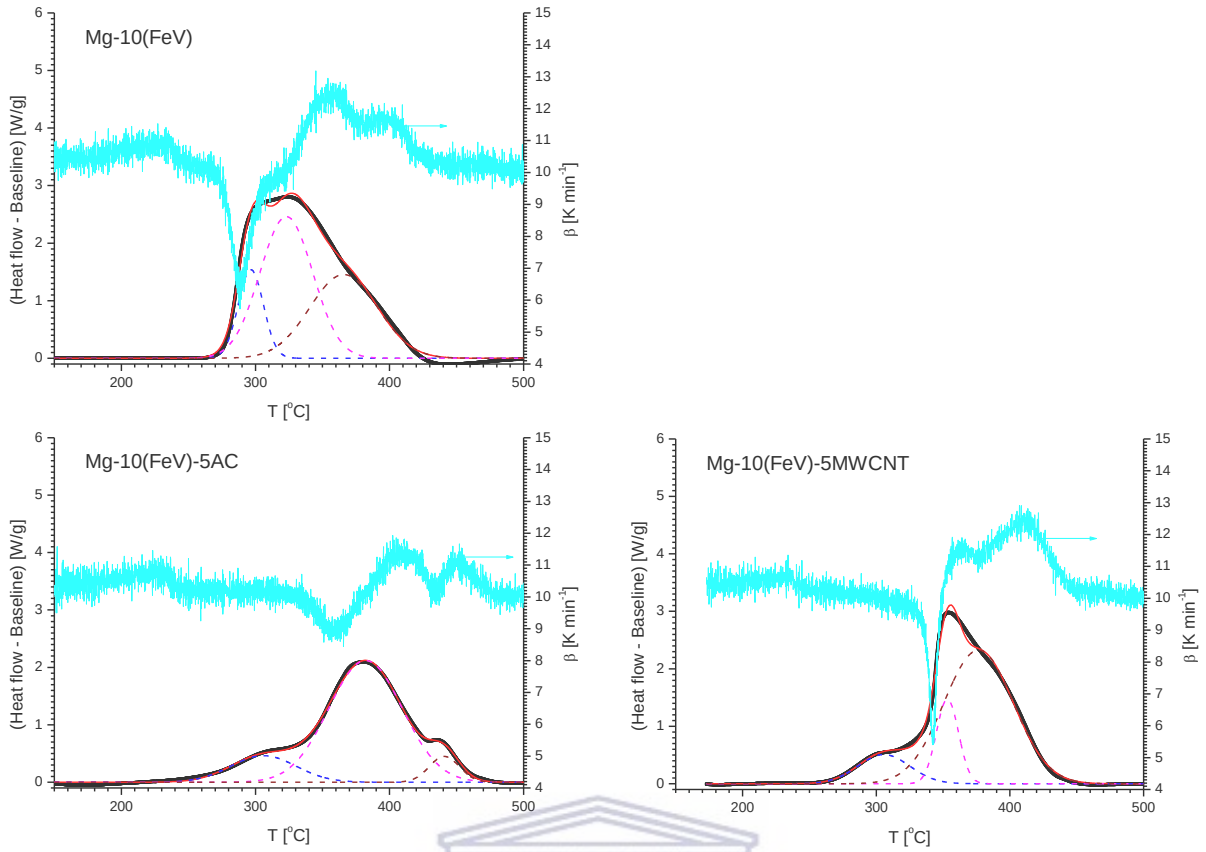

Figure 6.2: DSC curves for the as-milled samples of Mg – 10 wt. % FeV, Mg – 10 wt. % FeV – 5AC and Mg – 10 wt. % FeV – 5MWCNT; heating rate 10 K/min, experimental data (points), calculated (solid lines), constituent peaks (dashed lines), observed values of β = dT/dt are referred to the right y-axis

It is obvious that the addition of AC and MWCNT affects the original Mg – FeV nanocomposite significantly. The contribution of overlapping peaks is noticeable in both samples and the de-convolution procedure used previously in Section 5.2 is particularly effective for the data from the sample with AC. The presence of carbon in the Mg – 10 wt. % FeV sample increased the peak temperatures by 60 – 80 K, and supplied an additional peak as an energy barrier to the decomposition process. A similar observation was observed in the study of Mg – $FeTiO_3$, although the impacts of carbon in both samples were different [152].

Based on the data obtained, it was noted that the introduction of AC and MWCNT resulted in an increase in peak height and activation energies for selected peaks only. The wide peak (shown as dotted blue line in Figure 6.2) where Tm ≈ 300 °C, FWHM = 50 – 100 K plus the large range of

calculated E_A values lead to the suspicion that this peak is contributed by another process e.g. desorption of trace water adsorbed. Kissinger plots are shown in Appendix 3.

6.3 TDS and re-hydrogenation

When carbon is added to Mg – 10 wt. % FeV, the appearance of the second peak is suppressed. Furthermore, contrary to the observation made during DSC, the decomposition peak is visibly narrower when carbon is present in the samples. Figure 6.4 shows the TDS curves of samples containing carbon.

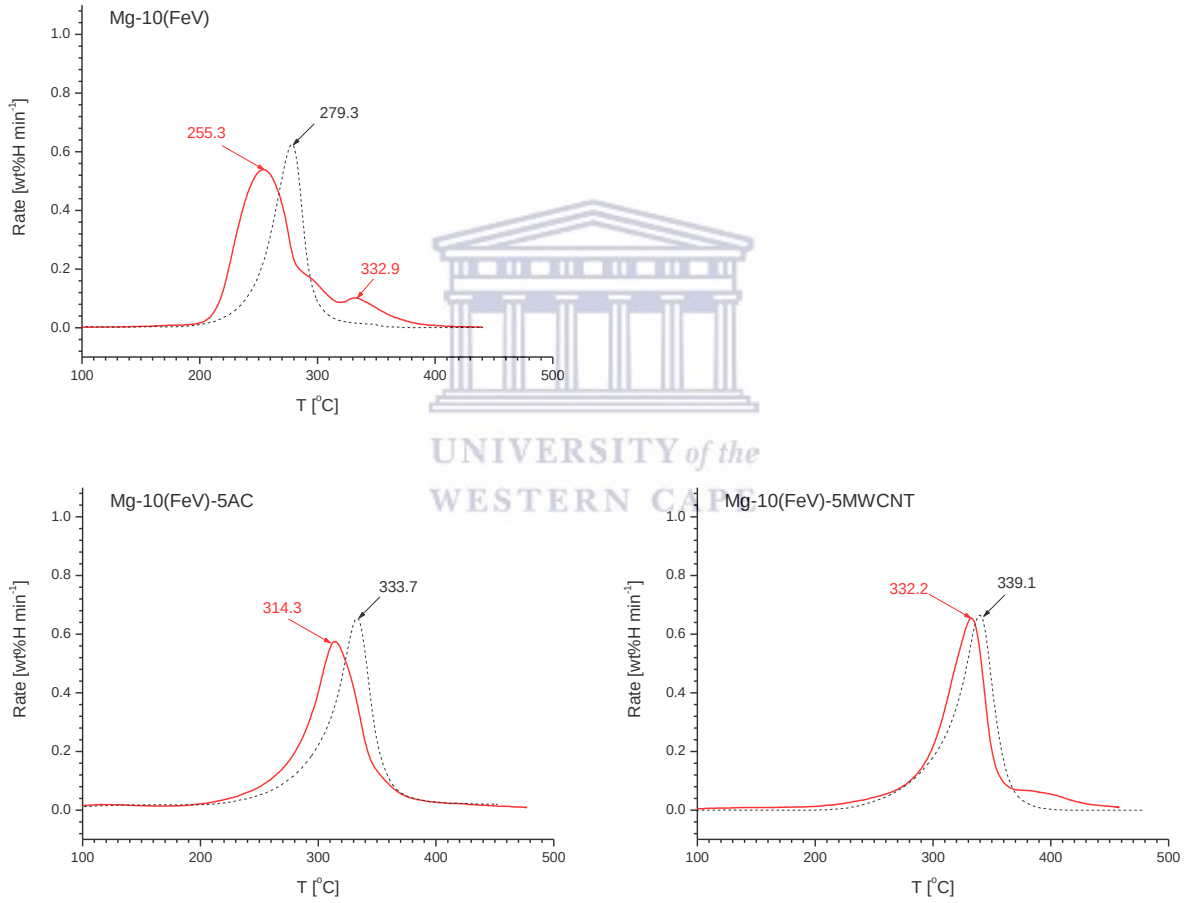

Figure 6.4: TDS curves for the as-milled (red) and re-hydrogenated (black) samples of Mg – 10 wt. % FeV, Mg – 10 wt. % FeV – 5AC and Mg – 10wt. % FeV – 5MWCNT; peak temperatures are labelled

The TDS and DSC (heating rate 5 K/min) peak temperatures correspond well to each other as was noted in the Mg – FeV samples with the larger difference observed for Mg – 10FeV – 5AC with -38 °C. The addition of carbon to Mg – 10FeV appears to stabilise the re-hydrogenation profile. In the case of MWCNT, the peak temperatures differ by less than 7 °C and this trend is followed on both the ascending and descending fronts. This stabilisation is also reflected in the smaller deterioration of hydrogen storage capacity when carbon is present, as shown in Table 6.2. In all samples, the n value was less than 1, indicating that re-hydrogenation was controlled by H diffusion.

Sample	Estimated amount of desorbed H_2 (wt. % H)		Fitted kinetic parameters of H absorption			
	1st TDS	2nd TDS	C_{max} (wt. % H)	t_0 (min)	n	R^2
Mg – 10FeV	7.1	4.8	5.169	0.52	0.305	0.96669
Mg – 10FeV – 5AC	7.2	7.1	6.685	2.82	0.424	0.99785
Mg – 10FeV – 5MWCNT	7.0	5.9	7.081	5.30	0.817	0.99709
Mg – 20FeV	6.8	4.2	4.589	4.05	0.295	0.95942

Table 6.2: Parameters of re-hydrogenation for select samples

6.4 XRD

XRD studies were carried out without complications despite the samples being exposed to air and moisture during analysis. A summary of XRD data obtained is presented in Table 6.3.

Sample	Characteristics of the constituent phases*						
	α-MgH_2	γ-MgH_2	Mg	BCT-H	FCC-H	BCC-H	BCC
Mg-10(FeV)	72.5(–) / 13 *a*=4.5169(5) *c*=3.0213(5)	22.8(3) / 19 *a*=4.545(5) *b*=5.407(6) *c*=4.956(6)	–	1.6(1) / 11 *a*=2.757(3) *c*=4.029(9)	–	13.7(1) / 5 *a*=3.012(1)	–
Mg-10(FeV)-5AC	70.75(–) / 10 *a*=4.5244(4) *c*=3.0261(4)	18.4(2) / 7 *a*=4.568(4) *b*=5.408(5) *c*=4.970(4)	–	2.94(9) / 10 *a*=2.945(2) *c*=3.237(4)	2.16(9) / 12 *a*=3.952(2)	5.71(9) / 7 *a*=3.006(1)	
Mg-10(FeV)-5MWCNT	72.6(–) / 10 *a*=4.5137(4) *c*=3.0205(4)	15.4(2) / 11 *a*=4.530(3) *b*=5.432(4) *c*=4.961(4)	1.56(5) / 370** *a*=3.21090(7) *c*=5.2136(2)	5.5(1) / 3 *a*=2.949(5) *c*=3.33(1)	1.15(7) / 26 *a*=3.935(2)	1.2(7) / 9 *a*=3.033(3)	2.6(1) / 7 *a*=2.973(3)
Mg-10(FeV)-5MWCNT – re-hydrogenated	91.9(–) / 93 *a*=4.51392(5) *c*=3.01808(6)	–	–	–	–	8.1(1) / 4 *a*=3.003(2)	–

Mg-10(FeV)-5G	76.3(–) / 40 *a*=4.5192(1) *c*=3.0224(1)	–	3.5(2) / 95 *a*=3.2117(8) *c*=5.217(2)	–	–	–	20.1(3) / 5 *a*=2.981(2)

Table 6.3: Summary of XRD data for Mg – 10 wt. % FeV samples with carbon content

Note:

*Calculated abundance [wt. %] /Crytallite size [nm]; lattice periods [Å]

**Preferred orientation plane (001)

Reference data: Refer to Appendix 4

As seen in Table 6.3 and in Figure 6.5, the as-milled samples exhibited the presence of both α- and γ – modified MgH_2 at the nanoscale, with lattice periods in good correspondence to reference data [165]. Several other phases were noted in the XRD patterns; these were identified as hydrogenated V and FeV, becoming especially prominent in the samples with 68 wt. % FeV and V.

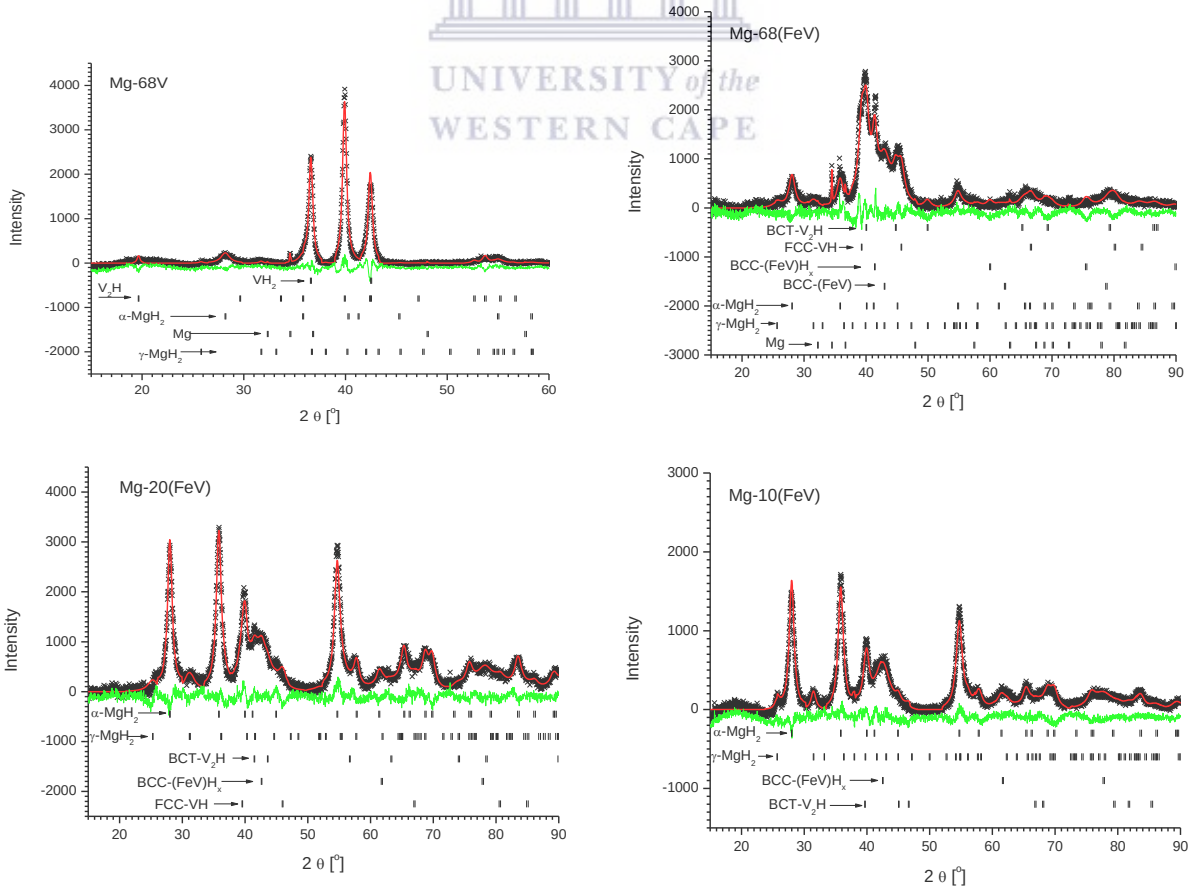

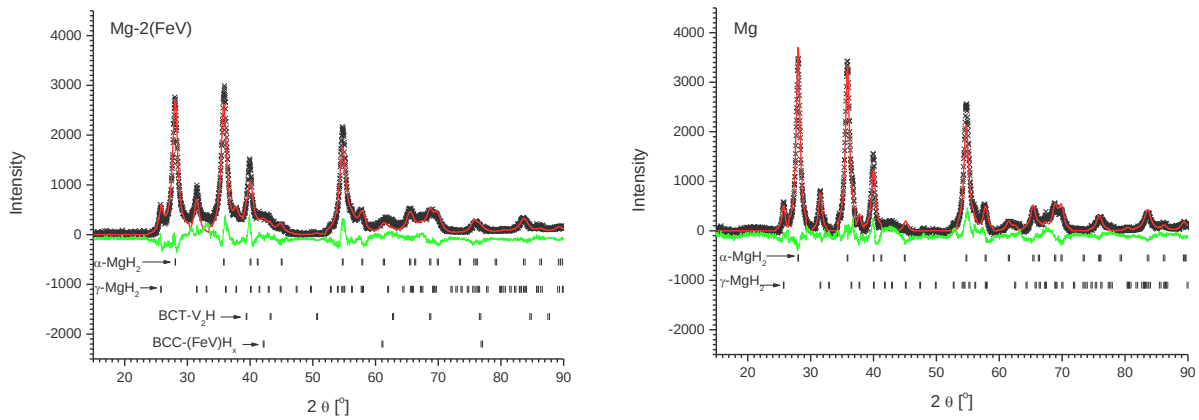

Figure 6.5: XRD spectra for the as-milled samples of Mg – 68 wt. % V, Mg – FeV and Mg

It is immediately apparent that the substitution of V with FeV causes major changes to the phase composition of the Mg nanocomposite (top two images in Figure 6.5). In the Mg – 68 wt. % V sample, well-resolved peaks corresponding to vanadium monohydride (V_2H_{1+x}) and vanadium dihydride (VH_2) were noted and these were also a good match to reference data with crystallite size ca. 45 nm [165]. On the other hand, the Mg – 68 wt. % FeV sample exhibits a much more diverse pattern. The phases found were a close match to hydride phases BCT – $(V,Fe)_2H$ and FCC – (V,Fe)H with nanocrystalline size of about 15 nm [166]. Besides that, significant amounts of non-hydrogenated BCC phase (crystallite size about 7 nm) was noted with the lattice period matching the major BCC phase in the starting FeV material. Finally, another BCC phase was matched in the XRD spectra for Mg – 68 wt. % FeV with 3.6% higher lattice period corresponding to a solid solution of hydrogen in the parent BCC. Crystalline sizes for this phase were estimated to be 15 nm.

Figure 6.5 also showed that samples with lower FeV content produced high intensities and narrower MgH_2 peaks. This corresponded well to the increase of crystallite size from 5 – 8 nm (Mg – 68 wt. % FeV) to 14 – 16 nm (as-milled pure Mg). The total calculated abundances for the FeV phases (BCC, FCC and BCT) only corresponded adequately to the content of FeV in the samples for Mg – 20 wt. % FeV. The discrepancy for samples with lower FeV content can be attributed to the low accuracy of quantitative phase analysis using XRD which is further complicated by the wide peaks of these

phases covering the range of crystallite sizes from < 5 – 12 nm, as seen in Table 6.3 These samples were noticeably missing the FCC – (V,Fe)H phase.

6.5 Cyclic studies

Cyclic studies for Mg – 10 wt. % FeV – 5C samples were performed at 350 °C with a minimum target of 50 cycles. Each cycle consisted of one desorption protocol and one absorption procedure, both run for approximately 30 minutes each. The final pressure for absorption was ca. 15 bar and for desorption ca. 3 bar; similar to the settings for samples without carbon.

While the Mg – FeV samples showed improved capacity retention over 27 – 30 hydrogen absorption/desorption cycles, the samples with additional carbon demonstrate even superior absorption/desorption capacities. Figure 6.6 (A) shows that after an initial drop in capacity (most likely due to incomplete prior desorption at P ≤ 3 bar), the absorption increases over the first 20 cycles. These levels are not maintained, as a decline of 13% occurs between cycles 25 to 98.

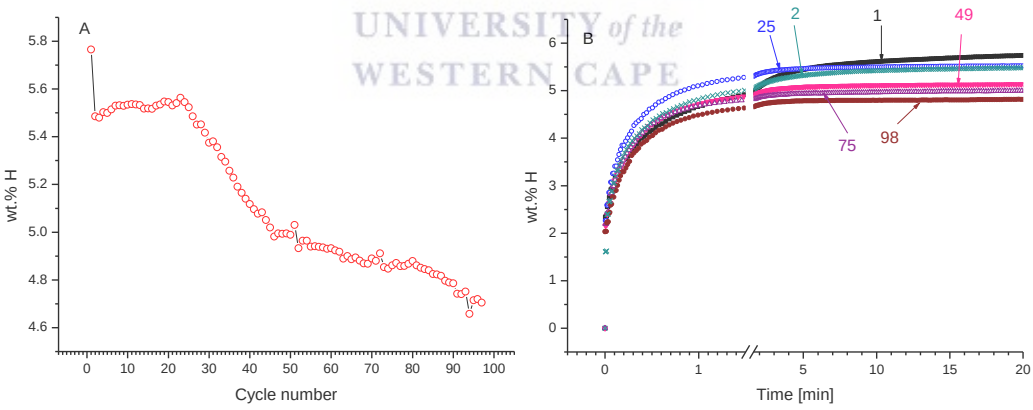

Figure 6.6: Hydrogen absorption data at P ≥ 13 bar (A), and kinetic curves for the corresponding cycle number (B) for Mg – 10FeV – 5G

Simultaneously, the hydrogenation kinetics was observed to improve over the first 10 cycles of absorption/desorption without any excessive deterioration as can be seen in Figure 6.6 (B). Over 100

cycles, the hydrogenation rate constant, K, calculated as an inverse of characteristic time (t_0) based on Equation (6) is approximately 10 min^{-1}.

A likely cause of the decline in H absorption capacity over the 100 cycles is the incremental sintering of Mg/MgH_2 during re-hydrogenation. Although the temperature during absorption is regulated at T ≈ 350 °C, the exothermic nature of the Mg hydrogenation reaction causes the reactor temperature to spike and often exceeds 400 °C at the given hydrogenation pressure. The temperature spike can be seen at the beginning of every absorption cycle in Figure 6.7 and in the case of Mg – 10FeV – 5G, appeared to spike the temperature by more than 15 °C on average.

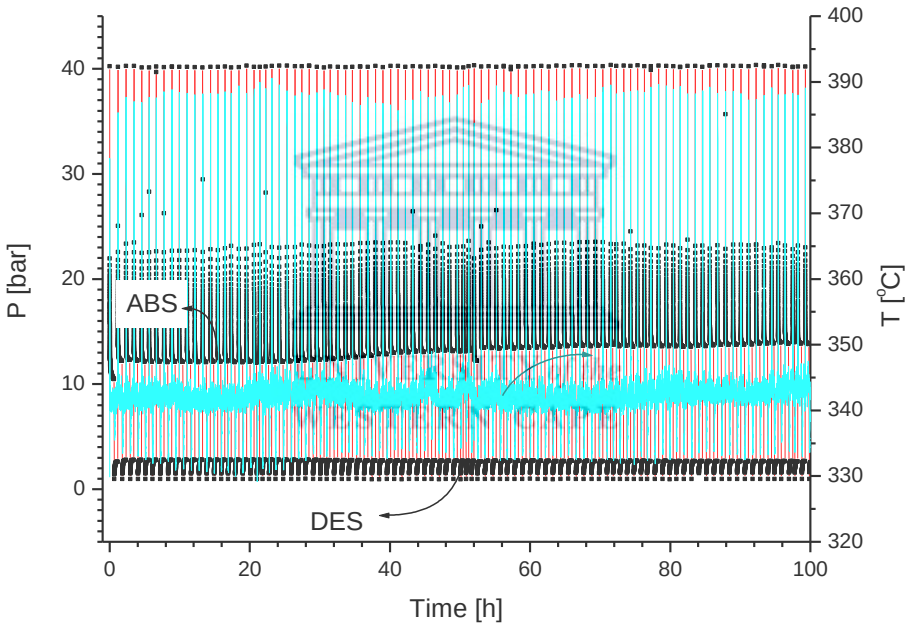

Figure 6.7: Pressure – Sample temperature data during cyclic stability studies of Mg – 10FeV – 5G

6.6 SEM & TEM studies

As compared to the Mg – FeV samples without carbon content, the samples with MWCNT and G exhibited more homogenously distributed FeV over the MgH_2 matrix. As shown in the following figures, FeV (or at least V) particles were easily identified as dark, dense spots ranging 1 – 10 nm.

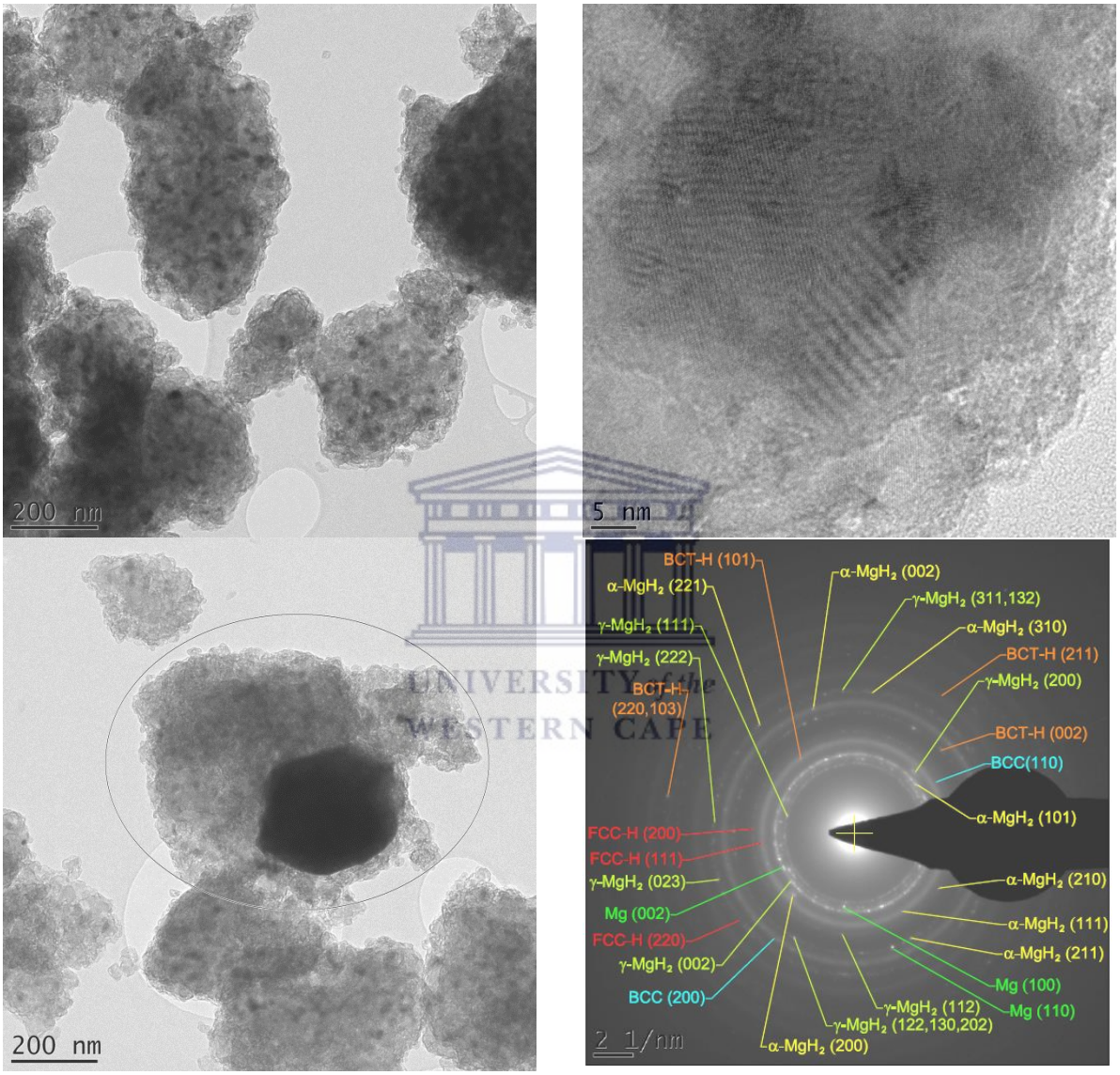

Figure 6.8: TEM images and SAD analysis of as-milled Mg – 10FeV – 5MWCNT (SAD pattern taken from circled area in adjacent image)

From Figure 6.8, the V particles present as dark inclusion in the as-milled sample (bottom left image) and correspond to the nanocrystallite wide rings in the SAD pattern (bottom right). After TDS and re-

hydrogenation, these dark inclusions become more dispersed over the lighter grey area, as in Figure 6.9. The MgH_2 is well crystallised as well.

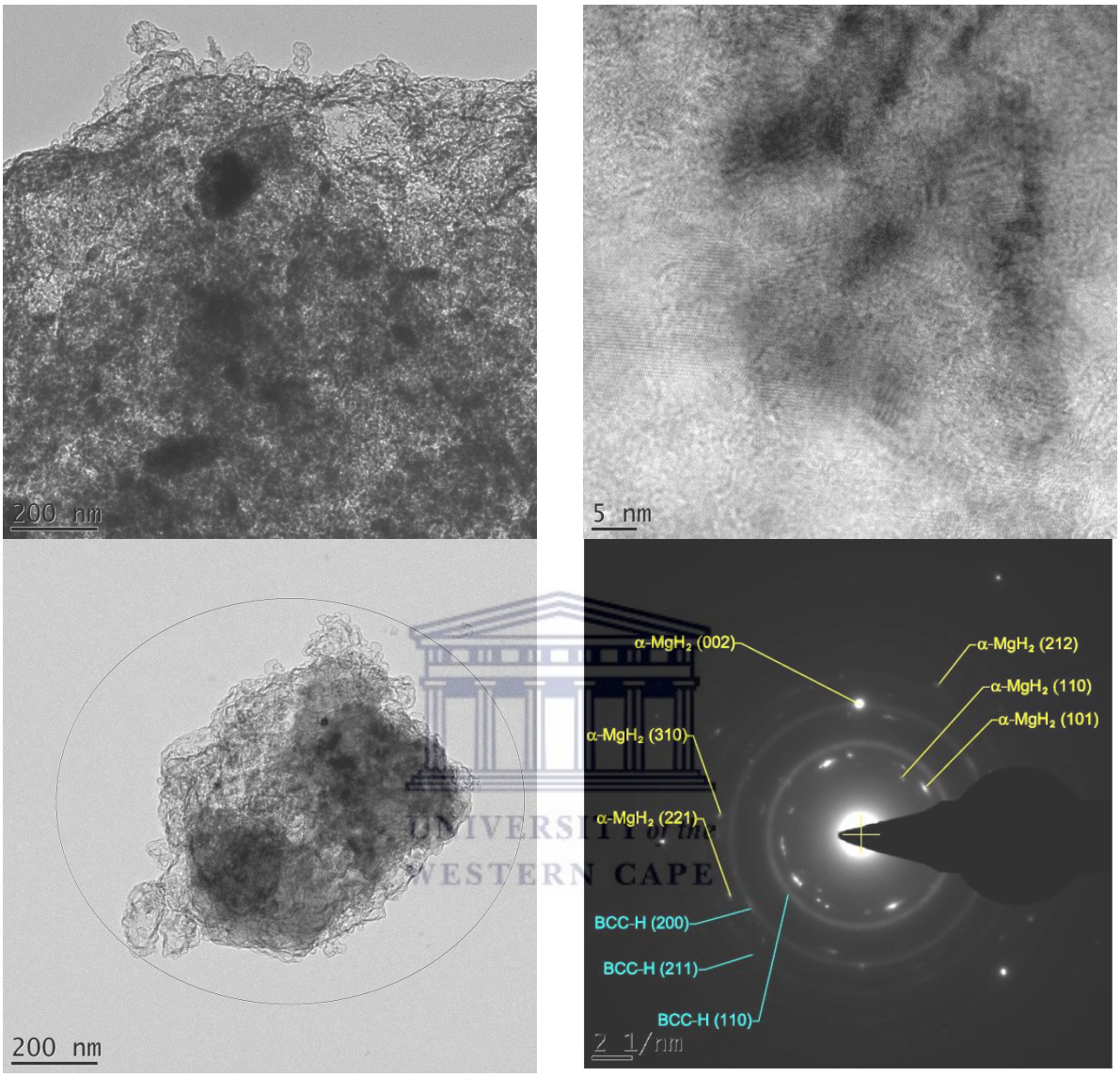

Figure 6.9: TEM images and SAD analysis of re-hydrogenated Mg – 10FeV – 5MWCNT

The sample of Mg – 10FeV – 5G shows some interesting features as well. In the as-milled state (Figure 6.10), it appears to have a multi-layered structure with dispersed V particles over the MgH_2 matrix, similar to the Mg – 10FeV – 5MWCNT sample. However, after 10 cycles of hydrogenation/dehydrogenation, the material takes on a network-like structure of very fine (ca. 10 nm) particles, as seen in Figure 6.11.

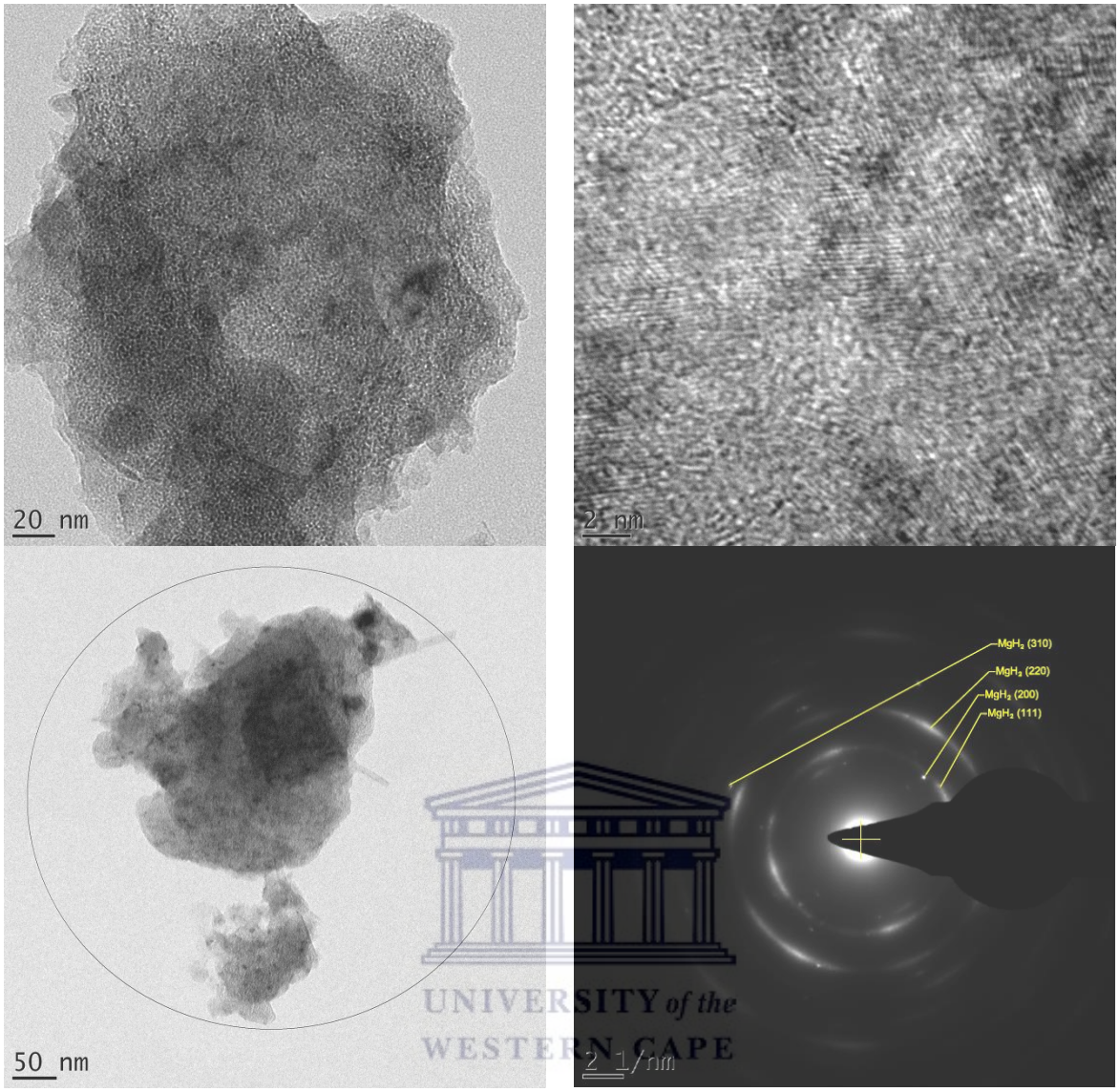

Figure 6.10: TEM images and SAD analysis of as-milled Mg – 10FeV – 5G

In Figure 6.11, the SAD pattern indicates the presence of MgH_2 nanocrystallites and BCC phases. A large spot is identified as the (002) plane from graphite but with increased d_{002} interplanar distance as compared to the reference data (as indicated with the dashed circle). When cycled up to 100 times, particle sintering is thought to occur and corresponds to the agglomerated features of submicron size in Figure 6.12. Correspondingly, the SAD patterns shows well-crystallised Mg and MgH2 and nanocrystalline BCC phase, which were in good agreement with the previously obtained XRD data.

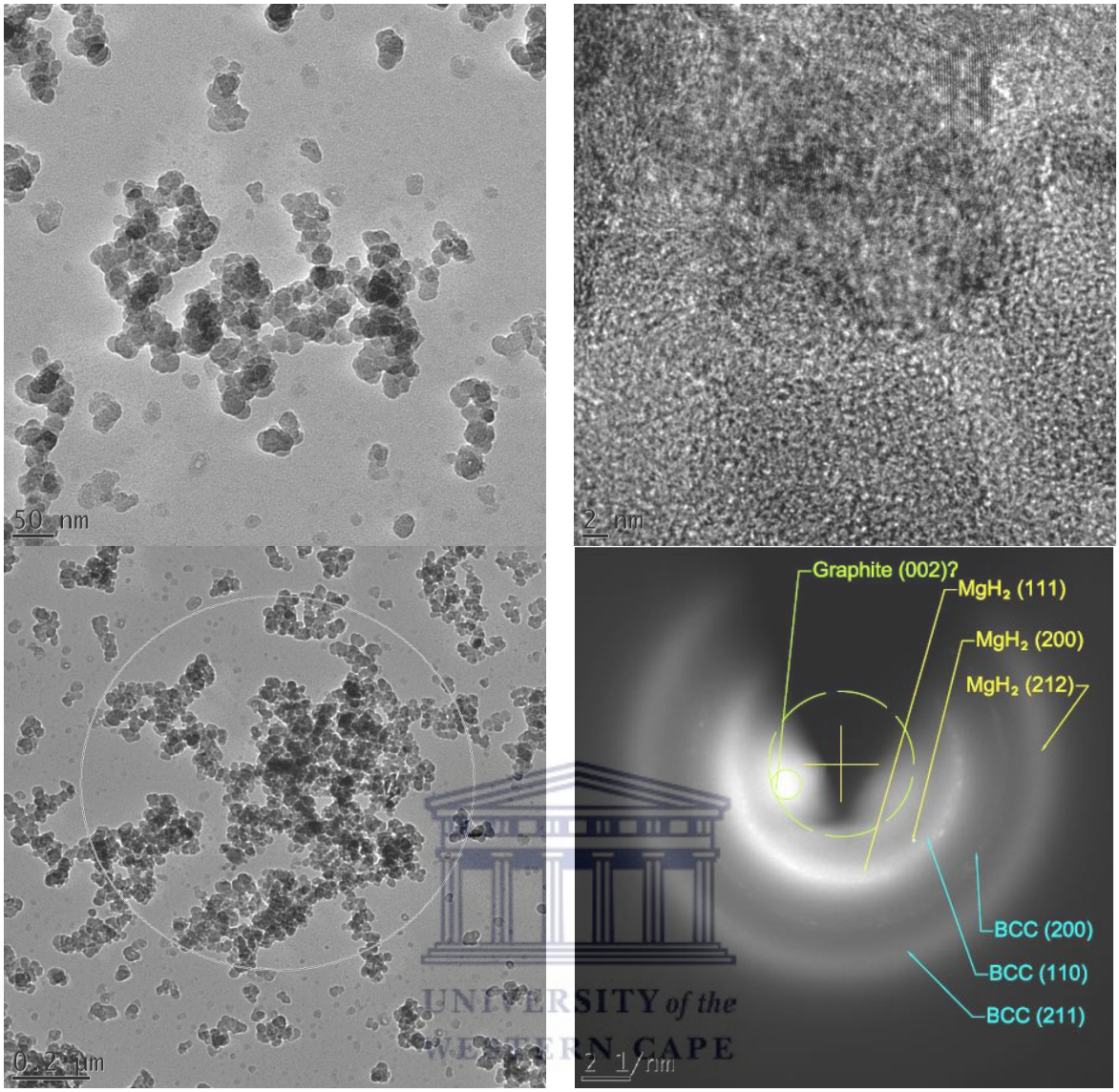

Figure 6.11: TEM images and SAD analysis of Mg – 10FeV – 5G (cycled 10 times)

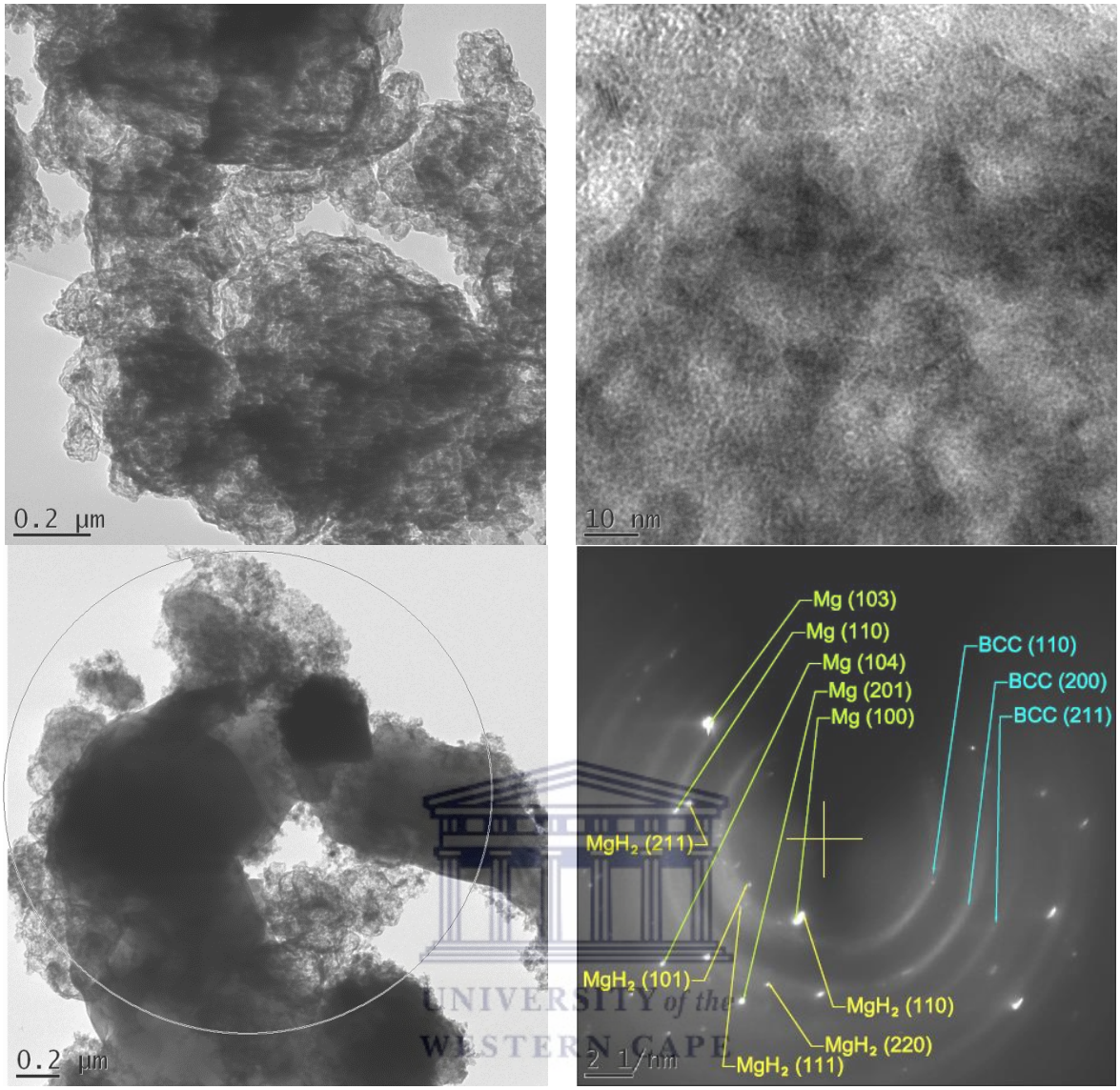

Figure 6.12: TEM images and SAD analysis of Mg – 10FeV – 5G (cycled 100 times)

6.7 Summary of Mg – 10FeV – 5C studies

It has been long suggested that the addition of carbonaceous material in addition to known catalytic metal has a beneficial impact on the hydrogen sorption performance of MgH_2 without directly influencing the catalysis itself. None of samples containing carbon additives in this study showed any increase in desorption/absorption kinetics; it actually slowed hydrogen kinetics down. However, this may not be an entirely negative result as it is known that the formation of MgH_2 actually impedes the diffusion of H atoms into the unreacted Mg [167]. As such, slowing down kinetics slightly may afford the material enough time to transition through the MgH_2 phases more effectively.

The carbon material appears to have a more facilitative role and possibly in maintaining the most efficient pathways for hydrogen permeation through the Mg/MgH_2 matrix. The samples containing graphite showed further grain refinement which resulted in the improvement in hydrogenation kinetics over the first 30 cycles as well as a higher reversible storage capacity. To this end, a balance needs to be found that preserves the highest storage capacity without excessive deterioration of hydrogen sorption kinetics.

7.0 Investigation of $Mg_{0.9}Ti_{0.1}$ performance as hydrogen storage material (joint study)

7.1 Introduction and Disclaimer

Our collaborators at the Institute for Energy Technology (IFE) in Norway synthesised and performed some characterisation studies on Mg – Ti nanocomposites. The rationale for using Ti as an additive to Mg was as a milling aid [137] as well as to improve the rate of hydrogenation [93], [168]. The main issue when using this material combination was the loss of reversible hydrogen storage capacity after cycling at high temperature (350°C). Poor cyclic stability is attributed to a number of factors, more notably the presence of contaminants in the hydrogen gas [169] and material sintering under thermal cycling, which is particularly true for Mg based nanocomposite [106]. The addition of carbon species enhances the absorption-desorption cyclic stability and refines the size of MgH_2 crystals in the alloy [116]. In practice, the addition of carbon to the Mg composite delays the onset of hydrogenation during ball milling, although hydrogenation rates were unchanged.

All materials used in this study were synthesised and characterised at IFE while the TEM studies (including SAD, EDS and EELS) were carried out at UWC. XRD patterns were obtained by iThemba labs and subsequently analysed at UWC. As such, only the results obtained at UWC will be discussed in the following section.

7.2 Scope

In this work, various combination ratios of Mg – Ti were produced but it was the $Mg_{0.9}Ti_{0.1}$ – 5 wt. % G sample that showed outstanding cycle life performance. As shown in Figure 8.1, the sample of $Mg_{0.9}Ti_{0.1}$ showed a 42% decrease in hydrogen absorption capacity after 30 cycles of absorption and desorption. On the other hand, the $Mg_{0.9}Ti_{0.1}$ – 5 wt. % G sample demonstrated exceptional resilience, losing only 2% hydrogen storage capacity over 105 cycles. As the only difference between the two samples was the inclusion of graphite in the formulation, a simple study was initiated. In

order to analyse the role of graphite in maintaining high hydrogen storage capacities over many cycles, samples with and without carbon graphite were both analysed in their as-milled and post-cycling state.

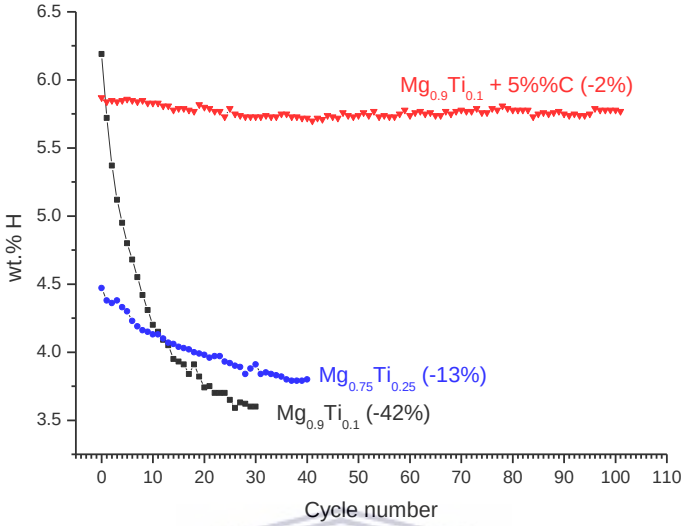

Figure 7.1: Reversible hydrogen storage capacity at T=350°C. Values in brackets specify percentage capacity losses

7.3 Ball milling hydrogenation of Mg – *x* wt. % Ti

HRBM of all samples proceeds almost to their theoretical value, as shown in Table 7.1 below.

Sample (theoretical wt. % hydrogen)	Milling time (min)	H absorption			Parameters fitted based on Eq. 6			
		wt. % H	Ncm^3/g	H/M	Cmax (wt. % H)	K (min^{-1})	n	R^2
Mg (7.66)	390	7.36	890.2	1.91	7.25(9)	0.00486(6)	3.1(1)	0.9981
Mg + 5C (7.29)	360	7.28	879.4	1.89	7.1(1)	0.016(4)	2.6(7)	0.9963
$Mg_{0.9}Ti_{0.1}$ (7.03)	240	6.62	788.0	1.88	6.60(6)	0.0152(2)	1.79(65)	0.9987
$Mg_{0.9}Ti_{0.1}$ + 5C (6.71)	240	4.63	763.4	1.91	6.28(8)	0.0158(3)	2.4(1)	0.9970
$Mg_{0.75}Ti_{0.25}$ (6.26)	240	6.18	732.3	1.97	6.09(4)	0.0287(6)	1.40(5)	0.9987
$Mg_{0.5}Ti_{0.5}$ (5.29)	240	5.21	611.2	1.97	5.22(2)	0.0513(7)	1.42(4)	0.9996

Table 7.1: HRBM parameters for Mg – Ti nanocomposites

Samples were hydrogenated almost to completion (>94%) with H/M values approximately 2. While the pure Mg and Mg + 5C samples required upwards of 6 hours to achieve saturation, the samples containing Ti were completed in about 90 minutes. More notable is that the $Mg_{0.5}Ti_{0.5}$ sample achieved maximum capacity after 40 minutes, as shown in Figure 8.1.

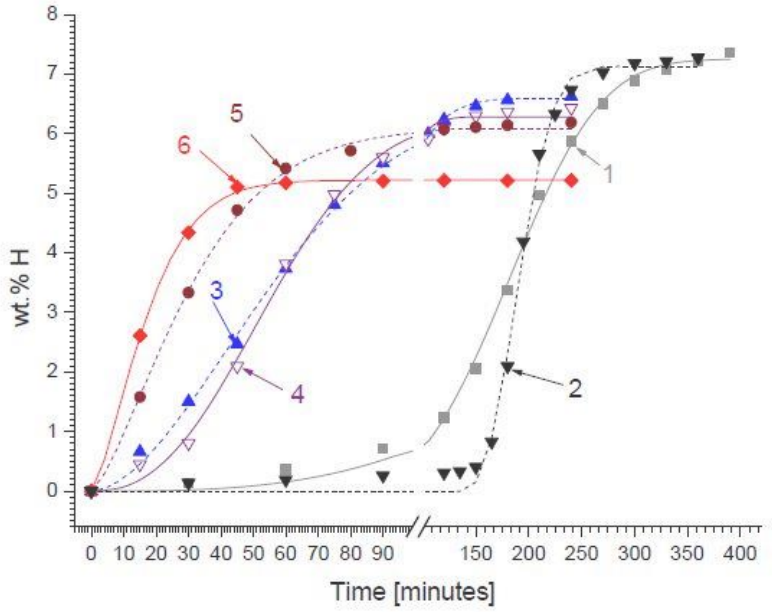

Figure 7.2: HRBM hydrogenation of 1 - Mg, 2 - Mg + 5C, 3 – $Mg_{0.9}Ti_{0.1}$, 4 – $Mg_{0.9}Ti_{0.1}$ + 5C, 5 – $Mg_{0.75}Ti_{0.25}$, 6 – $Mg_{0.5}Ti_{0.5}$; experimental points and calculated curves

It can also be seen in Figure 7.2 that the increase in Ti content increases the rate of hydrogen uptake, evidenced by the increasingly steep slopes. The addition of Ti itself (and subsequently graphite) resulted in significant changes to the hydrogenation mechanism as evidenced by changes of the Avrami exponent, n and reaction rate constant, k.

As shown by Cahn [170], limitations associated with nucleation origin sites may decrease the Avrami exponent, broadly n=3 when nucleation proceeds at points, edges (n=2) and at surfaces (n=1). Non-integer values of n can be attribution to the additional contribution of diffusion [171] coupled with, or alternatively the change of the nucleation mechanism during the reaction [65].

In Table 7.1, the hydrogenation of unmodified Mg during HRBM (n≈3) exemplifies the “classic” nucleation and growth mechanism while in Mg-Ti compositions (n≈1.5, k increased 3-10 times) the contribution of diffusion and/or limitation associated with the nucleation regions but with the faster nuclei formation becomes evident. Mg-Ti composites with added graphite, where n≈2.5 and k

increased approximately 3 times, exhibit intermediate performance indicating mixed nucleation and growth with diffusion mechanism of hydrogenation.

7.3 Role of carbon

Previous work by Lototskyy et al. [116] established a non-catalytic role for carbonaceous materials in Mg based nanocomposites. It was suggested that carbon additives are destroyed during HRBM and then reform into graphene layers that coat the MgH_2 nanoparticles and prevent excessive grain growth. This effect contributes to improved absorption-desorption cyclic stability and the maintenance of nano-sized MgH_2 crystals in re-hydrogenated Mg nanocomposites that contain carbon.

In a separate study [152] on the effect of titanium-iron oxide on the hydrogen storage performance of Mg, the addition of carbon corresponded to improved re-hydrogenation of Mg where 5 wt. % H_2 was absorbed in less than 10 minutes (<15 bar H_2, T=250°C).

Carbon additives served instead as a 'carrier' of activated hydrogen and quantities above 1 wt. % were found to prohibit fast hydrogenation kinetics. It was indicated in the current study that the $Mg_{90}Ti_{10}$ sample was the best performing in terms of hydrogenation kinetics

7.4 TEM and Elemental mapping

TEM and elemental analysis were performed to evaluate the changes in the material structure and morphology after cycling and to elucidate the root cause behind the exceptional cyclic stability of the sample containing graphite.

Certain areas of as-milled $Mg_{0.9}Ti_{0.1}$ contained purely TiH_2, as shown in Figure 7.3. It was noted that the calculated weight abundances of TiH2 in the as-milled samples were higher than that defined by stoichiometry i.e. 20% for $Mg_{0.9}Ti_{0.1}$ and 19% for $Mg_{0.9}Ti_{0.1}$ – 5C. Upon cycling, the abundance of TiH2 further increased by 19% for the $Mg_{0.9}Ti_{0.1}$ after 30 cycles but only by 4% for the $Mg_{0.9}Ti_{0.1}$ – 5C sample after 105 cycles.

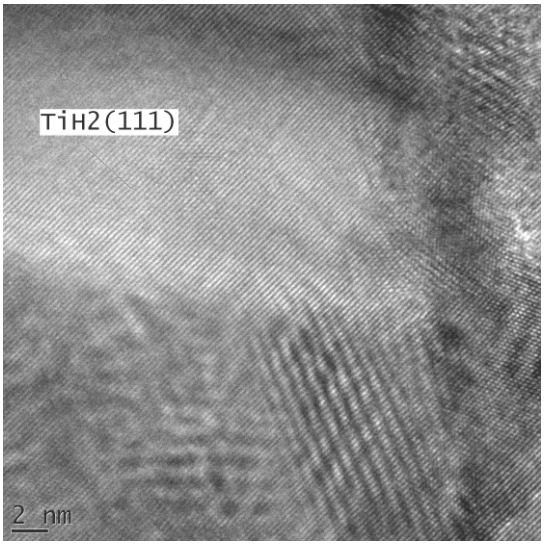

Figure 7.3: TEM image of as-milled Mg0.9Ti0.1 showing a zone of pure TiH2 phase (111)

The subsequent figures are elemental maps that illustrate the structure and morphology of samples before and after cycling. These images were obtained with Electron Energy Loss Spectroscopy (EELS) using the TEM apparatus and allowed for precise mapping of elements within the thin sample bulk. By comparing the images of samples before and after cycling, the changes that occur can be analysed and correlated to the absorption-desorption cycling performance.

In Figure 7.4 below, the as-milled $Mg_{0.9}Ti_{0.1}$ sample is shown to have a homogenous and well distributed density of Mg throughout. Pockets of low Mg density are filled with Ti as can be clearly seen in the overlayed image. The well distributed and fine particles of Mg were created as a result of sufficiently long ball milling.

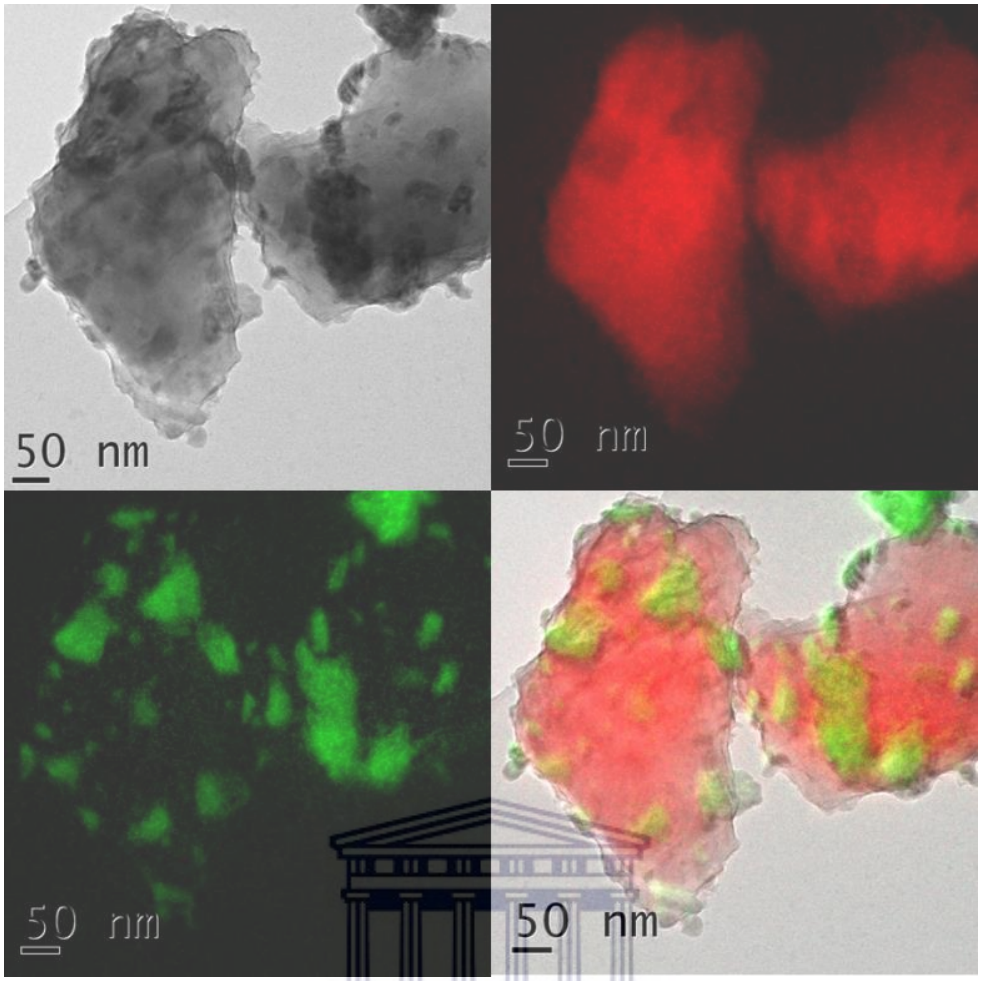

Figure 7.4: Elemental mapping image of as-milled Mg0.9Ti0.1; top left: filtered TEM image, top right: Mg map (red), bottom left: Ti image (green), bottom right: overlayed image

Following 30 cycles of absorption and desorption at 350 °C, several changes in material structure were noted. Figure 7.5 shows some segregation and agglomeration of Mg particles from a previously homogenous distribution. This suggests some level of sintering which in turn corroborates the decrease in hydrogen storage capacity of the sample. In contrast, the previously patchy clusters of Ti have become more homogenous and evenly distributed throughout the sample.

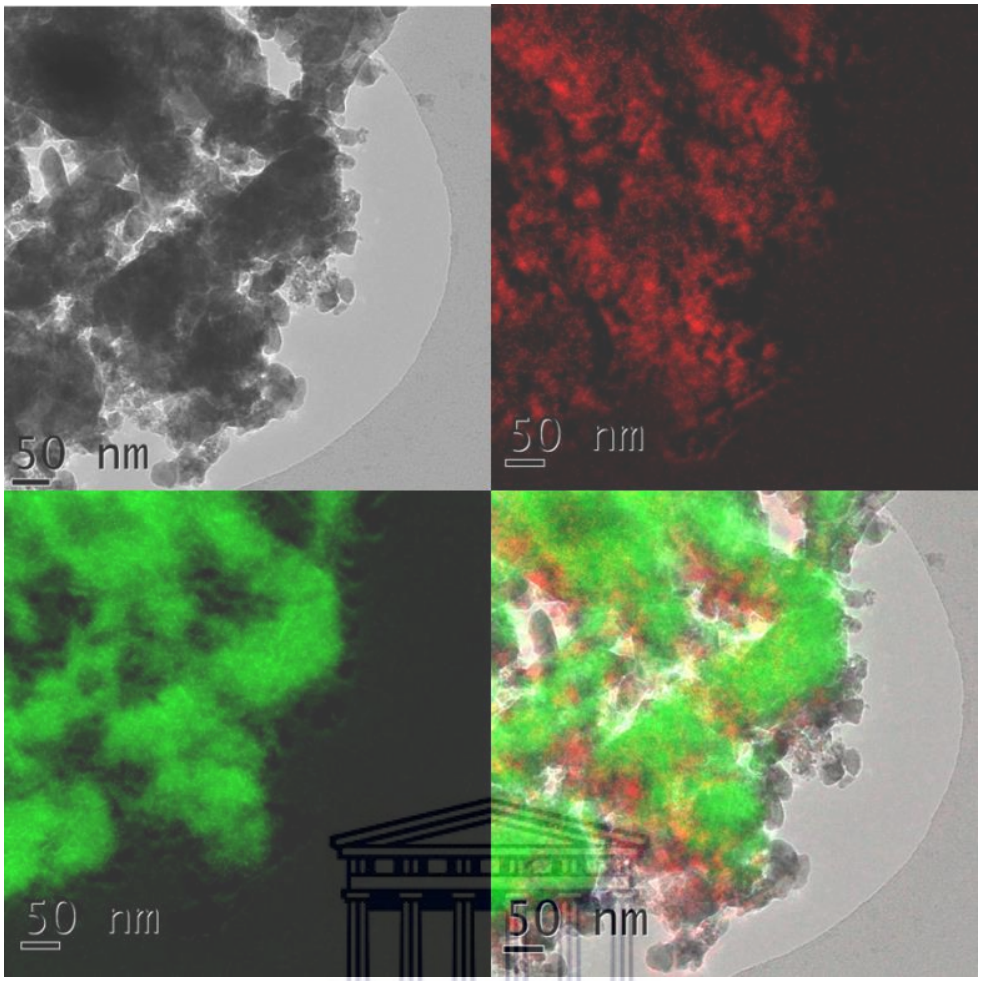

Figure 7.5: Elemental mapping image of Mg0.9Ti0.1 after 30 cycles; top left: filtered TEM image, top right: Mg map (red), bottom left: Ti image (green), bottom right: overlayed image

The elemental map for as-milled $Mg_{0.9}Ti_{0.1}$ – 5 wt. % G is shown in Figure 7.6. Once again, there is a homogenous distribution of Mg throughout the sample with pockets where Ti particles are clustered into areas of high density, [possibly on the surface of the Mg/MgH_2 matrix. The carbon distribution overlaps the Mg and Ti and appears to be slightly networked. (The blue carbon curved wall corresponds to the holey-carbon Cu grids used for TEM and should be disregarded)

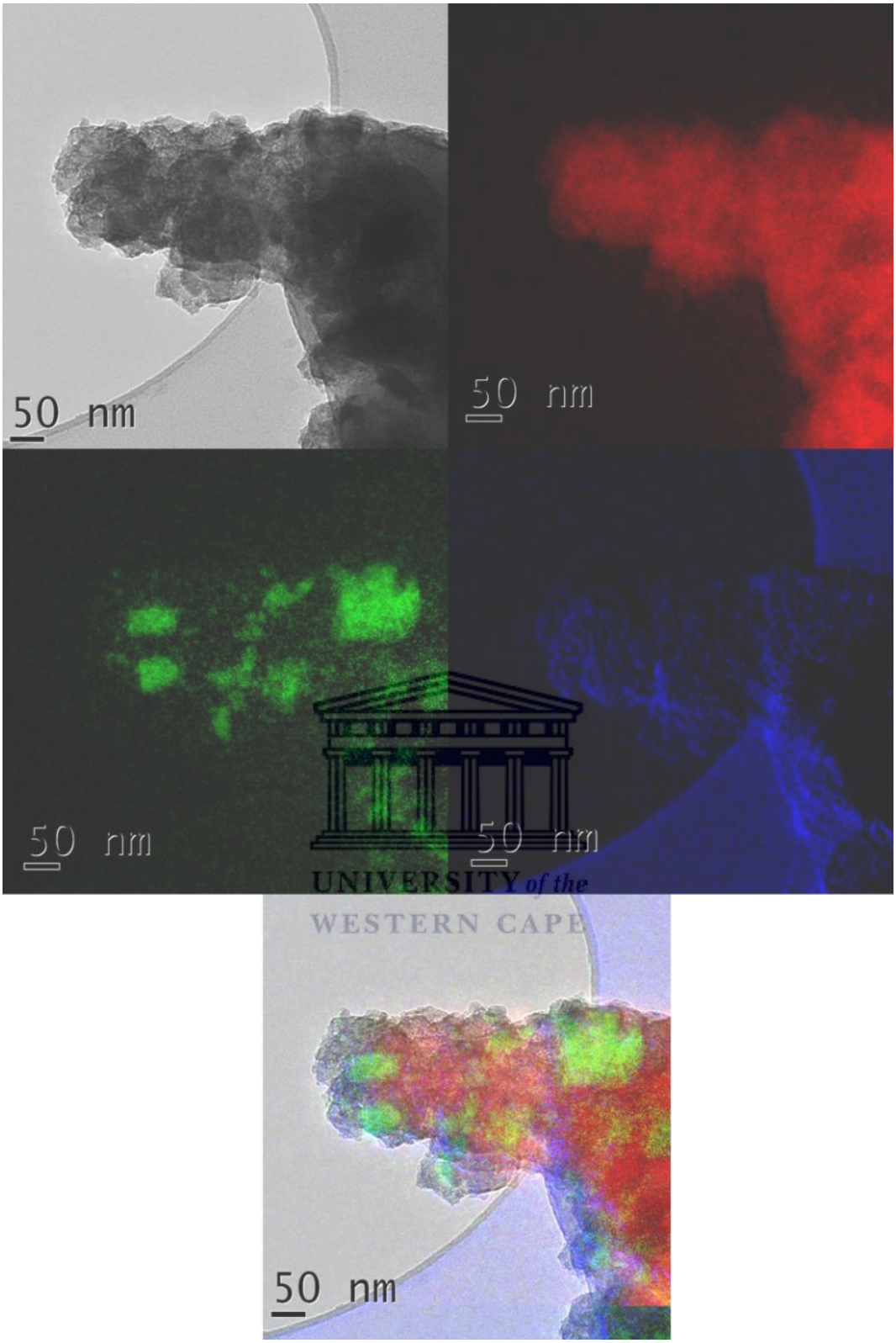

Figure 7.6: Elemental mapping image of as-milled Mg0.9Ti0.1– 5 wt. % G; top left: filtered TEM image, top right: Mg map (red), middle left: Ti image (green), middle right: C map (blue) bottom: overlayed image

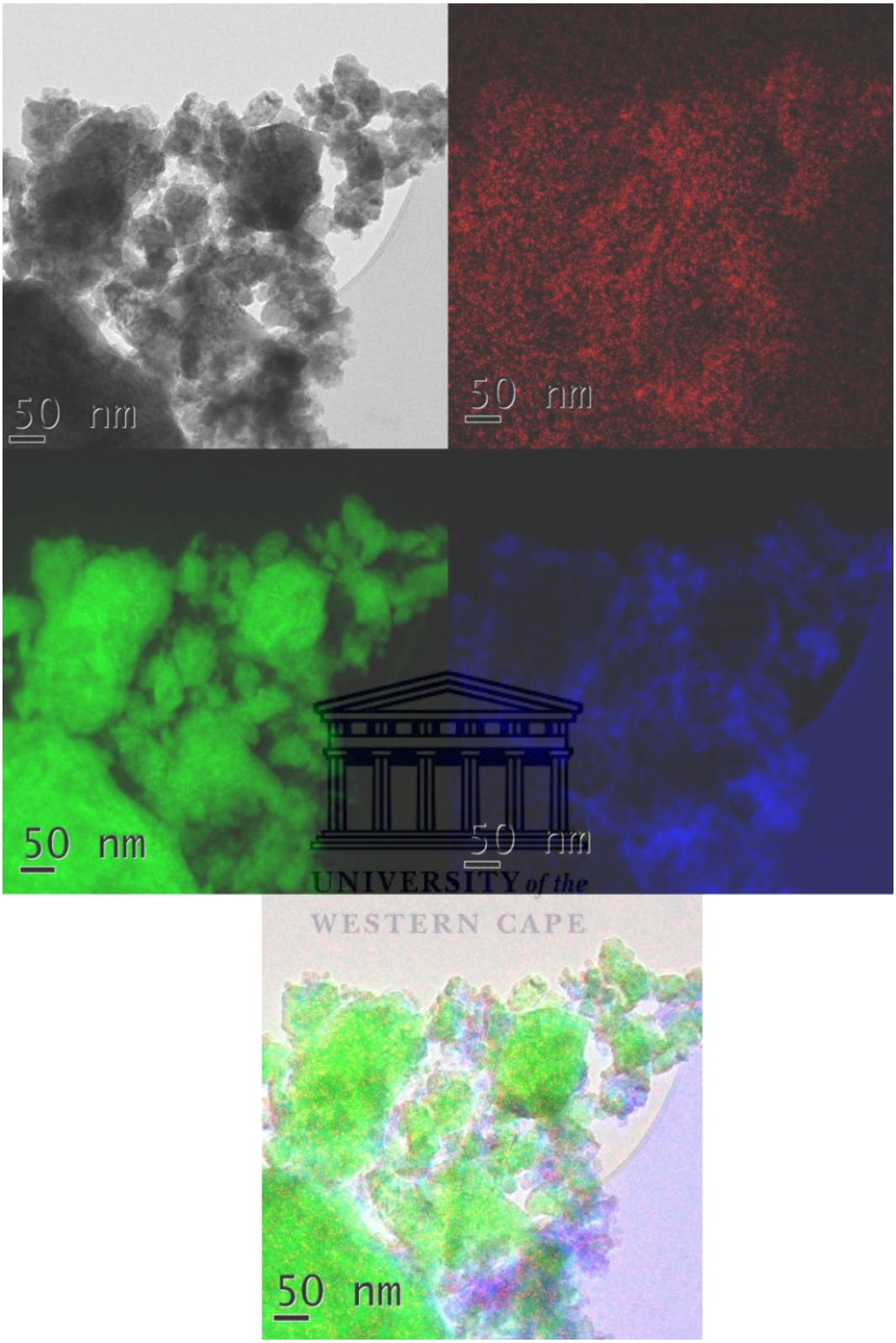

Figure 7.7: Elemental mapping image of Mg0.9Ti0.1– 5 wt. % G after 105 cycles; top left: filtered TEM image, top right: Mg map (red), middle left: Ti image (green), middle right: C map (blue) bottom: overlayed image

After 105 cycles, it was observed that the Mg (5 – 10 nm) did not aggregate and sinter so extensively as in the sample without graphite. The particles appeared to be even more refined than before cycling, and were more distinct in the image obtained. Furthermore, the distribution of Ti was also clustered but distribution on the grains. There was no apparent change in the morphology of carbon and the structure still appeared networked. The bottom image in Figure 7.7 also indicates that the Mg and Ti particles are overlapping and that the carbon is distributed primarily along the grain.

The segregation of TiH_2 particles around the Mg particles may impede the irradiation of Mg during analysis, thus resulting in the overestimation of TiH_2 abundances in the calculations.

7.5 XRD and phase analysis

XRD results for the as-milled samples showed the presence of nanocrystalline (<20nm) TiH_2, α-Mg H_2 and γ–Mg H_2. In the corresponding dehydrogenated (at 400 °C) sample, the α-Mg H_2 phase is transformed into Mg but the TiH_2 remains. The lattice periods for the phases identified in the XRD analysis matched reference data adequately. Table 7.2 summarises the information obtained from XRD analysis for samples $Mg_{0.9}Ti_{0.1}$ and $Mg_{0.9}Ti_{0.1}$ – 5 wt. % G, before and after cycling.

Sample	Mg				TiH_2				
	Abund-ance [wt. %]	*a* [Å]	*c* [Å]	Crystal-lite size [nm]	Abundance [wt. %]	*a* [Å]	Crystal-lite size [nm]	Strain [%]	*Rp*
$Mg_{0.9}Ti_{0.1}$	78.2(-)	3.2002(8)	5.195(1)	28	21.8(6)	4.432(2)	12	0	0.0099
$Mg_{0.9}Ti_{0.1}$ (30 cycles)	74.1(-)	3.2057(4)	5.2056(8)	121	25.9(1)	4.431(2)	17	0.8	0.0090
$Mg_{0.9}Ti_{0.1}$ + 5G	74(-)	3.2082(6)	5.207(1)	64	26(1)	4.437(2)	16	0.9	0.0093
$Mg_{0.9}Ti_{0.1}$ + 5G (105 cycles)	73(-)	3.2079(7)	5.209(1)	28	27(5)	4.40(1)	13	0.2	0.0096

Table 7.2: Information obtained via XRD analysis for $Mg_{0.9}Ti_{0.1}$ and $Mg_{0.9}Ti_{0.1}$ – 5 wt. % G

From the data in Table 7.2, it is first noted that the crystalline sizes in the $Mg_{0.9}Ti_{0.1}$ sample increase after absorption/desorption cycling, particularly for Mg (28 nm to 121 nm). Conversely, the Mg and TiH_2 crystalline sizes for the $Mg_{0.9}Ti_{0.1}$ – 5 wt. % G sample decrease after cycling. A similar trend is observed in terms of crystal strain, where cycling increases the strain in the TiH_2 phase in the $Mg_{0.9}Ti_{0.1}$ sample. In the $Mg_{0.9}Ti_{0.1}$ – 5 wt. % G sample, the strain decreases significantly after cycling. Mg does not exhibit strain in any of the samples analysed.

7.5 Conclusion of Study

In summary, this study provided evidence of significant morphological changes of $Mg_{0.9}Ti_{0.1}$ during cycling. TEM analysis confirmed that Mg sintering typically occurs during cycling, as previously mentioned in literature [106]. However, the addition of graphite greatly altered the morphology of the Mg-Ti nanocomposite in a beneficial way by providing further grain refinement of Mg as well as maintaining homogeneity of Mg throughout the sample. This was achieved by covering and filling the MgH_2 grains, thus preventing excessive agglomeration and sintering. In addition, the TiH_2 particles were clustered on the grain surface, thus maximising availability for hydrogen absorption and contributing towards maintaining a high hydrogen absorption capacity over 100+ cycles. The results indicate definitively that the minor addition (5 wt. %) of graphite sufficiently preserved the hydrogen absorption capacity during cycling at high temperatures, even if it clearly slowed down the hydrogenation and dehydrogenation steps.

8.0 Conclusions

The main objective of this study was to improve the hydrogen sorption performance of MgH_2, specifically to improve kinetics with the highest possible storage capacity and maintaining optimal reversible hydrogen storage capacity. In this work, the use of HRBM as a tool to effectively produce nanostructured MgH_2 composites has been validated.

The other results of this study may be summarised as follows:

8.1 Mg – FeV systems

Commercial FeV is a viable catalyst to improve hydrogen absorption/desorption in MgH_2 nanocomposites and facilitating hydrogenation during HRBM under hydrogen atmosphere. In this study, the following results were obtained specifically:

- The most pronounced improvement of dehydrogenation and re-hydrogenation kinetics was observed with Mg – 10 wt. % FeV; this sample achieved ca. 7 wt. % H storage capacity in 2 hours.
- The activation energy for dehydrogenation for the above sample was found to be reduced from 107 – 130 kJ/mol to 60 – 80 kJ/mol H_2; this translates to more than tenfold reduction of re-hydrogenation time when compared to pure Mg
- Improvements were noted to be less impactful than pure V additives, when compared to literature. This was related to the Fe substitution of V in FeV additives resulting in incomplete hydrogenation; while pure V or BCC vanadium alloys transform into FCC-VH_2 and BCT-V_2H_{1+x} upon hydrogenation, the hydrogenated Mg – FeV consisted primarily of BCC at nanocrytallite (<10 nm) sizes.
- Sintering of particles resulted in crystallite sizes growing from 20 nm to 100 nm at the upper end. However, FeV was still monocrystalline and finely distributed across the Mg/MgH_2

matrix during cycles of hydrogen absorption/desorption. This likely contributed to good cyclic stability at T = 350 °C over the first 30 cycles.

Commercially obtained FeV has a different catalytic mechanism from artificially created FeV via arc melting. The specific differences have not been studies as yet.

8.2 Mg – $FeTiO_3$ systems

It was effectively shown that $FeTiO_3$ is a viable option for catalytically enhancing MgH_2 performance at a fraction of the cost of using pure Fe, Ti or their alloys.

As demonstrated in the previous study, the Mg – $FeTiO_3$ nanocomposites had improved dehydrogenation and re-hydrogenation kinetics due to the reduction of $FeTiO_3$ during HRBM and the subsequent processes [152]. However, the nanocomposites are characterised by poor reversible hydrogen storage capacity due to impediment of unreacted Mg surfaces by MgO; it was shown in this study that the addition of carbon, particularly graphite, could form somewhat of a protective coverage over a large portion of the Mg surfaces and thus moderate this problem.

8.3 Mg – Ti systems

This study confirmed that significant morphological changes occur under cycling (at T ≥ 300 °C) which deteriorate the reversible hydrogen storage capacity of MgH_2 – TiH_2 composites without obvious effects on hydrogenation and dehydrogenation kinetics [168, 169]. These morphological changes include a shift in the distribution of TiH_2 catalyst particles on the surface of the Mg/MgH_2 matrix.

The addition of 5 wt. % graphite to the Mg – Ti nanocomposites during HRBM hydrogenation appears to slightly dampen kinetics of the initial hydrogenation as well as every subsequent hydrogen absorption/desorption step. This serves to confirm the hypothesis that carbon has no catalytic role in the hydrogenation/dehydrogenation of Mg composites but rather plays an intermediary role for H atoms [116]. TEM studies and especially elemental mapping of $Mg_{0.9}Ti_{0.1}$ and

$Mg_{0.9}Ti_{0.1}$ – 5G before and after cycling showed highly contrasting morphological features. Sintering/recrystallization of Mg was obvious for the sample without carbon, although the Mg remained uniformly distributed however with graphite, the constituent elements appeared to be even better distributed between the grains after cycling and Mg nanoparticles were further refined. The surface coverage of TiH_2 seemed to be enhanced as well. This is the defining characteristic that led to the excellent reversible hydrogen storage capacity, which deteriorated only by 2% over 105 absorption/desorption cycles at high temperature.

References

[1] E. Palermo, “Who Invented the Steam Engine?,” *Live Science*, 2014. [Online]. Available: http://www.livescience.com/44186-who-invented-the-steam-engine.html. [Accessed: 30-Aug-2016].

[2] “Svante Arrhenius (1859-1927),” *NASA Earth Observatory*. [Online]. Available: http://earthobservatory.nasa.gov/Features/Arrhenius/arrhenius.php.

[3] W. R. L. Anderegg, J. W. Prall, J. Harold, and S. H. Schneider, “Expert credibility in climate change.,” *Proc. Natl. Acad. Sci. U. S. A.*, vol. 107, no. 27, pp. 12107–9, Jul. 2010.

[4] J. Cook *et al.*, “Quantifying the consensus on anthropogenic global warming in the scientific literature,” *Environ. Res. Lett.*, vol. 8, no. 2, p. 024024, Jun. 2013.

[5] O. Milman, “Climate guru James Hansen warns of much worse than expected sea level rise | Environment | The Guardian,” *The Guardian2*, New York, 22-Mar-2016.

[6] “Nuclear Power in France,” *World Nuclear Association*, 2016. [Online]. Available: http://www.world-nuclear.org/information-library/country-profiles/countries-a-f/france.aspx. [Accessed: 17-Oct-2016].

[7] J. McCurry, “Five years on, cleanup of Fukushima’s reactors remains a distant goal,” *The Guardian*, 2016. [Online]. Available: https://www.theguardian.com/environment/2016/mar/11/fukushima-daiichi-nuclear-reactors-decommission-cleanup-japan-tsunami-meltdown. [Accessed: 17-Oct-2016].

[8] R. Poch, “Merkel says goodbye to nuclear and announces a revolution in renewables,” *La Vanguardia*, 2011. [Online]. Available: http://www.lavanguardia.com/medio-ambiente/20110531/54162870889/merkel-se-despide-de-lo-nuclear-y-anuncia-una-revolucion-en-renovables.html. [Accessed: 17-Oct-2016].

[9] A. Griffin, “Sweden breaks wind power record by half a million kWh after intense weather and storms,” *The Independent*, 2016. [Online]. Available: http://www.independent.co.uk/news/world/europe/sweden-wind-power-record-energy-storm-urd-weather-renewable-farm-a7498511.html. [Accessed: 03-Jan-2017].

[10] J. Shankleman and C. Martin, “Solar Could Beat Coal to Become the Cheapest Power on Earth,” *Bloomberg*, 2017. [Online]. Available: https://www.bloomberg.com/news/articles/2017-01-03/for-cheapest-power-on-earth-look-skyward-as-coal-falls-to-solar. [Accessed: 03-Jan-2017].

[11] Carly Cassella, “China just ran an entire region on 100% renewable energy for 7 days,” *Science Alert*, 2017. [Online]. Available: https://www.sciencealert.com/a-chinese-province-just-ran-on-100-renewable-energy-for-7-days. [Accessed: 17-Jul-2017].

[12] S. Brandon, “China just switched on the world’s largest floating solar power plant,” *World Economic Forum*, 2017. [Online]. Available: https://www.weforum.org/agenda/2017/06/china-worlds-largest-floating-solar-power/. [Accessed: 04-Sep-2017].

[13] A. Vaughan, “All Volvo cars to be electric or hybrid from 2019,” *The Guardian*, 2017. [Online]. Available: https://www.theguardian.com/business/2017/jul/05/volvo-cars-electric-hybrid-2019.

[14] D. Muoio, “Hydrogen-powered cars are better than electric cars - but there’s a catch,” *Tech Insider*, 2016. [Online]. Available: http://www.techinsider.io/why-hydrogen-powered-cars-are-better-2016-1. [Accessed: 30-Aug-2016].

[15] Y. Demirel, “Energy Storage,” 2012, pp. 305–341.

[16] S. H. Zadeh, “Hydrogen Production via Ultrasound-Aided Alkaline Water Electrolysis,” *J.*

Autom. Control Eng., vol. 2, no. 1, pp. 103–109, 2014.

[17] L. Zhou, "Progress and problems in hydrogen storage methods," *Renew. Sustain. Energy Rev.*, vol. 9, no. 4, pp. 395–408, Aug. 2005.

[18] U. DOE, "Lower and Higher Heating Values of Fuels," *Hydrogen Analysis Resource Centre*, 2015. [Online]. Available: http://hydrogen.pnl.gov/tools/lower-and-higher-heating-values-fuels. [Accessed: 23-May-2016].

[19] "Hydrogen Storage," *Energy.gov, Office of Energy Efficiency & Renewable Energy*. [Online]. Available: http://energy.gov/eere/fuelcells/hydrogen-storage. [Accessed: 30-Aug-2016].

[20] US Department of Energy, "Compare Fuel Cell Vehicles," *www.fueleconomy.gov*, 2017. [Online]. Available: http://www.fueleconomy.gov/feg/fcv_sbs.shtml. [Accessed: 04-Sep-2017].

[21] "Fuel Cell Forklift and Hydrogen Refuelling Station," *Supply Chain Today*, 2017. [Online]. Available: http://www.supplychaintoday.co.za/blog/2017/10/24/fuel-cell-forklift-hydrogen-refuelling-station/. [Accessed: 03-Sep-2018].

[22] "Hydrogen Storage Challenges," *Energy.gov, Office of Energy Efficiency & Renewable Energy*. [Online]. Available: http://energy.gov/eere/fuelcells/hydrogen-storage-challenges.

[23] US DOE, "Technical Plan — Storage." Fuel Cells Technology Office, US DOE, pp. 14–15, 2012.

[24] E. Farber, "THE DEVELOPMENT OF METAL HYDRIDE CHEMISTRY," *Chymia*, vol. 8, pp. 165–180, 1962.

[25] A. Züttel, "Hydrogen storage methods," *Naturwissenschaften*, vol. 91, no. 4, pp. 157–172, 2004.

[26] J. Sibanyoni, "Nanostructured light weight hydrogen storage materials," University of the

Western Cape, 2012.

[27] T. J. N. A. F.-O. of S. Education, “It’s Elemental - The Element Magnesium,” *Jefferson Lab*. [Online]. Available: http://education.jlab.org/itselemental/ele012.html. [Accessed: 28-Jan-2016].

[28] WebElements, “Magnesium: historical information.” [Online]. Available: http://www.webelements.com/magnesium/history.html. [Accessed: 28-Jan-2016].

[29] L. Alchin, “Magnesium Properties,” *Siteseen Ltd*. [Online]. Available: http://www.elementalmatter.info/magnesium-properties.htm. [Accessed: 28-Jan-2016].

[30] “Material Hardness Tables,” *Ted Pella, Inc.*, 1996. [Online]. Available: https://www.tedpella.com/company_html/hardness.htm. [Accessed: 19-Jan-2017].

[31] J. K. Nørskov, A. Houmøller, P. K. Johansson, and B. I. Lundqvist, “Adsorption and Dissociation of H 2 on Mg Surfaces,” *Phys. Rev. Lett.*, vol. 46, no. 4, pp. 257–260, Jan. 1981.

[32] Z. Jian, Z. Dianwu, H. Yani, P. Ping, and L. Jinshui, “Study on H2 Adsorption and Dissociation Properties on Mg(0001) Surface,” *Rare Met. Mater. Eng.*, vol. 38, no. 9, pp. 1518–1525, Sep. 2009.

[33] N. B. Arboleda, H. Kasai, K. Nobuhara, W. A. Diño, and H. Nakanishi, “Dissociation and Sticking of H_2 on Mg(0001), Ti(0001) and La(0001) Surfaces,” *J. Phys. Soc. Japan*, vol. 73, no. 3, pp. 745–748, Mar. 2004.

[34] J. Navarro-Ruiz, M. Sodupe, P. Ugliengo, A. Rimola, G. Vidali, and R. Dovesi, “Interstellar H adsorption and H_2 formation on the crystalline (010) forsterite surface: a B3LYP-D2* periodic study,” *Phys. Chem. Chem. Phys.*, vol. 16, no. 33, p. 17447, Apr. 2014.

[35] M. Durandurdu, “New high-pressure phase of MgH 2 : An ab initio constant-pressure study,” *EPL (Europhysics Lett.*, vol. 105, no. 4, p. 46001, Feb. 2014.

[36] M. Emilsson, “Hydrogen Desorption in High Pressure Phases of MgH2: a Density Functional Theory Based Study,” in *AIP Conference Proceedings*, 2006, vol. 837, pp. 168–172.

[37] D. Moser, G. Baldissin, D. J. Bull, D. J. Riley, and I. Morrison, “The pressure – temperature phase diagram of MgH 2 and isotopic substitution,” vol. 305403, 2011.

[38] S. Cui, W. Feng, H. Hu, Z. Feng, and Y. Wang, “Structural phase transitions in MgH2 under high pressure,” 2008.

[39] P. Vajeeston, P. Ravindran, A. Kjekshus, and H. Fjellvåg, “Pressure-induced structural transitions in MgH2,” *Phys. Rev. Lett.*, vol. 89, no. 17, p. 175506, 2002.

[40] P. Vajeeston *et al.*, “Structural stability and pressure-induced phase transitions in MgH 2,” *Phys. Rev. B*, vol. 73, no. 22, p. 224102, Jun. 2006.

[41] J.-P. Bastide, B. Bonnetot, J.-M. Létoffé, and P. Claudy, “Polymorphisme de l’hydrure de magnesium sous haute pression,” *Mater. Res. Bull.*, vol. 15, no. 9, pp. 1215–1224, Sep. 1980.

[42] M. Bortz, B. Bertheville, G. Bottger, K. Yvon, G. Böttger, and K. Yvon, “Structure of the high pressure phase γ-MgH 2 by neutron powder diffraction,” *J. Alloys Compd.*, vol. 287, no. 1, pp. 4–6, 1999.

[43] H. Kohlmann, Y. Zhao, M. F. Nicol, and J. McClure, “The crystal structure of α-MgD2 under high pressure by neutron powder diffraction,” *Zeitschrift für Krist.*, vol. 223, no. 10, pp. 706–710, Jan. 2008.

[44] D. Moser *et al.*, “An *in situ* neutron diffraction measurement of the pressure–temperature evolution of a MgD_2:TiD_2 mixture,” *High Press. Res.*, vol. 30, no. 4, pp. 643–652, Dec. 2010.

[45] M. Pozzo and D. Alfè, “Structural properties and enthalpy of formation of magnesium hydride from quantum Monte Carlo calculations,” *Phys. Rev. B*, vol. 77, no. 104103, pp. 1–8, 2008.

[46] C. R. Luna, C. E. Macchi, A. Juan, and A. Somoza, “Electronic and bonding properties of MgH2–Nb containing vacancies,” *Int. J. Hydrogen Energy*, vol. 35, no. 22, pp. 12421–12427, Nov. 2010.

[47] R. Varin, T. Czujko, and Z. Wronski, “Magnesium Hydride - Crystallographic Characteristics,” in *Green Energy: Basic Concepts and Fundamentals*, Xianguo Li, Ed. Springer Science & Business Media, 2011, p. 242.

[48] K. N. N. Semenenko, V. N. Verbetskij, Y. A. Kalashnikov, N. V. Timofeeva, and M. I. Ioffe, “Phase transformations of metal hydrides under conditions of superhigh pressures,” *Vestn. Mosk. Univ. Seriya 2, Khimiya*, vol. 19, no. 6, pp. 718–722, 1978.

[49] “CaF2 structure (C1) http--cst-www.” [Online]. Available: http://slideplayer.com/slide/10331621/.

[50] J. Töpler, H. Buchner, H. Säufferer, K. Knorr, and W. Prandl, “Measurements of the diffusion of hydrogen atoms in magnesium and Mg2Ni by neutron scattering,” *J. Less Common Met.*, vol. 88, no. 2, pp. 397–404, Dec. 1982.

[51] M. Stioui, A. Grayevsky, A. Moran, S. Kreitzman, N. Kaplan, and D. Shaltiel, “Proton magnetic resonance study of diffusion-related properties in magnesium-rich compounds,” *J. Less Common Met.*, vol. 104, no. 1, pp. 119–124, Dec. 1984.

[52] J. Huot, G. Liang, S. Boily, a Van Neste, R. Schulz, and A. Van Neste, “Structural study and hydrogen sorption kinetics of ball-milled magnesium hydride,” *J. Alloys Compd.*, vol. 293–295, pp. 495–500, Dec. 1999.

[53] G. Liang, J. Huot, S. Boily, A. Van Neste, and R. Schulz, “Catalytic effect of transition metals on hydrogen sorption in nanocrystalline ball milled MgH 2 –Tm (Tm5Ti, V, Mn, Fe and Ni) systems,” vol. 292, pp. 247–252, 1999.

[54] R. W. G. Wyckoff, “Scrutinyite,” in *Crystal Structures 1*, 2nd Editio., New York: Interscience Publishers, 1963, pp. 239–444.

[55] D. Chandra, J. J. Reilly, and R. Chellappa, “Metal hydrides for vehicular applications: The state of the art,” *JOM*, vol. 58, no. 2, pp. 26–32, Feb. 2006.

[56] M. H. Mintz, Z. Gavra, and Z. Hadari, “Kinetic study of the reaction between hydrogen and magnesium, catalyzed by addition of indium,” *J. Inorg. Nucl. Chem.*, vol. 40, no. 5, pp. 765–768, Jan. 1978.

[57] H. G. Schimmel, J. Huot, L. C. Chapon, F. D. Tichelaar, and F. M. Mulder, “Hydrogen cycling of niobium and vanadium catalyzed nanostructured magnesium.,” *J. Am. Chem. Soc.*, vol. 127, no. 41, pp. 14348–54, Oct. 2005.

[58] P. S. Rudman, “Hydriding and dehydriding kinetics,” *J. Less Common Met.*, vol. 89, no. 1, pp. 93–110, Jan. 1983.

[59] D. L. Douglass, “The formation and dissociation of magnesium alloy hydrides and their use for fuel storage in the hydrogen car,” *Metall. Trans. A*, vol. 6, no. 12, p. 2179, Dec. 1975.

[60] J. Bloch and M. H. Mintz, “Kinetics and mechanisms of metal hydrides formation—a review,” *J. Alloys Compd.*, vol. 253254, pp. 529–541, 1997.

[61] B. Vigeholm, K. Jensen, B. Larsen, and A. S. Pedersen, “Elements of hydride formation mechanisms in nearly spherical magnesium powder particles,” *J. Less Common Met.*, vol. 131, no. 1–2, pp. 133–141, Mar. 1987.

[62] B. Vigeholm, B. Larsen, A. S. Pedersen, and J. Kjoller, “ON THE HYDROGENATION MECHANISM IN MAGNESIUM II.,” vol. 1, pp. 1455–1463, 1984.

[63] C. M. Stander, “Kinetics of Formation of Magnesium Hydride from Magnesium and Hydrogen,” *Zeitschrift für Phys. Chemie*, vol. 104, no. 4–6, pp. 229–238, Apr. 1977.

[64] P. Spatz, H. A. Aebischer, A. Krozer, and L. Schlapbach, “The Diffusion of H in Mg and the Nucleation and Growth of MgH_2 in Thin Films*,” *Zeitschrift für Phys. Chemie*, vol. 181, no. Part_1_2, pp. 393–397, 1993.

[65] L. Mooij and B. Dam, “Nucleation and growth mechanisms of nano magnesium hydride from the hydrogen sorption kinetics,” *Phys. Chem. Chem. Phys.*, vol. 15, no. 27, p. 11501, Jul. 2013.

[66] S. Zhou *et al.*, “Effect of carbon from anthracite coal on decomposition kinetics of magnesium hydride,” *J. Alloys Compd.*, vol. 592, pp. 231–237, 2014.

[67] H. Gasan, N. Aydinbeyli, O. N. Celik, and Y. M. Yaman, “The dependence of the hydrogen desorption temperature of MgH2 on its structural and morphological characteristics,” *J. Alloys Compd.*, vol. 487, no. 1, pp. 724–729, 2009.

[68] H. Gasan, O. N. Celik, N. Aydinbeyli, and Y. M. Yaman, “Effect of V, Nb, Ti and graphite additions on the hydrogen desorption temperature of magnesium hydride,” *Int. J. Hydrogen Energy*, vol. 37, no. 2, pp. 1912–1918, Jan. 2012.

[69] R. Checchetto, N. Bazzanella, A. Miotello, and P. Mengucci, “Catalytic properties on the hydrogen desorption process of metallic additives dispersed in the MgH2 matrix,” *J. Alloys Compd.*, vol. 446–447, pp. 58–62, 2007.

[70] N. Bazzanella, R. Checchetto, and A. Miotello, “Atoms and nanoparticles of transition metals as catalysts for hydrogen desorption from magnesium hydride,” *J. Nanomater.*, vol. 2011, 2011.

[71] A. Zaluska, L. Zaluski, and J. . Ström–Olsen, “Nanocrystalline magnesium for hydrogen storage,” *J. Alloys Compd.*, vol. 288, no. 1–2, pp. 217–225, Jun. 1999.

[72] W. Cao, “Synthesis of Nanomaterials by High Energy Ball Milling,” *UnderstandingNano.com*, 2007. [Online]. Available: http://www.understandingnano.com/nanomaterial-synthesis-ball-

milling.html. [Accessed: 16-Jan-2017].

[73] P. -a. Huhn, M. Dornheim, T. Klassen, and R. Bormann, “Thermal stability of nanocrystalline magnesium for hydrogen storage,” *J. Alloys Compd.*, vol. 404–406, no. October 2004, pp. 499–502, Dec. 2005.

[74] K. J. Gross, D. Chartouni, E. Leroy, and A. Zuttel, “Mechanically milled Mg composites for hydrogen storage: the relationship between morphology and kinetics ¨,” vol. 269, pp. 259–270, 1998.

[75] N. Hanada, T. Ichikawa, and H. Fujii, “Hydrogen absorption kinetics of the catalyzed MgH2 by niobium oxide,” *J. Alloys Compd.*, vol. 446–447, no. October 2006, pp. 67–71, 2007.

[76] P. Palade *et al.*, “Hydrogen storage in Mg–Ni–Fe compounds prepared by melt spinning and ball milling,” *J. Alloys Compd.*, vol. 415, no. 1–2, pp. 170–176, May 2006.

[77] D. R. Leiva *et al.*, “Magnesium-Nickel alloy for hydrogen storage produced by melt spinning followed by cold rolling,” *Mater. Res.*, vol. 15, no. 5, pp. 813–817, Oct. 2012.

[78] J. Lu, Y. J. Choi, Z. Z. Fang, H. Y. Sohn, and E. Rönnebro, “Hydrogen Storage Properties of Nanosized MgH_2 −0.1TiH_2 Prepared by Ultrahigh-Energy−High-Pressure Milling,” *J. Am. Chem. Soc.*, vol. 131, no. 43, pp. 15843–15852, Nov. 2009.

[79] Y. J. Choi, J. Lu, H. Y. Sohn, and Z. Z. Fang, “Hydrogen storage properties of the Mg–Ti–H system prepared by high-energy–high-pressure reactive milling,” *J. Power Sources*, vol. 180, no. 1, pp. 491–497, 2008.

[80] P. Vermeulen, R. A. H. Niessen, and P. H. L. Notten, “Hydrogen storage in metastable MgyTi(1−y) thin films,” *Electrochem. commun.*, vol. 8, no. 1, pp. 27–32, Jan. 2006.

[81] H. Shao *et al.*, “Hydrogen storage and thermal conductivity properties of Mg-based materials with different structures,” *Int. J. Hydrogen Energy*, vol. 39, no. 18, pp. 9893–9898, 2014.

[82] N. Hanada, T. Ichikawa, and H. Fujii, “Catalytic Effect of Nanoparticle 3d-Transition Metals on Hydrogen Storage Properties in Magnesium Hydride MgH_2 Prepared by Mechanical Milling,” *J. Phys. Chem. B*, vol. 109, no. 15, pp. 7188–7194, Apr. 2005.

[83] V. M. Skripnyuk, E. Rabkin, L. a. Bendersky, a. Magrez, E. Carreño-Morelli, and Y. Estrin, “Hydrogen storage properties of as-synthesized and severely deformed magnesium – multiwall carbon nanotubes composite,” *Int. J. Hydrogen Energy*, vol. 35, no. 11, pp. 5471–5478, Jun. 2010.

[84] S. Bouaricha, J.-P. Dodelet, D. Guay, J. Huot, and R. Schulz, “Study of the activation process of Mg-based hydrogen storage materials modified by graphite and other carbonaceous compounds,” *J. Mater. Res.*, vol. 16, no. 10, pp. 2893–2905, Jan. 2011.

[85] J.-L. Bobet *et al.*, “Hydrogen sorption properties of graphite-modified magnesium nanocomposites prepared by ball-milling,” *J. Alloys Compd.*, vol. 366, no. 1–2, pp. 298–302, Mar. 2004.

[86] C. Lal and I. P. Jain, “Effect of ball milling on structural and hydrogen storage properties of Mg - x wt% FeTi (x=2 & 5) solid solutions,” *Int. J. Hydrogen Energy*, vol. 37, no. 4, pp. 3761–3766, Feb. 2012.

[87] R. A. Varin and T. Czujko, “Overview of processing of nanocrystalline hydrogen storage intermetallics by mechanical alloying/milling,” *Mater. Manuf. Process.*, vol. 17, no. 2, pp. 129–156, 2002.

[88] A. Zaluska, L. Zaluski, and J. O. Ström-Olsen, “Structure, catalysis and atomic reactions on the nano-scale: a systematic approach to metal hydrides for hydrogen storage,” *Appl. Phys. A Mater. Sci. Process.*, vol. 72, no. 2, pp. 157–165, 2001.

[89] B. Yang, Y. He, and Y. Zhao, “Concentration-dependent hydrogen diffusion in hydrogenation

and dehydrogenation of vanadium-coated magnesium nanoblades," *Int. J. Hydrogen Energy*, vol. 36, no. 24, pp. 15642–15651, Dec. 2011.

[90] Y. He, J. Fan, and Y. Zhao, "The role of differently distributed vanadium nanocatalyst in the hydrogen storage of magnesium nanostructures," *Int. J. Hydrogen Energy*, vol. 35, no. 9, pp. 4162–4170, May 2010.

[91] M. V Lototsky, R. V Denys, and V. A. Yartys, "Combustion-type hydrogenation of nanostructured Mg-based composites for hydrogen storage," *Int. J. Energy Res.*, no. 33, pp. 1114–1125, 2009.

[92] G. Liang, J. Huot, S. Boily, A. Van Neste, and R. Schulz, "Hydrogen storage properties of the mechanically milled MgH2–V nanocomposite," *J. Alloys Compd.*, vol. 291, no. 1, pp. 295–299, 1999.

[93] H. Shao, M. Felderhoff, and F. Schüth, "Hydrogen storage properties of nanostructured MgH2/TiH2 composite prepared by ball milling under high hydrogen pressure," *Int. J. Hydrogen Energy*, vol. 36, no. 17, pp. 10828–10833, 2011.

[94] K. Asano, H. Enoki, and E. Akiba, "Synthesis of Mg–Ti FCC hydrides from Mg–Ti BCC alloys," *J. Alloys Compd.*, vol. 478, no. 1, pp. 117–120, 2009.

[95] M. Rashad *et al.*, "Effect of graphene nanoplatelets (GNPs) addition on strength and ductility of magnesium-titanium alloys," *J. Magnes. Alloy.*, vol. 1, no. 3, pp. 242–248, Sep. 2013.

[96] C. Lu, J. Zou, X. Shi, X. Zeng, and W. Ding, "Synthesis and hydrogen storage properties of core–shell structured binary Mg@Ti and ternary Mg@Ti@Ni composites," *Int. J. Hydrogen Energy*, pp. 1–9, 2016.

[97] F. Venturi, M. Calizzi, S. Bals, T. Perkisas, and L. Pasquini, "Self-assembly of gas-phase synthesized magnesium nanoparticles on room temperature substrates," *Mater. Res. Express*,

vol. 2, no. 1, p. 015007, Dec. 2014.

[98] M. Calizzi, D. Chericoni, L. H. Jepsen, T. R. Jensen, and L. Pasquini, “Mg–Ti nanoparticles with superior kinetics for hydrogen storage,” *Int. J. Hydrogen Energy*, vol. 41, no. 32, pp. 14447–14454, 2016.

[99] H. Y. Sohn and S. Emami, “Kinetics of dehydrogenation of the Mg–Ti–H hydrogen storage system,” *Int. J. Hydrogen Energy*, vol. 36, no. 14, pp. 8344–8350, Jul. 2011.

[100] H. Jung, J. Yuh, S. Cho, and W. Lee, “Effects of Ti interlayers on microstructures and hydrogen storage capacity in Mg/Pd multilayer thin films,” *J. Alloys Compd.*, vol. 601, pp. 63–66, 2014.

[101] S. Singh, S. W. H. Eijt, M. W. Zandbergen, W. J. Legerstee, and V. L. Svetchnikov, “Nanoscale structure and the hydrogenation of Pd-capped magnesium thin films prepared by plasma sputter and pulsed laser deposition,” *J. Alloys Compd.*, vol. 441, no. 1, pp. 344–351, 2007.

[102] M. Jurczyk, M. Nowak, a. Szajek, and a. Jezierski, “Hydrogen storage by Mg-based nanocomposites,” *Int. J. Hydrogen Energy*, vol. 37, no. 4, pp. 3652–3658, 2012.

[103] T. Fujimoto, S. Ogawa, T. Kanai, N. Uchiyama, T. Yoshida, and S. Yagi, “Hydrogen storage property of materials composed of Mg nanoparticles and Ni nanoparticles fabricated by gas evaporation method,” *Int. J. Hydrogen Energy*, vol. 40, no. 35, pp. 11890–11894, 2015.

[104] A. V. Kuklin, A. a. Kuzubov, P. O. Krasnov, A. O. Lykhin, and L. V. Tikhonova, “Ni-doping effect of Mg(0001) surface to use it as a hydrogen storage material,” *J. Alloys Compd.*, vol. 609, pp. 93–99, Oct. 2014.

[105] H. Hofmann *et al.*, “Ni-doped versus undoped Mg–MgH 2 materials for high temperature heat or hydrogen storage ´,” vol. 292, pp. 57–71, 1999.

[106] G. Friedlmeier, A. Manthey, M. Wanner, M. Groll, and Y. Al, “Cyclic stability of various application-relevant metal hydrides,” *J. Alloys Compd.*, vol. 231, no. 1–2, pp. 880–887, Dec.

1995.

[107] A. Reiser, B. Bogdanović, and K. Schlichte, “The application of Mg-based metal-hydrides as heat energy storage systems,” *Int. J. Hydrogen Energy*, vol. 25, no. 5, pp. 425–430, 2000.

[108] H. Shao *et al.*, “Phase and morphology evolution study of ball milled Mg–Co hydrogen storage alloys,” *Int. J. Hydrogen Energy*, vol. 38, no. 17, pp. 7070–7076, 2013.

[109] P. Zolliker, K. Yvon, P. Fischer, and J. Schefer, “Dimagnesium cobalt(I) pentahydride, Mg2CoH5, containing square-pyramidal pentahydrocobaltate(4-) (CoH54-) anions,” *Inorg. Chem.*, vol. 24, no. 24, pp. 4177–4180, Nov. 1985.

[110] E. Y. Ivanov, I. G. Konstanchuk, A. A. Stepanov, Y. Jie, M. Pezat, and B. Darriet, “The ternary system magnesium-cobalt-hydrogen,” *Inorg. Chem.*, vol. 28, no. 3, pp. 613–615, Feb. 1989.

[111] F. C. Gennari and F. J. Castro, “Formation, composition and stability of Mg–Co compounds,” *J. Alloys Compd.*, vol. 396, no. 1, pp. 182–192, 2005.

[112] W. Oelerich, T. Klassen, and R. Bormann, “Metal oxides as catalysts for improved hydrogen sorption in nanocrystalline Mg-based materials,” *J. Alloys Compd.*, vol. 315, no. 1, pp. 237–242, 2001.

[113] C. J. Webb, “A review of catalyst-enhanced magnesium hydride as a hydrogen storage material,” *J. Phys. Chem. Solids*, pp. 1–11, Jun. 2014.

[114] G. Barkhordarian, T. Klassen, and R. Bormann, “Fast hydrogen sorption kinetics of nanocrystalline Mg using Nb2O5 as catalyst,” *Scr. Mater.*, vol. 49, no. 3, pp. 213–217, Aug. 2003.

[115] M. Polanski, J. Bystrzycki, R. a. Varin, T. Plocinski, and M. Pisarek, “The effect of chromium (III) oxide (Cr2O3) nanopowder on the microstructure and cyclic hydrogen storage behavior of magnesium hydride (MgH2),” *J. Alloys Compd.*, vol. 509, no. 5, pp. 2386–2391, Feb. 2011.

[116] M. Lototskyy, J. M. Sibanyoni, R. V. Denys, M. Williams, B. G. Pollet, and V. a. Yartys, "Magnesium–carbon hydrogen storage hybrid materials produced by reactive ball milling in hydrogen," *Carbon N. Y.*, vol. 57, pp. 146–160, Jun. 2013.

[117] A. S. Awad *et al.*, "Effect of carbons (G and CFs), TM (Ni, Fe and Al) and oxides (Nb 2 O 5 and V 2 O 5) on hydrogen generation from ball milled Mg-based hydrolysis reaction for fuel cell," *Energy*, vol. 95, pp. 175–186, Jan. 2016.

[118] M. G. Verón, H. Troiani, and F. C. Gennari, "Synergetic effect of Co and carbon nanotubes on MgH2 sorption properties," *Carbon N. Y.*, vol. 49, no. 7, pp. 2413–2423, Jun. 2011.

[119] H. Imamura *et al.*, "Carbon nanocomposites synthesized by high-energy mechanical milling of graphite and magnesium for hydrogen storage," *Acta Mater.*, vol. 51, no. 20, pp. 6407–6414, Dec. 2003.

[120] A. D. D. Rud and A. M. M. Lakhnik, "Effect of carbon allotropes on the structure and hydrogen sorption during reactive ball-milling of Mg e C powder mixtures," *Int. J. Hydrogen Energy*, vol. 37, no. 5, pp. 4179–4187, Mar. 2011.

[121] S. Zhou *et al.*, "Effectiveness of crystallitic carbon from coal as milling aid and for hydrogen storage during milling with magnesium," *Fuel*, vol. 109, pp. 68–75, Jul. 2013.

[122] M. a. Lillo-Ródenas, Z. X. Guo, K. F. Aguey-Zinsou, D. Cazorla-Amorós, and a. Linares-Solano, "Effects of different carbon materials on MgH2 decomposition," *Carbon N. Y.*, vol. 46, pp. 126–137, 2008.

[123] D. Cao and W. Wang, "Storage of hydrogen in single-walled carbon nanotube bundles with optimized parameters: Effect of external surfaces," *Int. J. Hydrogen Energy*, vol. 32, no. 12, pp. 1939–1942, 2007.

[124] A. C. Dillon, K. M. Jones, T. A. Bekkedahl, C. H. Kiang, D. S. Bethune, and M. J. Heben, "Storage

of hydrogen in single-walled carbon nanotubes," *Nature*, vol. 386, no. 6623, pp. 377–379, Mar. 1997.

[125] M. Y. Song, M. Pezat, B. Darriet, and P. Hagenmuller, "Hydriding mechanism of Mg2Ni in the presence of oxygen impurity in hydrogen," *J. Mater. Sci.*, vol. 20, no. 8, pp. 2958–2964, Aug. 1985.

[126] R. B. Schwarz, "Hydrogen Storage in Alloys," *MRS Bull.*, vol. 24, pp. 40–44, 1999.

[127] S. Kwon, S. Baek, D. R. Mumm, S.-H. Hong, and M. Song, "Enhancement of the hydrogen storage characteristics of Mg by reactive mechanical grinding with Ni, Fe and Ti," *Int. J. Hydrogen Energy*, vol. 33, no. 17, pp. 4586–4592, Sep. 2008.

[128] Y. Yan, Y. Chen, H. Liang, C. Wu, and M. Tao, "Hydrogen storage properties of V30–Ti–Cr–Fe alloys," *J. Alloys Compd.*, vol. 427, no. 1–2, pp. 110–114, Jan. 2007.

[129] J. Yoo, G. Shim, S. Cho, and C. Park, "Effects of desorption temperature and substitution of Fe for Cr on the hydrogen storage properties of Ti0.32Cr0.43V0.25Ti0.32Cr0.43V0.25 alloy," *Int. J. Hydrogen Energy*, vol. 32, no. 14, pp. 2977–2981, Sep. 2007.

[130] T. Dou, Z. Wu, J. Mao, and N. Xu, "Application of commercial ferrovanadium to reduce cost of Ti–V-based BCC phase hydrogen storage alloys," *Mater. Sci. Eng. A*, vol. 476, no. 1–2, pp. 34–38, Mar. 2008.

[131] S. F. Santos and J. Huot, "Hydrogen storage in Ti–Mn–(FeV) BCC alloys," *J. Alloys Compd.*, vol. 480, no. 1, pp. 5–8, Jul. 2009.

[132] J. Huot, D. B. Ravnsbæk, J. Zhang, F. Cuevas, M. Latroche, and T. R. Jensen, "Mechanochemical synthesis of hydrogen storage materials," *Prog. Mater. Sci.*, vol. 58, no. 1, pp. 30–75, Jan. 2013.

[133] J. S. Benjamin and T. E. Volin, "The mechanism of mechanical alloying," *Metall. Trans.*, vol. 5,

no. 8, pp. 1929–1934, 1974.

[134] C. Suryanarayana, “Mechanical alloying and milling,” *Prog. Mater. Sci.*, vol. 46, no. 1–2, pp. 1–184, Jan. 2001.

[135] T. Prasad Yadav, R. Manohar Yadav, and D. Pratap Singh, “Mechanical Milling: a Top Down Approach for the Synthesis of Nanomaterials and Nanocomposites,” *Nanosci. Nanotechnol.*, vol. 2, no. 3, pp. 22–48, 2012.

[136] T. Spassov, P. Delchev, P. Madjarov, M. Spassova, and T. Himitliiska, “Hydrogen storage in Mg–10at.% LaNi5 nanocomposites, synthesized by ball milling at different conditions,” *J. Alloys Compd.*, vol. 495, no. 1, pp. 149–153, Apr. 2010.

[137] S. Zhou *et al.*, “Nano-confined magnesium for hydrogen storage from reactive milling with anthracite carbon as milling aid,” *Int. J. Hydrogen Energy*, vol. 39, no. 25, pp. 2–7, Mar. 2014.

[138] “8000M Mixer/Mill® | SPEX SamplePrep,” *Spex Sample Prep*, 2014. [Online]. Available: http://www.spexsampleprep.com/8000M-mixermill. [Accessed: 16-Jan-2017].

[139] J.-L. Bobet, B. Chevalier, M. Y. Song, and B. Darriet, “Improvements of hydrogen storage properties of Mg-based mixtures elaborated by reactive mechanical milling,” *J. Alloys Compd.*, vol. 356, pp. 570–574, 2003.

[140] Y. S. Chuang and S. J. Hwang, “Synthesis and hydrogen absorption/desorption properties of Mg-Nb2O5-SWCNT/MWCNT nanocomposite prepared by reactive milling,” *J. Alloys Compd.*, vol. 656, pp. 835–842, 2015.

[141] A. K. Nath, C. Jiten, and K. C. Singh, “Influence of ball milling parameters on the particle size of barium titanate nanocrystalline powders,” *Phys. B Condens. Matter*, vol. 405, no. 1, pp. 430–434, 2010.

[142] H. Yuan, Y. An, G. Xu, and C. Chen, “Hydriding behavior of magnesium-based hydrogen

storage alloy modified by mechanical ball-milling," *Mater. Chem. Phys.*, vol. 83, no. 2–3, pp. 340–344, Feb. 2004.

[143] F. L. Zhang, M. Zhu, and C. Y. Wang, "Parameters optimization in the planetary ball milling of nanostructured tungsten carbide/cobalt powder," *Int. J. Refract. Met. Hard Mater.*, vol. 26, no. 4, pp. 329–333, 2008.

[144] F. J. Gotor, M. Achimovicova, C. Real, and P. Balaz, "Influence of the milling parameters on the mechanical work intensity in planetary mills," *Powder Technol.*, no. 233, pp. 1–7, 2013.

[145] G. B. Schaffer and P. G. McCormick, "On the kinetics of mechanical alloying," *Metall. Trans. A*, vol. 23, no. 4, pp. 1285–1290, Apr. 1992.

[146] J.-L. Bobet, E. Akiba, Y. Nakamura, and B. Darriet, "Study of Mg-M (M=Co, Ni and Fe) mixture elaborated by reactive mechanical alloying — hydrogen sorption properties," *Int. J. Hydrogen Energy*, vol. 25, no. 10, pp. 987–996, 2000.

[147] US DOE, "Hydrogen Storage | Department of Energy," 2017. [Online]. Available: https://energy.gov/eere/fuelcells/hydrogen-storage. [Accessed: 22-May-2017].

[148] H. Imamura, K. Masanari, M. Kusuhara, H. Katsumoto, T. Sumi, and Y. Sakata, "High hydrogen storage capacity of nanosized magnesium synthesized by high energy ball-milling," *J. Alloys Compd.*, vol. 386, no. 1–2, pp. 211–216, Jan. 2005.

[149] M. Song, J. Bobet, and B. Darriet, "Improvement in hydrogen sorption properties of Mg by reactive mechanical grinding with Cr2O3, Al2O3 and CeO2," *J. Alloys Compd.*, vol. 340, pp. 256–262, 2002.

[150] C. Z. Wu *et al.*, "Hydrogen storage properties of MgH2/SWNT composite prepared by ball milling," *J. Alloys Compd.*, vol. 420, no. 1–2, pp. 278–282, Aug. 2006.

[151] K. S. Munir, P. Kingshott, and C. Wen, "Carbon Nanotube Reinforced Titanium Metal Matrix

Composites Prepared by Powder Metallurgy—A Review," *Crit. Rev. Solid State Mater. Sci.*, vol. 40, no. 1, pp. 38–55, Jan. 2015.

[152] M. Lototskyy, M. W. Davids, J. M. Sibanyoni, J. Goh, and B. G. Pollet, "Magnesium-based hydrogen storage nanomaterials prepared by high energy reactive ball milling in hydrogen at the presence of mixed titanium-iron oxide," *J. Alloys Compd.*, vol. 645, no. S1, pp. S454–S459, 2015.

[153] H. E. Kissinger, "Reaction Kinetics in Differential Thermal Analysis," *Anal. Chem.*, vol. 29, no. 11, pp. 1702–1706, Nov. 1957.

[154] H. zur Loye, "X-Ray Diffraction - How it works, what it can and what it cannot tell us," 2001.

[155] P. Scherrer, "Bestimmung der Größe und der inneren Struktur von Kolloidteilchen mittels Röntgenstrahlen," *Nachrichten von der Gesellschaft der Wissenschaften zu Göttingen, Math. Klasse*, vol. 26, pp. 98–100, 1918.

[156] T. Ungar, "Warren-Averback Applications," in *Industrial applications of X-ray diffraction*, F. H. Chung and D. K. (Deane K. Smith, Eds. New York: Marcel Dekker, 2000, p. 847.

[157] P. Mengucci, G. Barucca, G. Majni, N. Bazzanella, R. Checchetto, and A. Miotello, "Structure modification of Mg-Nb films under hydrogen sorption cycles," *J. Alloys Compd.*, vol. 509, no. SUPPL. 2, pp. S572–S575, 2011.

[158] C. Suryanarayana and M. G. Norton, *X-Ray diffraction : A practical approach*. Springer Science & Business Media, 2013.

[159] P. D. Goodell, G. D. Sandrock, and E. L. Huston, "Kinetic and dynamic aspects of rechargeable metal hydrides," *Journal of the less-common metals*, vol. 73, no. 1. pp. 135–142, 01-Sep-1980.

[160] M. V. Lototsky, "Sieverts-type setup for measurements of hydrogen sorption properties of

materials." Cape Town, 2006.

[161] R. Schulz *et al.*, "Recent developments in the applications of nanocrystalline materials to hydrogen technologies," *Mater. Sci. Eng. A*, vol. 267, no. 2, pp. 240–245, Jul. 1999.

[162] Westbrook Resources Ltd., "Westbrook Metal Powders." Sheffield.

[163] T. Liu, C. Chen, C. Qin, and X. Li, "Improved hydrogen storage properties of Mg-based nanocomposite by addition of LaNi5 nanoparticles," *Int. J. Hydrogen Energy*, vol. 39, no. 32, pp. 18273–18279, 2014.

[164] R. V. Denys, a. B. Riabov, J. P. Maehlen, M. V. Lototsky, J. K. Solberg, and V. a. Yartys, "In situ synchrotron X-ray diffraction studies of hydrogen desorption and absorption properties of Mg and Mg–Mm–Ni after reactive ball milling in hydrogen," *Acta Mater.*, vol. 57, no. 13, pp. 3989–4000, Aug. 2009.

[165] P. S. White, J. R. Rodgers, and Y. Le Page, "Crystmet: A database of the structures and powder patterns of metals and intermetallics," *Acta Crystallogr. Sect. B Struct. Sci.*, vol. 58, no. 3 PART 1, pp. 343–348, 2002.

[166] K. Asano, S. Hayashi, and Y. Nakamura, "Formation of hydride phase and diffusion of hydrogen in the V–H system varied by substitutional Fe," *Int. J. Hydrogen Energy*, vol. 41, no. 15, pp. 6369–6375, Apr. 2016.

[167] J.-C. Crivello *et al.*, "Review of magnesium hydride-based materials: development and optimisation," *Appl. Phys. A*, vol. 122, no. 2, p. 97, Feb. 2016.

[168] F. G. Eisenberg, D. A. Zagnoli, and J. J. Sheridan, "The effect of surface nickel on the hydriding-dehydriding kinetics of MgH2," *J. Less Common Met.*, vol. 74, no. 2, pp. 323–331, Oct. 1980.

[169] Z. Dehouche, J. Goyette, T. K. Bose, and R. Schulz, "Moisture effect on hydrogen storage properties of nanostructured MgH2–V–Ti composite," *Int. J. Hydrogen Energy*, vol. 28, no. 9,

pp. 983–988, Sep. 2003.

[170] J. W. Cahn, “Transformation kinetics during continuous cooling,” *Acta Metall.*, vol. 4, no. 6, pp. 572–575, Nov. 1956.

[171] T. FORDE, J. MAEHLEN, V. YARTYS, M. LOTOTSKY, and H. UCHIDA, “Influence of intrinsic hydrogenation/dehydrogenation kinetics on the dynamic behaviour of metal hydrides: A semi-empirical model and its verification,” *Int. J. Hydrogen Energy*, vol. 32, no. 8, pp. 1041–1049, Jun. 2007.

[172] C. Zhou *et al.*, “Stability of Catalyzed Magnesium Hydride Nanocrystalline During Hydrogen Cycling. Part II: Microstructure Evolution,” *J. Phys. Chem. C*, vol. 119, no. 39, pp. 22272–22280, Oct. 2015.

[173] C. Zhou, Z. Z. Fang, and R. C. Bowman, “Stability of Catalyzed Magnesium Hydride Nanocrystalline During Hydrogen Cycling. Part I: Kinetic Analysis,” *J. Phys. Chem. C*, vol. 119, no. 39, pp. 22261–22271, Oct. 2015.

Appendix 1 – US DOE Targets for Hydrogen Storage Performance

Source: Fuel Cells Technology Office, Office of Energy Efficiency & Renewable Energy, US DOE

(URL: https://www.energy.gov/eere/fuelcells/doe-technical-targets-onboard-hydrogen-storage-light-duty-vehicles)

Table 3.3.3 Technical System Targets: Onboard Hydrogen Storage for Light-Duty Fuel Cell Vehicles [a,i]

Storage Parameter	Units	2020	Ultimate
System Gravimetric Capacity Usable, specific-energy from H_2 (net useful energy/max system mass) [b]	kWh/kg (kg H_2/kg system)	1.8 (0.055)	2.5 (0.075)
System Volumetric Capacity Usable energy density from H_2 (net useful energy/max system volume) [b]	kWh/L (kg H_2/L system)	1.3 (0.040)	2.3 (0.070)
Storage System Cost	$/kWh net	10	8
	($/kg H_2 stored)	333	266
• Fuel cost [c]	$/gge at pump	2-4	2-4
Durability/Operability			
• Operating ambient temperature [d]	°C	-40/60 (sun)	-40/60 (sun)
• Min/max delivery temperature	°C	-40/85	-40/85
• Operational cycle life (1/4 tank to full)	Cycles	1500	1500
• Min delivery pressure from storage system	bar (abs)	5	3
• Max delivery pressure from storage system	bar (abs)	12	12
• Onboard Efficiency [e]	%	90	90
• "Well" to Powerplant Efficiency [e]	%	60	60
Charging / Discharging Rates			
• System fill time (5 kg)	min	3.3	2.5
	(kg H_2/min)	(1.5)	(2.0)
• Minimum full flow rate	(g/s)/kW	0.02	0.02
• Start time to full flow (20 °C)	s	5	5
• Start time to full flow (-20 °C)	s	15	15
• Transient response at operating temperature 10%-90% and 90%-0%	s	0.75	0.75
Fuel Quality (H_2 from storage) [f]	% H_2	SAE J2719 and ISO/PDTS 14687-2 (99.97% dry basis)	
Environmental Health & Safety			
• Permeation & leakage [g]	-	Meets or exceeds applicable standards, for example SAE J2579	
• Toxicity	-		
• Safety	-		
• Loss of usable H_2 [h]	(g/h)/kg H_2 stored	0.05	0.05

[a] Targets are based on the lower heating value of hydrogen, 33.3 kWh/kg H_2. Targets are for a complete system, including tank, material, valves, regulators, piping, mounting brackets, insulation, added cooling capacity, and all other balance-of-plant components. All capacities are defined as usable capacities that could be delivered to the fuel cell power plant. All targets must be met at the end of service life (approximately 1500 cycles or 5000 operation hours, equivalent of 150,000 miles).

[b] Capacities are defined as the usable quantity of hydrogen deliverable to the powerplant divided by the total mass/volume of the complete storage system, including all stored hydrogen, media, reactants (e.g., water for hydrolysis-based systems), and system components. Tank designs that are conformable and have the ability to be

efficiently package onboard vehicles may be beneficial even if they do not meet the full volumetric capacity targets. Capacities must be met at end of service life.

c Hydrogen threshold cost is independent of pathway and is defined as the untaxed cost of hydrogen produced, delivered and dispensed to the vehicle.[http://hydrogen.energy.gov/pdfs/11007_h2_threshold_costs.pdf]For material-based storage technologies, the impact of the technology on the hydrogen threshold cost, e.g., off-board cooling, off-board regeneration of chemical hydrogen storage materials, etc., must be taken into account.

d Stated ambient temperature plus full solar load (i.e., full exposure to direct sunlight). No allowable performance degradation from –20 °C to 40 °C. Allowable degradation outside these limits is to be determined.

e Onboard efficiency is the energy efficiency for delivering hydrogen from the storage system to the fuel cell powerplant, i.e., accounting for any energy required for operating pumps, blowers, compressors, heating, etc. required for hydrogen release. Well-to-powerplant efficiency includes onboard efficiency plus off-board efficiency, i.e., accounting for the energy efficiency of hydrogen production, delivery, liquefaction, compression, dispensing, regeneration of chemical hydrogen storage materials, etc. as appropriate. H2A and HDSAM analyses should be used for projecting off-board efficiencies.

f Hydrogen storage systems must be able to deliver hydrogen meeting acceptable hydrogen quality standards for fuel cell vehicles (see SAE J2719 and ISO/PDTS 14687-2). Note that some storage technologies may produce contaminants for which effects are unknown and not addressed by the published standards; these will be addressed by system engineering design on a case-by-case basis as more information becomes available.

g Total hydrogen lost into the environment as H_2; relates to hydrogen accumulation in enclosed spaces. Storage system must comply with applicable standards for vehicular tanks including but not limited to SAE J2579 and the United Nations Global Technical Regulation. This includes any coating or enclosure that incorporates the envelope of the storage system.

h Total hydrogen lost from the storage system, including leaked or vented hydrogen; relates to loss of range.

i Details in this table are being revised to match changes in the high level cost target.

Appendix 2 – Schematic of Sieverts' apparatus

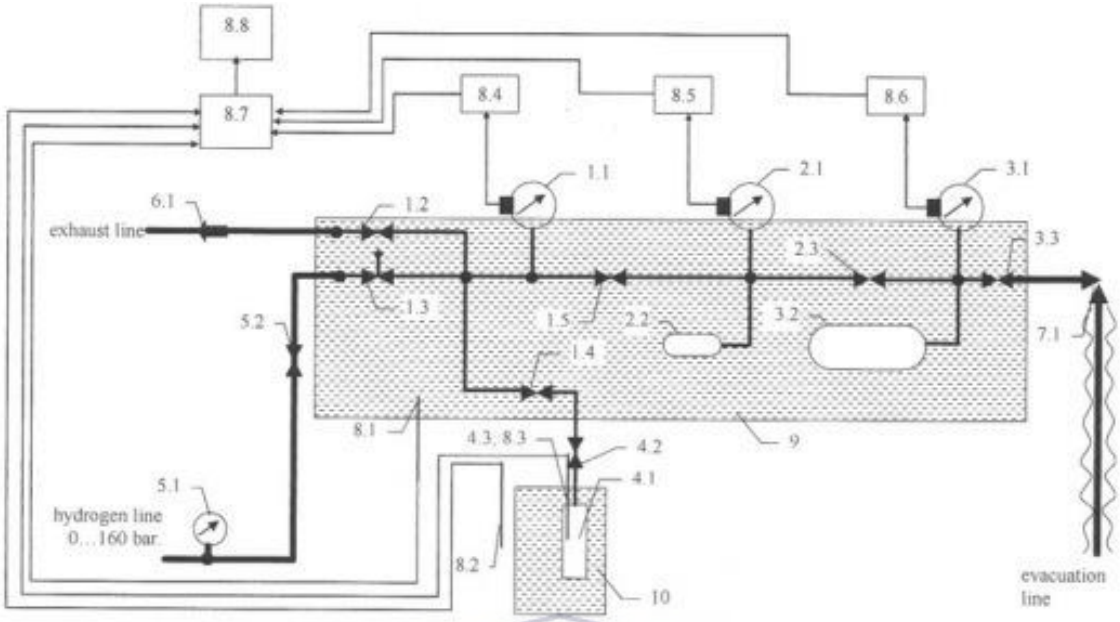

Figure 2. Gas / Measurements scheme of the Setup:

1. High-pressure collector:
   - 1.1. Pressure sensor 160 bar FS
   - 1.2. Exhaust valve
   - 1.3. H_2 input valve
   - 1.4. Reactor valve
   - 1.5. Medium-pressure connection valve
2. Medium-pressure collector:
   - 2.1. Pressure sensor 16 bar FS
   - 2.2. Buffer cylinder 75 cm^3
   - 2.3. Low-pressure connection valve
3. Low-pressure collector:
   - 3.1. Pressure sensor 2.5 bar FS
   - 3.2. Buffer cylinder 500 cm^3
   - 3.3. Evacuation valve
4. Reactor assembly
   - 4.1. Reactor body
   - 4.2. Gas connection line with locking valve
   - 4.3. Thermocouple
5. H_2 supply line:
   - 5.1. Manometer 160 bar FS
   - 5.2. H_2 supply valve
6. Exhaust line:
   - 6.1. Check valve
7. Evacuation line
   - 7.1. Vacuum valve
8. Data acquisition system
   - 8.1. Thermistor measuring bath temperature
   - 8.2. Thermistor measuring room temperature
   - 8.3. Thermocouple measuring sample temperature
   - 8.4. 160 bar pressure indicator / transmitter
   - 8.5. 16 bar pressure indicator / transmitter
   - 8.6. 2.5 bar pressure indicator / transmitter
   - 8.7. 34970A data acquisition / switch unit
   - 8.8. PC
9. Bath
10. Thermostat / furnace

Appendix 3 – Kissinger plots for select Mg – FeV and Mg –FeV –C samples

(Line labels correspond to peak numbers)

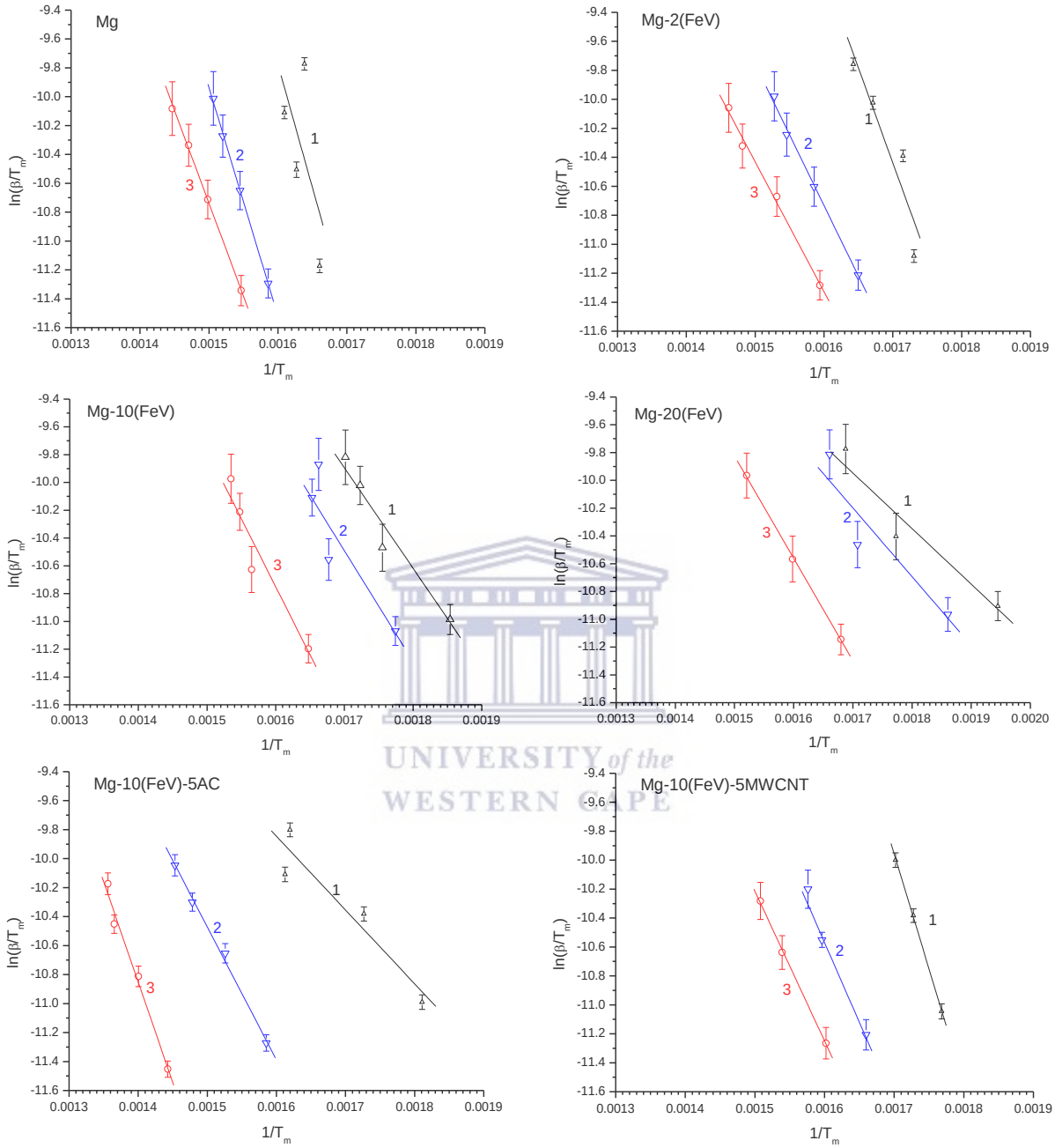

Appendix 4 – XRD Reference data

Source: CRYSMET database, v6.0, © TOth Information Systems, Inc.

α-MgH_2 - *P*4_2/*mnm* (#136); *a* = 4.4853 Å, *c* = 2.9993 Å; structure type TiO_2, ID: 506716
γ-MgH_2- *Pbcn* (#60); *a* = 4.4860 Å, *b* = 5.4024 Å, *c* = 4.8985 Å; structure type α-PbO_2, ID: 506717
Mg - *P*6_3/*mmc* (#194); *a*=3.2125 Å, *c*= 5.2132 Å, ID: 455030
BCT-H, sample Mg-68V -*I*4_1/*amd* (#141, origin choice 2); *a* = 6.035 Å, *c* = 6.872 Å; V_2H, ID: 122647
BCT-H, samples Mg-x(FeV)(-5C) - *I*4/*mmm* (#139); *a*=2.96 Å, *c*=3.378 Å; $(V_{0.9}Fe_{0.1})_2H$
FCC-H, sample Mg-68V - *Fm*-3*m* (#225); *a* = 4.268 Å; structure type CaF_2; VH_2, ID: 21150
FCC-H, samples Mg-x(FeV)(-5C) - *Fm*-3*m* (#225); *a* = 3.961 Å; structure type NaCl; $(V_{0.9}Fe_{0.1})H$
BCC, BCC-H - *Im*-3*m* (#229); *a*= 2.892 Å; $V_{0.8}Fe_{0.2}$, ID: 26787